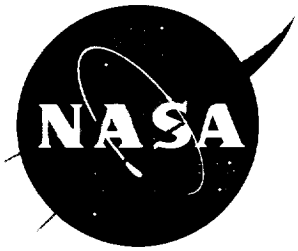

NASA Technical Paper 3704

Design of Launch Vehicle Flight Control Augmentors and Resulting Flight Stability and Control (Center Director's Discretionary Fund Project 93–05, Part III)

C. Barret, Ph.D.
Marshall Space Flight Center • MSFC, Alabama

National Aeronautics and Space Administration
Marshall Space Flight Center • MSFC, Alabama 35812

August 1997

ACKNOWLEDGMENTS

The author wishes to acknowledge the wind tunnel test team at MSFC for their efforts, and the MSFC Center Director's Discretionary Fund program for the research funding.

TABLE OF CONTENTS

LIST OF FIGURES

LIST OF TABLES

NOMENCLATURE

α	=	Angle-of-attack (deg)
AT	=	Aerodynamic torque (ft-lb)
β	=	Angle-of-sideslip (deg)
C_ℓ	=	Coefficient of rolling moment
C_m	=	Coefficient of pitching moment
C_n	=	Coefficient of yawing moment
C_{m_α}	=	$\frac{\partial C_m}{\partial \alpha}$ = Gradient of coefficient of pitching moment (per deg)
$\left(C_{m_q} + C_{m_{\dot{\alpha}}}\right)$	=	Pitch damping derivatives
C_A	=	Coefficient of axial force
C_N	=	Coefficient of normal force
C_Y	=	Coefficient of side force
C_{N_α}	=	$\frac{\partial C_N}{\partial \alpha}$ = Gradient of coefficient of normal force (per deg)
$C_{N_{\alpha_F}}$	=	$\frac{\partial C_{N_F}}{\partial \alpha}$ = Flight control augmentor gradient of coefficient of normal force (per deg)
C_{N_C}	=	Canard normal force coefficient
CR	=	Control ratio (nondimensional)
CT	=	Control torque (ft-lb)
d	=	Reference length, which for a launch vehicle is the diameter of the major portion of the fuselage and is called a caliber (ft)
δ_C	=	Deflection angle of the all-movable canard in degrees
δ_E	=	Engine gimbal deflection angle (deg)
δ_F	=	Deflection angle of the all-movable flight control augmentor (deg)
E	=	Number of engines
I_y	=	Moment of inertia about y-axis (slugs-ft^2)
μ	=	Launch vehicle mass
Λ	=	Angle of planform sweep
ℓ_{cp}	=	Moment arm from center-of-gravity to center-of-pressure (ft)
ℓ_C	=	Moment arm from LV cg to *ac* of canard

ℓ_E	=	Moment arm from cg to engine gimbal plane (ft)
ℓ_F	=	Moment arm from center-of-gravity to aerodynamic center of flight control augmentor (ft)
N	=	Normal force (lb)
N_C	=	Normal force provided by canard (lb)
N_F	=	Normal force provided by flight control augmentors (lb)
Q	=	Dynamic pressure (lb/ft^2)
S	=	Reference area, which for a launch vehicle is the cross sectional area of the major length of fuselage (ft^2)
S_C	=	Planform area of one canard in a horizontal position
S_F	=	Planform area of one flight control augmentor (ft^2)
t	=	Time to half or double amplitude of oscillation (sec)
T	=	Thrust per engine (lb)
u	=	Forward flight velocity (ft/sec)
X_{cg}	=	Distance from Moment Reference Point to center of gravity (ft)
X_{cp}	=	Distance from Moment Reference Point to center of pressure (ft)

TECHNICAL PAPER

DESIGN OF LAUNCH VEHICLE FLIGHT CONTROL AUGMENTORS AND RESULTING FLIGHT STABILITY AND CONTROL (Center Director's Discretionary Fund Project 93–05, Part III)

I. INTRODUCTION

The Space Shuttle was only the first step in achieving routine access to space. Recently, a whole spectrum of new launch vehicles (LV's) for space transportation have been studied at the NASA Marshall Space Flight Center (MSFC). In all future LV designs, decreasing the structural weight will always be of great concern. This is tantamount to increased payload capability, which in turn means reduced cost-per-pound to orbit. One very significant increase in payload capability has been defined in an LV family studied. It has been shown that a sizable weight savings can be realized by a rearrangement of the internal propellant tanks. Studies have been conducted both at MSFC and at Lockheed-Martin, maker of the Space Shuttle external tank (ET), which show that a very substantial weight can be saved by inverting the relative positions of the liquid hydrogen (LH_2) and the liquid oxygen (LOX) propellant tanks.

As the vehicle sits on the launch pad in the conventional configuration, the heavier LOX tank is located on top of the lighter LH_2 tank. This requires a heavy structural member between the two tanks to prevent the lighter LH_2 tank from being crushed. This configuration also requires large, long, heavy, and even drag-producing LOX feed lines running the length of the vehicle on the exterior fuselage. If the relative position of the propellant tanks is inverted, both the heavy structural separation member and the long LOX feed lines could be deleted. This configuration would also reduce the fueling time. While the structures community was elated with this finding, the LOX tank aft configuration gave the vehicle an aft center-of-gravity (cg) location which surfaced controllability concerns. In the conventional configuration, the LV is controlled in the ascent trajectory by the gimbaling of its rocket engines. However, the resulting aft cg configured LV would not be adequately controllable with engine gimbaling alone. It is known that the controllability of an aft cg LV is decreased. Today, more aft cg LV's are appearing due to larger numbers of aft engines and added strap-on boosters. Therefore, in the new spectrum of LV's being considered, when the available control authority has been determined to be inadequate or marginal, some means of flight control augmentation is required.

In this research effort, the author has proposed that the designed all-movable, blunt-trailing-edge flight control augmentors (FCA's), possibly incorporating smart materials for small tab actuation to aid actuation of the FCA's and advanced composites for reduced thermal protection requirements, provide the required flight control augmentation for the aft cg-configured LV, especially when needed most in the ascent trajectory, during maximum dynamic pressure. Reference 1 shows that while stationary aerodynamic surfaces have been used in the past in the Saturn series of LV's, and while there have been some small movable tip controls on some earlier LV's, all movable FCA's have not been used on a large Saturn-class

LV to augment engine gimbaling to the author's knowledge. The designed FCA's can also be used in the marginal control configuration to enhance controllability, as load alleviators, to reduce engine gimbaling requirements, to provide engine actuator failure protection, and to enhance crew safety and vehicle reliability by providing more control in engine-out events.

The added control capability through the use of the FCA's allows greater tolerance of wind magnitudes and a minimization of bending moments on the vehicle both during liftoff and ascent. Conventionally, the LV aerodynamic loads during ascent are alleviated by turning the vehicle into the wind, thereby reducing the flight angle-of-attack (α) and/or angle-of-sideslip (β). Thus, load relief is accomplished at the expense of trajectory deviation. Load relief control is most necessary when the LV experiences maximum dynamic pressure and the aerodynamic loads are greatest. The time during the maximum dynamic pressure portion of the trajectory happens to be when the FCA's would provide the most significant assistance. For prelaunch, the unfueled vehicle on the pad must withstand peak winds of 75 knots, and fueled at liftoff peak winds of 50 knots. The environmental disturbances are multiplied by 1.5 to account for Von Karmán vortex shedding effects.

Wind profiles show greatest steady wind speeds occur between 20,000 and 60,000 feet with a gust overshoot of up to 50 percent. The more the engines are required to gimbal, the more engineering design and cost is involved to have the propellant ducts move with the gimbal action while maintaining a full flow of fuel. The extension, compression, and torsion of the propellant ducts become limiting factors of engine gimbaling. Thus, the designed FCA's of this research provide not only the required control augmentation, but a plethora of additional significant benefits.

Figure 1 shows the scope of this comprehensive research project. Previous publications (1–8) have presented: the developmental stages of the program, the comprehensive reviews of our national heritage of LV's that have used aerodynamic surfaces and current use of these by other nations, a state-of-the-art assessment of smart materials and advanced composites directly applicable to the innovative design of the FCA's, and facets of design and flight stability.

This publication concatenates and expounds on the details of the designed FCA's, the static stability and dynamic stability wind tunnel test programs, the static stability and control analyses, the dynamic stability characteristics of the experimental LV with the designed FCA's, and the elastic vehicle analysis.

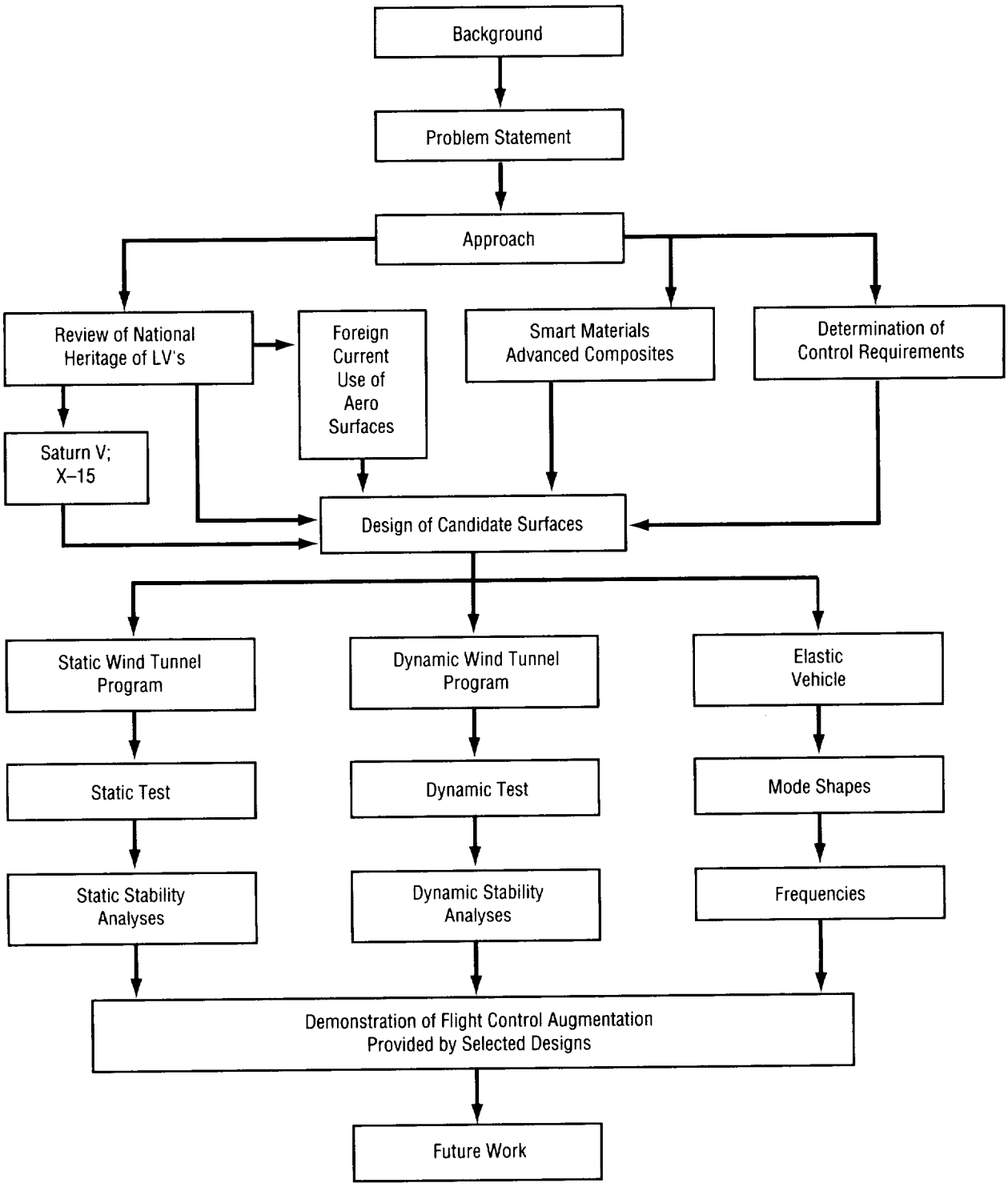

FIGURE 1. Flow chart of conducted research.

II. CONTROL REQUIREMENTS

For this research effort, an experimental LV has been selected which is an expendable vehicle very similar to the Saturn V in many respects and 74 percent of its length with a length of 269.3 ft, and propelled by six bipropellant rocket engines each providing 583,000 lb of vacuum thrust. The position of the LOX tank and the LH_2 tank has been interchanged, the LOX feedlines removed, and the biconic nose has been redesigned to a 1.2-caliber ogive nose in order to better accommodate the forward-located canard FCA's by providing a cleaner and more uniform flow.

Then based on the review of our national heritage of LV's using aerodynamic surfaces, the review of the X–15 and Saturn series design concepts,[1] the survey of current use of aerodynamic surfaces by other nations, the generated mass properties and trajectory data for the aft-cg experimental LV, the original aerodynamic data, the U.S. Air Force Stability and Control DATCOM[9] as a preliminary design tool, and a control requirement analysis, a set of candidate FCA's were designed for wind tunnel test.

The traditional LV control requirement at MSFC is to have the ratio of the control torque to the aerodynamic torque be ≥ 1.5, i.e., the LV is to have at least 1.5 times as much control authority over the vehicle as the pitch up destabilizing aerodynamic moment. That is,

$$\mathrm{CR} = \frac{\mathrm{CT}}{\mathrm{AT}} \geq 1.5 \tag{1}$$

This control requirement is used to size the designed LV FCA's. From figure 2, using force and moment equations, it can be seen that about the cg,

$$\mathrm{CT} = T \sin \delta_E \, (E) \, \ell_E \tag{2}$$

$$\mathrm{AT} = N \, \ell_{cp} = C_{N_\alpha} \, \alpha \, Q \, S \, \ell_{cp} = C_N \, Q \, S \, \ell_{cp} \tag{3}$$

$$\ell_{cp} = X_{cp} - X_{cg} \tag{4}$$

Thus, equation (1) becomes,

$$\mathrm{CR} = \frac{T \sin \delta_E \, (E) \, \ell_E}{C_{N_\alpha} \, \alpha \, Q \, S \, \ell_{cp}} \geq 1.5 \tag{5}$$

It can be seen that about the moment reference point (MRP),

$$AT = C_{N_\alpha}\ \alpha\ Q\ S\ X_{cp} = C_m\ Q\ S\ d = C_{m_\alpha}\ \alpha\ Q\ S\ d \tag{6}$$

Therefore,

$$AT = C_{N_\alpha}\ \alpha\ Q\ S\ \frac{C_{m_\alpha}}{C_{N_\alpha}}\ d = \left(C_{m_\alpha}\ Q\right)\ \alpha\ \frac{\pi\ d^3}{4} \tag{7}$$

Equation (7) shows that the maximum AT for a fixed α occurs when $\left(C_{m_\alpha}\ Q\right)$ is a maximum.

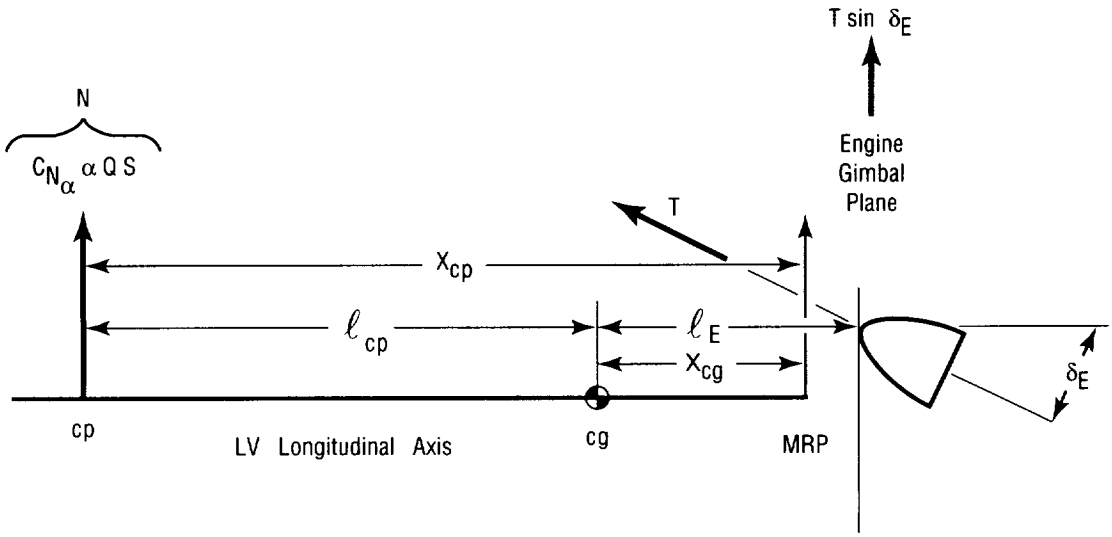

FIGURE 2. Aerodynamic torque versus engine gimbal torque.

When a LV flies through its ascent trajectory, the traditional critical point from an aerodynamic loads standpoint, it is near maximum dynamic pressure (max Q). LV control systems and structures are designed around this critical point and LV trajectories are "shaped" accordingly. For the experimental LV, figure 3 shows the variation of critical parameters during ascent, and table 1 lists the values used at max Q. Substituting the values from table 1 into equation (5) yields a control ratio of 1.3. This is inadequate controllability, since the minimum requirement is 1.5.

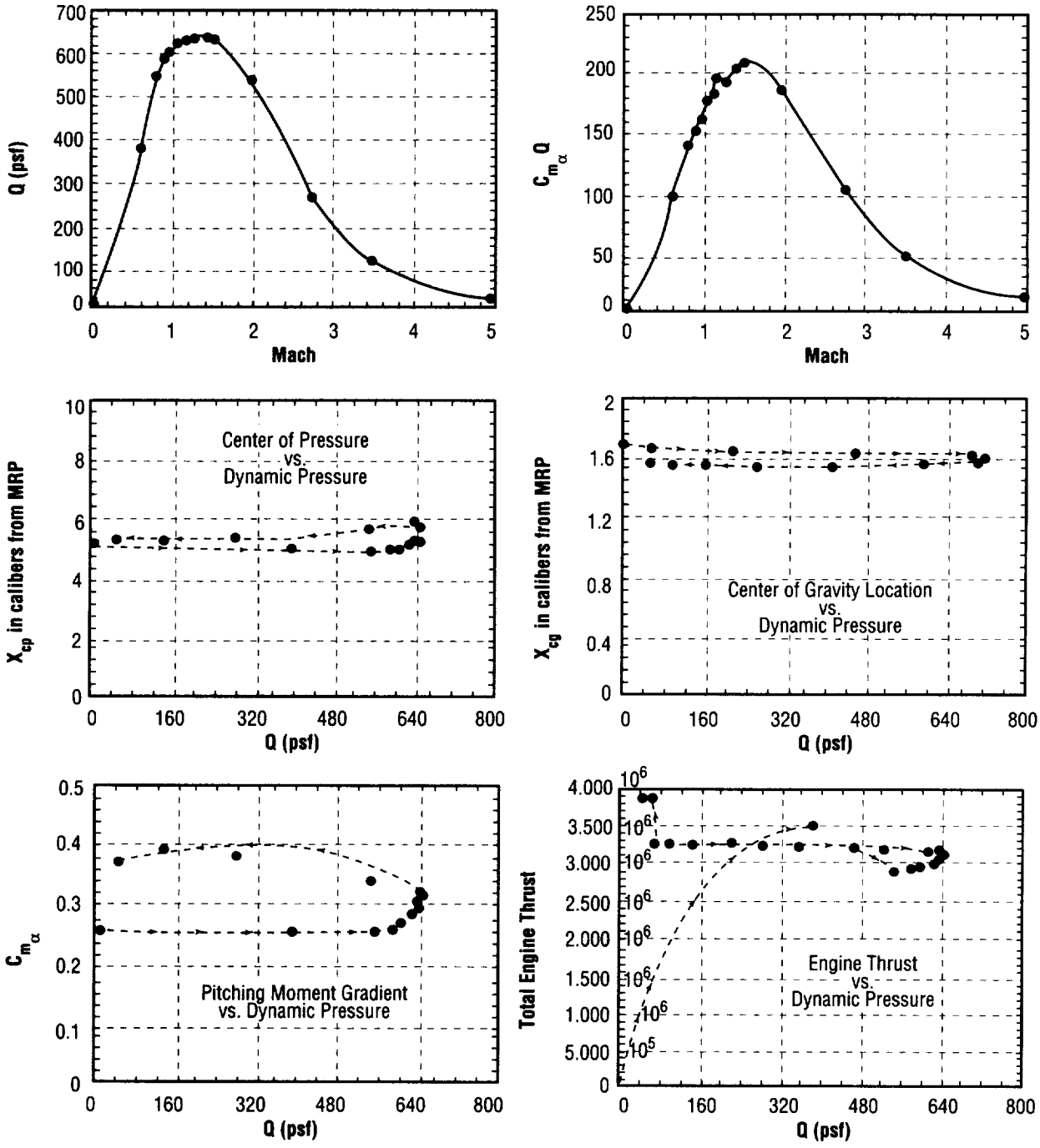

FIGURE 3. Variation in ascent parameters for the experimental LV.

TABLE 1. Experimental LV values.

$max\ Q$	=	639.9 psf
T	=	520,512 lb/engine
E	=	6
M	=	1.41
S	=	597.56 ft^2
d	=	27.58 ft
C_{N_α}	=	0.057153
C_{m_α}	=	0.321070
X_{cg}	=	52.98 ft
ℓ_E	=	53.4 ft
δ_E	=	4° (although 8° are possible, 4° is the usual number allotted to routine control)
α	=	4° (based on the maximum used during Saturn V flights)
X_{cp}	=	5.62 calibers = 155 ft
ℓ_{cp}	=	101.52 ft

III. FLIGHT CONTROL AUGMENTOR DESIGN

A. Aft Augmentors

Using equation (1) to size the all-movable FCA planform which will provide the required controllability (fig. 4),

$$CR = \frac{CT + N_F \ell_F}{AT} = \frac{T \sin\delta_E (E) \ell_E + C_{N_{\alpha_F}} (\alpha + \delta_F) Q (2) S_F \ell_F}{C_{N_\alpha} \alpha Q S \ell_{cp}} \geq 1.5 \qquad (8)$$

It is assumed here that the ratio of local dynamic pressures at the FCA location is very close to 1, that the aerodynamic center (*ac*) of the FCA is near the quarter-chord location (which is a conservative assumption), and that the moment about the FCA $\left(C_{m_{ac_F}}\right)$ is near zero, i.e., that the FCA is symmetrical without camber. The FCA's augment the control torque by shifting the LV center-of-pressure (*cp*) aft, as shown in figure 5, thereby reducing the moment arm of the resultant normal force on the vehicle. The *cp* is the point of no moment, whereas the *ac* is the point where the moment is independent of α, i.e., where C_{m_α} equals zero. For a symmetrical vehicle, *cp* = *ac*. The *cp* location is of vital concern in flight stability and control, since it determines the aerodynamic moment arm.

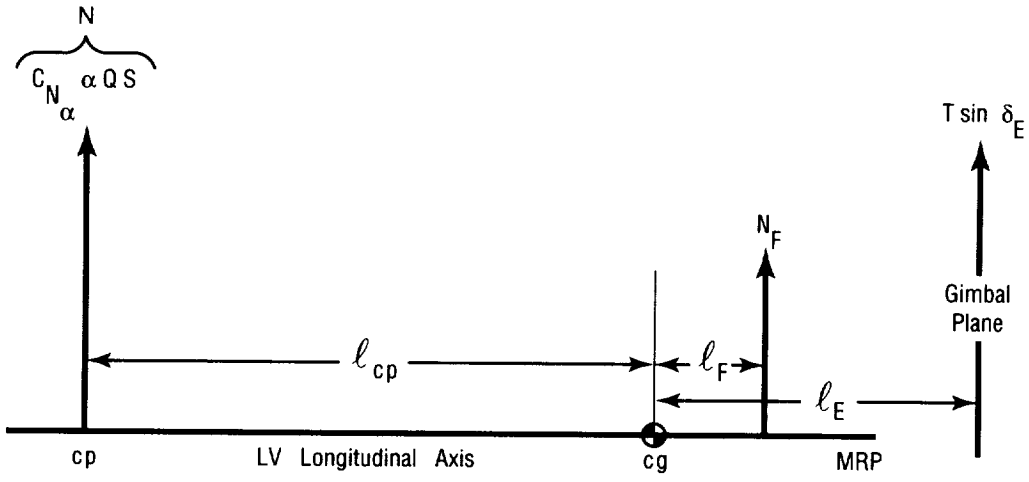

FIGURE 4. Control augmentation provided by designed FCA's.

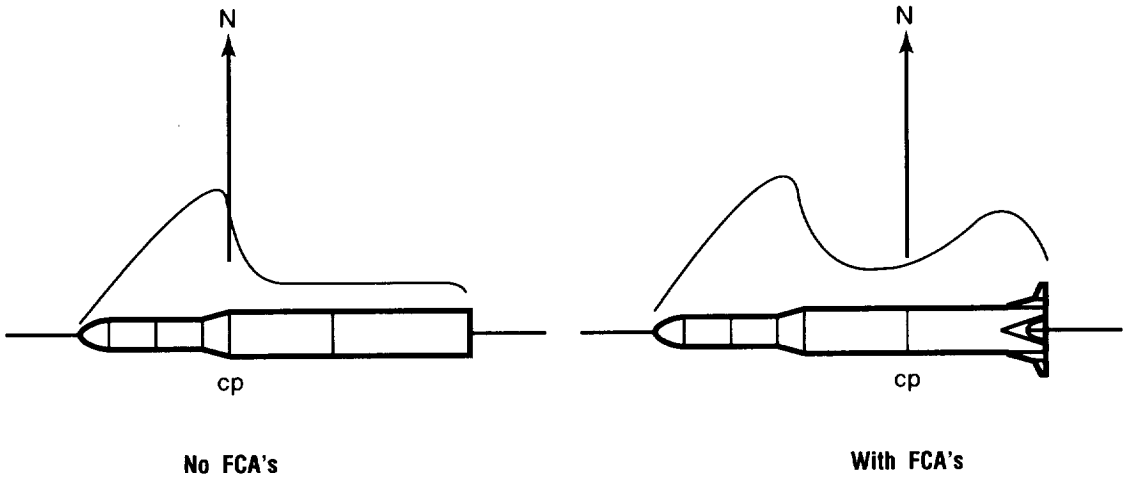

FIGURE 5. Center-of-pressure shift provided by designed FCA's.

To solve equation (8), values for $C_{N_{\alpha_F}}$ and ℓ_{cp} are needed. From previous work with Saturn V aerodynamic data the value of $C_{N_{\alpha_F}}$ as a function of M has been isolated; $C_{N_{\alpha_F}}$ = 0.1102/deg. When these values are substituted into equation (8) for the experimental LV,

δ_F (deg)	S_F (ft^2)	Engine Out S_F (ft^2)
2	44	95
		Choose 80
4	33	71

A planform area of 80 ft^2 is chosen to not only move the *cp* aft and thereby improve stability and control, but also to be able to accommodate a very far aft cg and an engine out. Choosing 80 ft^2 means that in an engine-out event, the LV control requirements would be met with < 4° of FCA deflection. The FCA's together with the thrust vector control (TVC) then provide the required control authority.

After an aerodynamic surface has been sized, the next step is to decide on a planform shape. Since the experimental LV is expendable, simple planform designs were desired for ease of fabrication. Therefore, the only other significant design issues to address were the operational speed regimes, the aspect ratio (A), the LE sweep angle (Λ), the taper ratio (τ), the airfoil, and the airfoil thickness-to-chord (t/c) ratio. During its ascent flight, the experimental LV flies through three speed regimes: subsonic, transonic, and supersonic. It has been established that the FCA's will provide the greatest assistance to the LV during the time when $C_{m_\alpha} Q$ is maximum. Since this occurs at a supersonic Mach number, the FCA's were designed for the supersonic speed

regime.All-movable FCA's were chosen since they are known to have an operational advantage in the supersonic regime. In subsonic flow, a trailing edge (TE) effect of a partially movable control surface is felt upstream. In supersonic flow, on the other hand, the forward part of a surface does not feel the effect of a deflected aft portion of a control surface. Thus, if large lift is desired, the entire surface should move. A set of four cruciform FCA's were chosen based on Saturn V success[1] and also on the fact that the experimental LV has four of its six engines located in line with the aft fuselage circumference, hence four engine shrouds which provide suitable location for four FCA's.

There are not many basic shapes of supersonic airfoils from which to choose. The basic shapes are the diamond and the lenticular. Part of a detailed study by Wood and Miller[10] showed that the lift generated by the basic diamond and the basic lenticular shapes demonstrated no discernible differences between the basic diamond and the basic lenticular airfoil. Thus, the author has chosen a variety of diamond and lenticular airfoils for the FCA designs that were wind tunnel tested. While drag minimization is a driver in many airfoil designs, it was not the case here. The aerodynamic surface drag of the vehicles studied in reference 1 was < 2 percent of the total vehicle drag. Symmetrical airfoils without camber were chosen. For the experimental LV using a set of four FCA's at 80 ft^2 each,

$$\frac{S_F}{S_{\text{wetted}}} = 1.6 \text{ percent} \tag{9}$$

The six bipropellant liquid engines of the experimental LV produce 3,500,400 lb of thrust, and the time of FCA use is 4 min.

Blunt rather than sharp TE's can be used on a LV, since FCA drag is normally < 2 percent of the total vehicle drag. Blunt TE's have been used successfully in many previous LV's, as cited in reference 1. The blunt TE was used for many reasons, including avoidance of transonic problems, ease of fabrication, utility for holddown posts, structural rigidity to help prevent flutter, and, in the case of the X–15, for better high-speed directional control.[1] Blunt TE's have also been used to solve transonic problems on French sounding rockets such as the D6 (ONERA).[11] ONERA in France had the transonic problem of shock-induced boundary layer separation on the downstream part of airfoils used on the base of the first stage. This transonic boundary layer separation resulted in decreased stability and increased load factors. The transonic problem was corrected by the use of thick TE's, and it was found that the wedge shape experienced no transonic problems and produced much improvement in static flight stability.[11]

Better control effectiveness was what was being sought here for the designed FCA's. As shown in reference 1, none of the blunt TE surfaces of the Saturn series moved, so the amount of increased control effectiveness on a LV was not known. Could the increased control effectiveness of the blunt TE achieved on the X–15 be realized on a LV? The blunt TE also helps to avoid some transonic problems of fluctuating C_m and negative local lift due to transonic shocks. The blunt TE was also structurally appealing for possible future insertion of reaction control systems (RCS) and/or smart actuator mechanisms due to the space available in a blunt TE airfoil. Therefore, the FCA's designed incorporate blunt TE's.

While there is some preference for triangular planforms for supersonic speeds because of smaller *cp* shifts in going from subsonic to supersonic speeds, more vortex lift and more negative pitching moments, and there is some preference for trapezoidal planforms for subsonic speeds, the recent literature shows that

wind tunnel test is still being used extensively to make final decisions on planform shape parameters and also to increase databases so that current aerodynamic prediction codes can be further refined.

A total of 12 candidate FCA's have been designed and wind tunnel tested at MSFC: 11 aft FCA's and 1 forward canard FCA. The fabricated aft FCA's are shown in figure 6 and described in table 2. Since the critical design point is supersonic, eight triangular family aft FCA's and a triangular canard were chosen. Based on Saturn IB LV success,[1] four FCA's have $\Lambda = 45°$; based on Saturn V LV success,[1] four FCA's have $\Lambda = 30°$. The eight FCA's in the triangular family were all originally true triangles, however for launch pad logistics (and structural/fabrication considerations), some of the tips were clipped. These clipped-tip designs are of course strictly trapezoids. For comparison to the triangular planform families, an aft swept, forward swept, and trapezoidal tapered planform, all with diamond airfoils, have been used. Aspect ratios ranged from 1.74 to 5.625. Figure 7 shows the fabricated forward canard FCA's. Figure 8 shows the wind tunnel test model with aft FCA's. Figure 9 shows the wind tunnel test model with forward and aft FCA's.

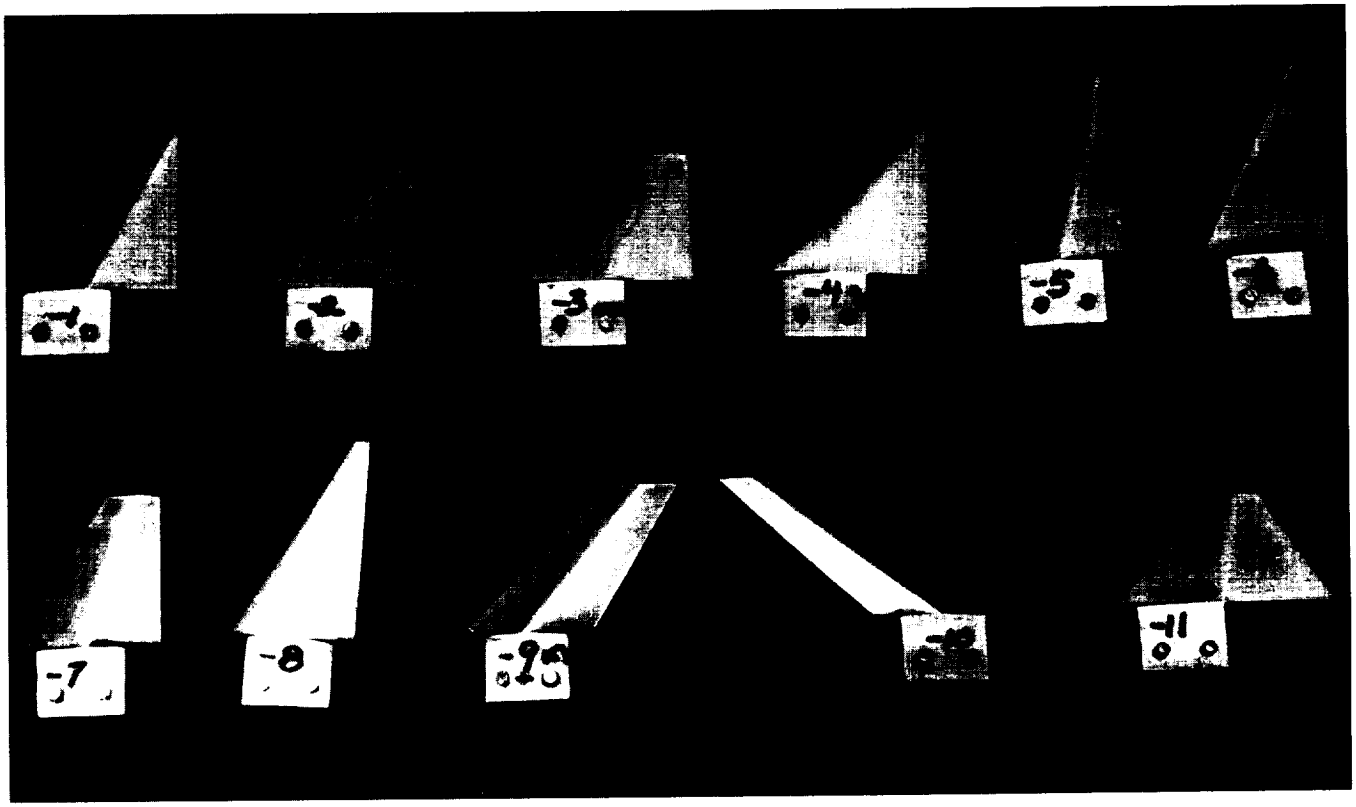

FIGURE 6. Fabricated aft FCA designs.

TABLE 2. Candidate FCA design descriptions.

4 triangular family planforms; LE $\Lambda = 45°$; TE = 0°
- 1 full diamond airfoil (#1)
- 1 half diamond; blunt TE (#2)
- 1 full diamond; clipped tip (#3)
- 1 lenticular airfoil (#4)

4 triangular family planforms; LE $\Lambda = 30°$; TE = 0°
- 1 full diamond airfoil (#5)
- 1 half diamond; blunt TE (#6)
- 1 full diamond; clipped tip (#7)
- 1 lenticular airfoil (#8)

1 aft swept trapezoidal planform; LE $\Lambda = 45°$; TE = 30° (#9)
1 forward swept trapezoidal planform; LE $\Lambda = -45°$; TE = −55° (#10)
1 tapered trapezoidal planform; LE $\Lambda = 45°$; TE = −30° (#11)
1 triangular planform canard; half diamond; blunt TE (#12)

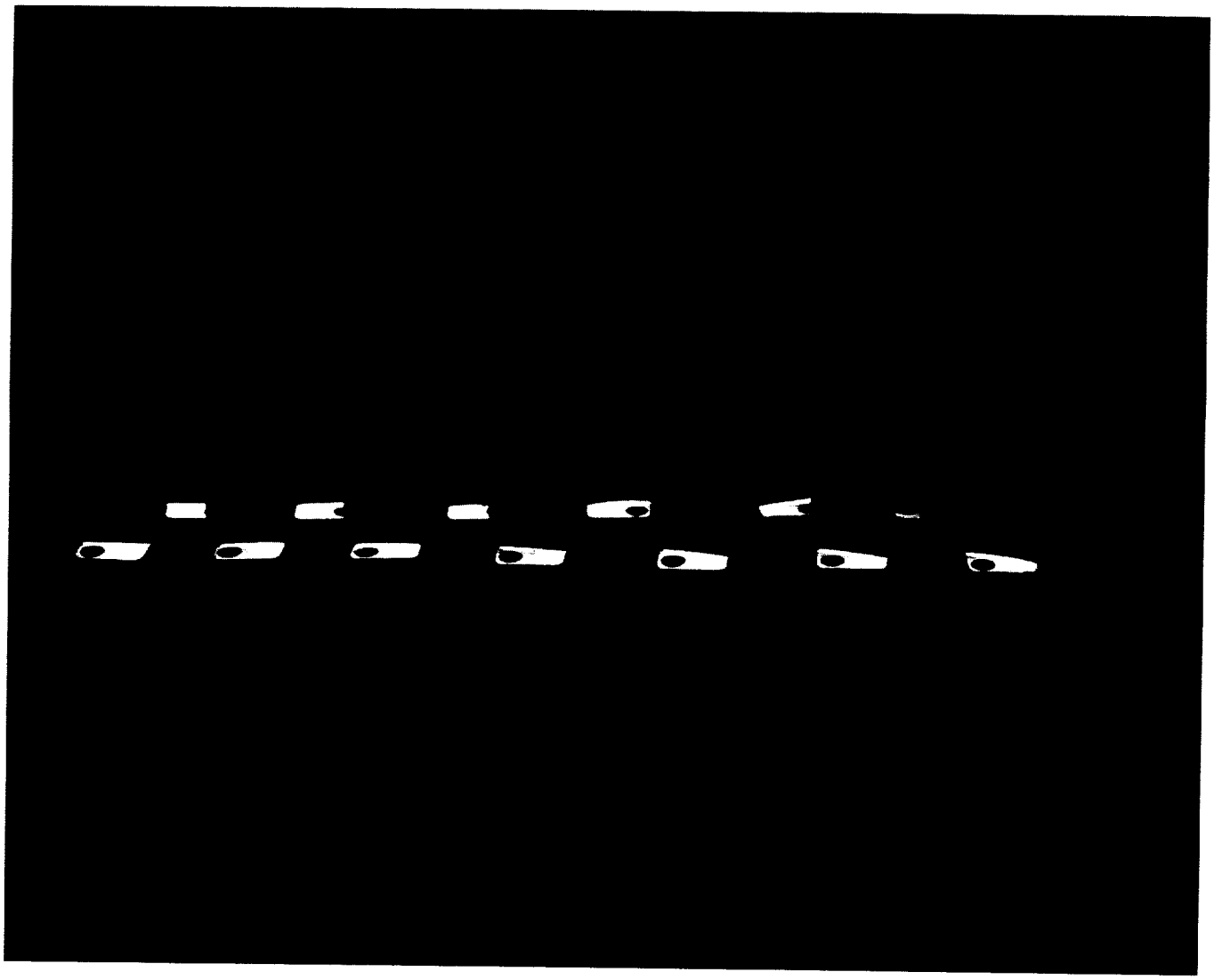

FIGURE 7. Fabricated forward FCA's.

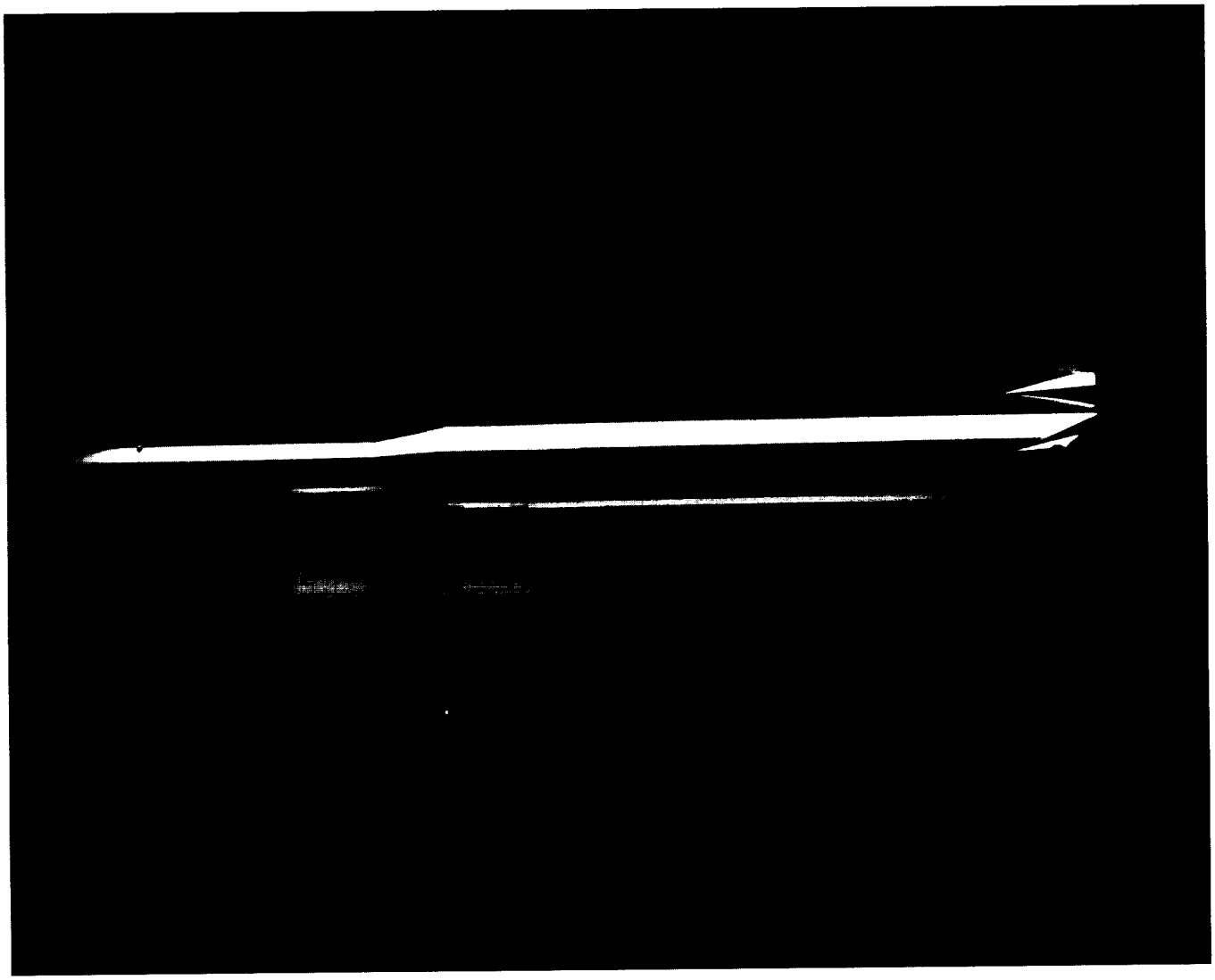

FIGURE 8. Wind tunnel test model with aft FCA's.

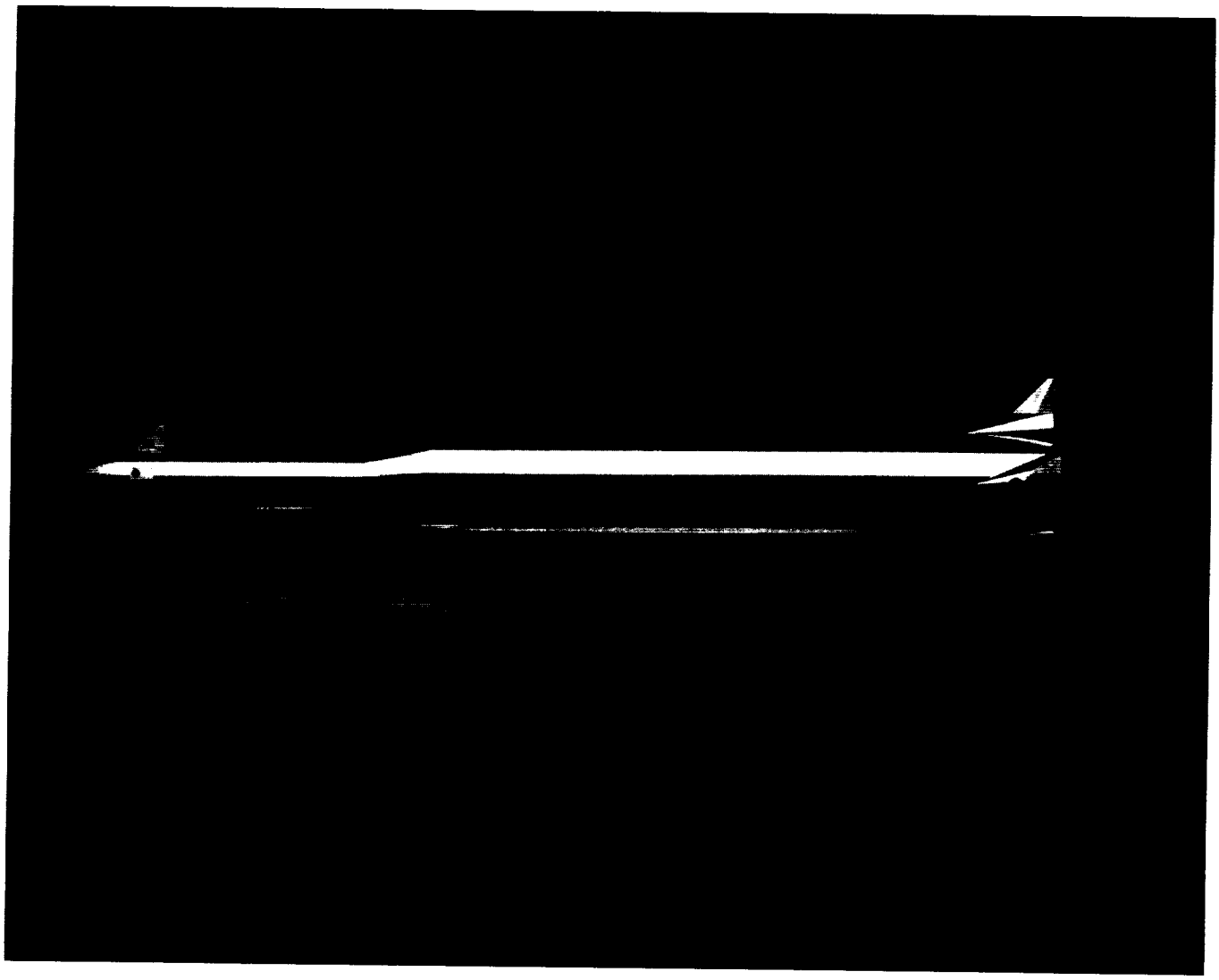

FIGURE 9. Wind tunnel test model with forward and aft FCA's.

B. Canard Design

It is well known that an aerodynamic flight control surface normally located forward of the cg on a flight vehicle produces an effect which is destabilizing to its static stability. Although canards cause static instability, they have been used extensively on subsonic and supersonic aircraft and missiles for a variety of reasons. Some advantages provided by canard usage include: production of lift at the nose, high maneuverability due to fast response time, and reduced trim drag in cruise flight. For example, a canard has been investigated for the Shuttle Orbiter to produce an additional nose-up pitching moment, which would allow a more forward cg location, and trim out the nose-down pitching moment created by the down-elevon deflection. The Orbiter forward cg is limited to 0.65 reference body length (Operational Design Data Book, Rockwell, 1991), which restricts its payload carrying capability. Some of these studies have been conducted by NASA Ames Research Center (ARC). Deployable canards have also been studied to provide positive (nose-up) pitch authority in the landing phase and relax the pilot workload.

The objective of this research is to augment the deficient control torque due to an aft cg location. The traditional use of canards is to treat forward cg problems, and traditional usage would exacerbate an aft cg problem. However, a nontraditional canard control can be used here to provide negative lift on the nose and a pitch-down torque which would achieve the control objectives. For the application here, the vortices from the canards onto the LV empennage must be considered, as the canard downwash acting on the empennage can reduce the FCA control effectiveness. Since the location of the FCA's on the experimental LV has been selected, based on the location of the six engines and four engine shrouds, the canards are aligned with the FCA's in the same manner. The biconic nose of the experiment LV has been redesigned to provide cleaner and more uniform flow in proximity to the canard controls. The 1.2–caliber ogive nose accommodates the canards as shown below. The longitudinal body station location of the canards is sometimes a trade between distancing from the bow and oblique shocks and their effects on the control authority of the canards, and the structural considerations of having the canards located at a major bulkhead. The canards have been located on the payload bay bulkhead for structural considerations.

For completeness in this research, a set of cruciform canards has been designed by using linearized supersonic theory for the canard lift coefficient, along with the same moment balance method used above and shown in figure 10. Using equation (1), in the same manner as in section 5.2 for the aft FCA's, the all-movable canard planforms which will provide the required controllability are sized,

$$\mathrm{CR} = \frac{CT + N_C \ell_C}{AT} = \frac{T \sin \delta_E (E) \ell_E + C_{N_C} Q\ 2\ S_C \ell_C}{C_{N_\alpha} \alpha Q S \ell_{cp}} \geq 1.5 \qquad (10)$$

and

$$C_{N_c} = \frac{4 (\alpha + \delta_c) \text{ (in radians)}}{\sqrt{M_\infty{}^2 - 1}} \qquad (11)$$

It is assumed here that the ratio of local dynamic pressure at the canard location is very close to 1, that the *ac* of the canard is near the half-chord location (which is the conservative assumption for the canard), and that the moment about the canard $\left(C_{m_{ac_C}}\right)$ is near zero, i.e., that the canard is symmetrical and without camber.

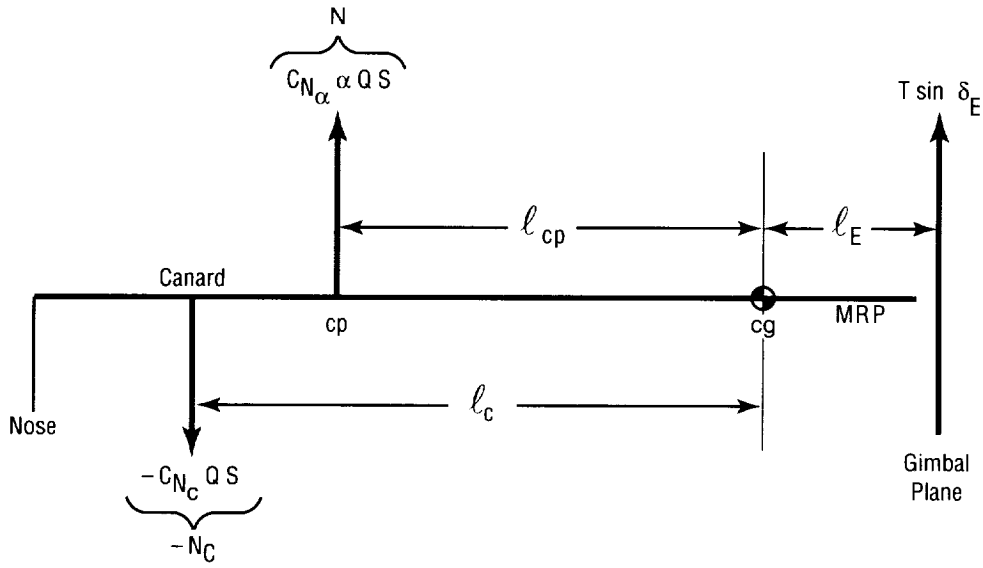

FIGURE 10. Canard control augmentation.

For the experimental LV, equation (11) becomes

$$C_{N_C} = 4.024\ (0.06981 + \delta_C)\ ;\ \text{and}\ \ \ell_C = 147.64\ \text{ft}\ .$$

When these values are substituted into equation (10) along with the values used in table 1,

δ_C°	S_C (ft^2)
7	43.74
8	32.80
9	26.24

Choose $S_C = 32$ ft^2

Figure 11 shows the designed triangular 32 ft^2 canard planform and the fuselage location selection factors. One set of four in line with the aft FCA locations was used. They have blunt TE's, are hinged at their TE's, and located on the LV fuselage 1.2 calibers from the tip of the ogive nose. This location on the payload bay forward bulkhead is not only advantageous for structural reasons, but it is believed the canards will be free of the bow or oblique shock wave emanating from the LV nose. It is also felt that this location is far enough forward on the fuselage to prevent any serious blanketing of aft FCA's, if they are used simultaneously, from the canard vortex downward. Table 3 summarizes the canard design parameters used for simplicity.

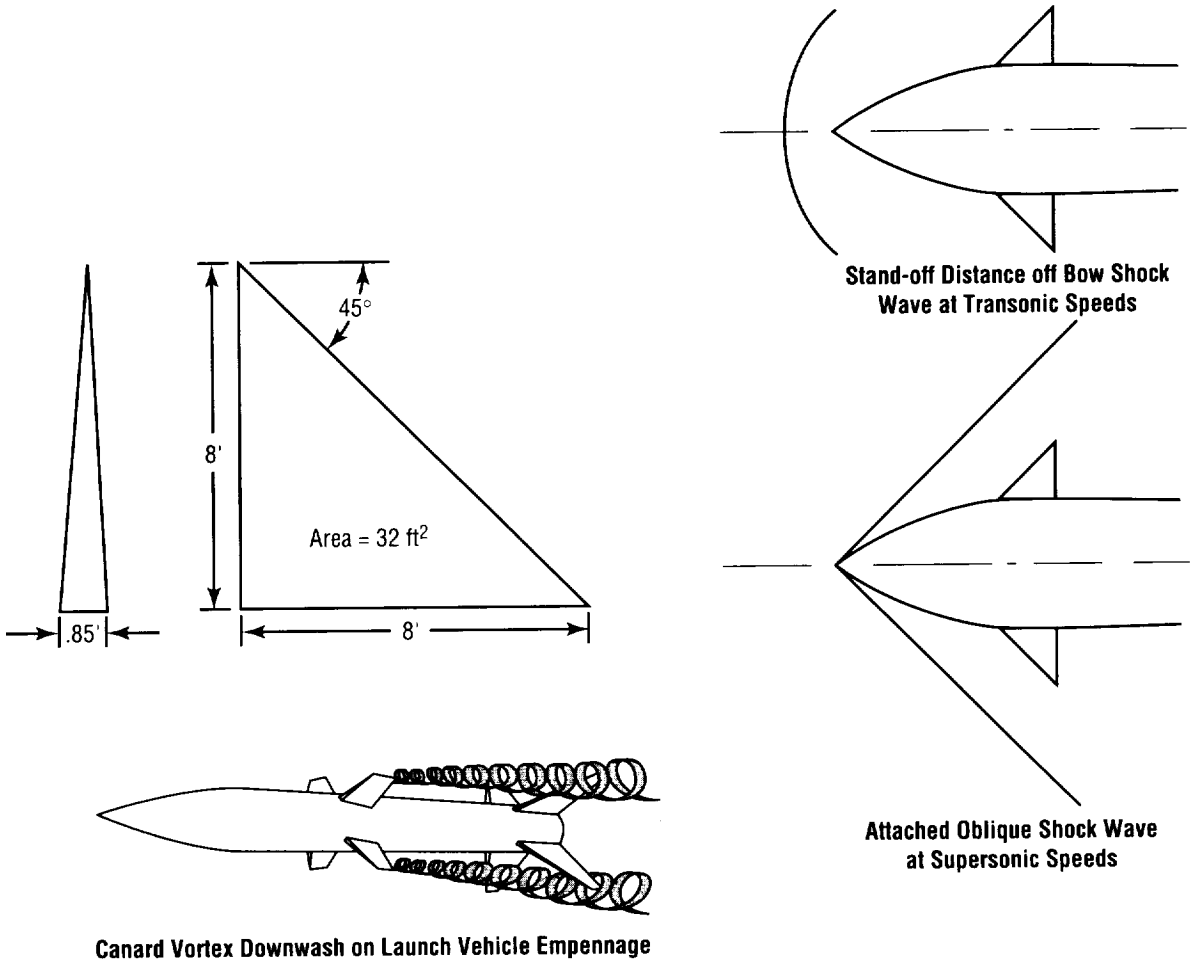

FIGURE 11. Canard surface planform design and factors in selecting location on launch vehicle fuselage.

TABLE 3. Canard design parameters.

Redesigned nose to accommodate canard controls:
Biconic redesigned to 1.2 caliber ogive nose
Canard controls:
Four cruciform triangular planforms
Span = 16 ft
Root chord = 8 ft
Leading edge sweep = 45°
Airfoil = 0.85 ft ramp
Longitudinal placement = 1.2 calibers from nose tip

C. Options for Increased Control Effectiveness

The Shuttle aerodynamic flight control surfaces become effective approximately 10 sec into the launch ascent trajectory, at which time Q is of sufficient magnitude. As an added way to increase the torque provided by the designed FCA's, RCS could be employed in the blunt TE's or the concept of jet flaps could be employed, since the blunt TE's provide additional space. In the jet flap concept, a propulsive jet can be emitted from the TE of the FCA, as shown in figure 12, with the primary objective of increasing the lift of the surface, hence control moment. Also, a recent investigation (Arena, Nelson, and Schiff; 1993) has shown that an effective technique for generating control torque when conventional control surfaces lose their effectiveness is to use pneumatic blowing through a chined forebody. Again, these additions could be explored if the surfaces were needed to be more effective sooner than 10 sec into the ascent, e.g., for very reduced wind restrictions at liftoff. In the upper portion of the ascent, once the FCA's have ceased to be effective they can be dropped off perhaps with the engines, since this is an expendable LV.

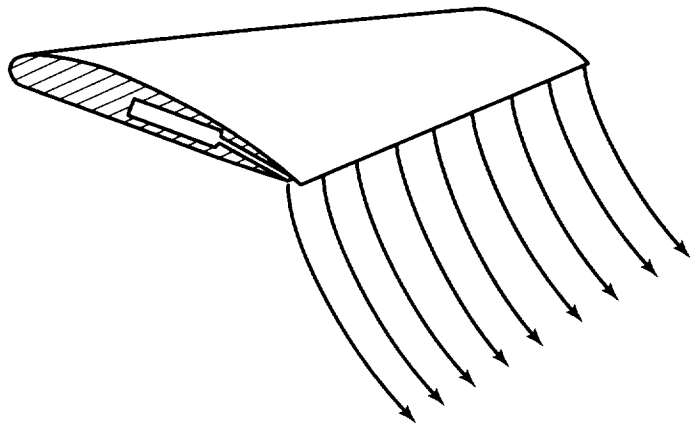

FIGURE 12. Flight control augmentor with internally ducted jet.

IV. WIND TUNNEL TEST PROGRAM

The static stability wind tunnel test program conducted at the NASA MSFC wind tunnel test facility obtained force and moment data from which the stability derivatives and control derivatives were calculated for the flight stability and control analysis. The tests measured normal, axial, and side forces; pitching, yawing, and rolling moments; and were conducted at Mach numbers from 0.2 to 5, an α and β range of $\pm 10°$, aft FCA deflections up to 15° in 3° increments, and forward FCA deflections of up to 30° in 5° increments. The three forces and three moments were measured on a six-component strain gauge balance mounted internally in the experimental LV test article. The MSFC wind tunnel used in this research was the 14 × 14-Inch Trisonic Wind Tunnel.[12] The test articles were fabricated from stainless steel to a scale of 0.5 percent by Dynamic Engineering Incorporated. Figure 13 shows a diagram of the test LV with its 1.2–caliber ogive nose redesign, canard locations, engine shrouds, aft FCA's, balance center, and MRP. The tests were conducted with and without the canard forward FCA's. Table 4 shows wind tunnel operating conditions and table 5 shows wind tunnel test data tolerances.

TABLE 4. Wind tunnel operating conditions.

Mach Number	Reynolds Number ($\times 10^6$/ft)	Dynamic Pressure (lb/in^2)	Stagnation Temperature (°F)	Stagnation Pressure (lb/in^2)
0.20	1.6	0.58	100	22
0.40	3.4	2.21	100	22
0.80	5.5	6.47	100	22
0.95	6.2	7.76	100	22
1.20	6.5	9.15	100	22
1.46	6.0	9.49	100	22
1.96	7.2	11.00	100	30
2.74	4.7	6.38	140	30
3.48	4.8	5.15	140	45
4.96	4.4	2.73	140	80

TABLE 5. Wind tunnel test data tolerances.

Strain Gauge Balance 250			
Capacity		Accuracy	Max Loads*
NF (lb)	200	+1.00	21
SF (lb)	107	+0.50	4.5
AF (lb)	75	+0.25	12
PM (in-lb)	200	+0.99	14
RM (in-lb)	50	+0.25	1.5
YM (in-lb)	107	+0.49	16

*Maximum estimated running loads and not starting loads.

Coefficient Tolerances

Mach No.	Dynamic Pressure	C_N	C_m	C_A	C_Y	C_n	C_ℓ
0.20	0.58	0.8057	0.4819	0.2014	0.4028	0.2385	0.1217
0.40	2.21	0.2114	0.1265	0.0529	0.1057	0.0626	0.0319
0.80	6.47	0.0722	0.0432	0.0181	0.0361	0.0214	0.0109
0.95	7.76	0.0602	0.0360	0.0151	0.0301	0.0178	0.0091
1.20	9.15	0.0511	0.0305	0.0128	0.0255	0.0151	0.0077
1.46	9.49	0.0492	0.0295	0.0123	0.0246	0.0146	0.0074
1.96	11.00	0.0425	0.0254	0.0106	0.0212	0.0126	0.0064
2.74	6.38	0.0732	0.0438	0.0183	0.0366	0.0217	0.0111
3.48	5.15	0.0907	0.0548	0.0227	0.0454	0.0269	0.0137
4.96	2.73	0.1712	0.1024	0.0428	0.0856	0.0507	0.0259

The dynamic stability wind tunnel test program obtained the damping derivatives for three selected FCA's tested on the experimental LV for a deflection range of 0° to 15° and a Mach range of 0.8 to 1.96, so that dynamic stability characteristics could be compared. Many wind tunnel techniques are available for dynamic stability testing. NASA Langley Research Center has typically used forced oscillation of 0.5–1.5 Hz, but their wind tunnels are larger than the one used at MSFC for this test. To facilitate the logistics, a free oscillation with a mechanical release was chosen. Free oscillation is the simplest of the oscillatory techniques and lends itself well to automatic computer processing. It is usually limited to measurement of direct damping derivatives, and involves the evaluation of a decaying oscillatory motion performed by an elastically suspended model following some initial disturbance. The initial disturbance may include a mechanical release from a displaced position, an application of a mechanical impulse, or an excitation at resonance and sudden interruption of the source of excitation. The decaying oscillations are recorded. From this data the frequency and the damping, expressed as the log increment of amplitude, can be measured.

The oscillation was 2° about $\alpha = 0°$. Figure 14 shows the aluminum dynamic wind tunnel test model in the MSFC wind tunnel. Figure 15 shows the detail of the dynamic adapter assembly. Figure 16 shows the variable porosity walls used at the transonic speeds and described in reference 12.

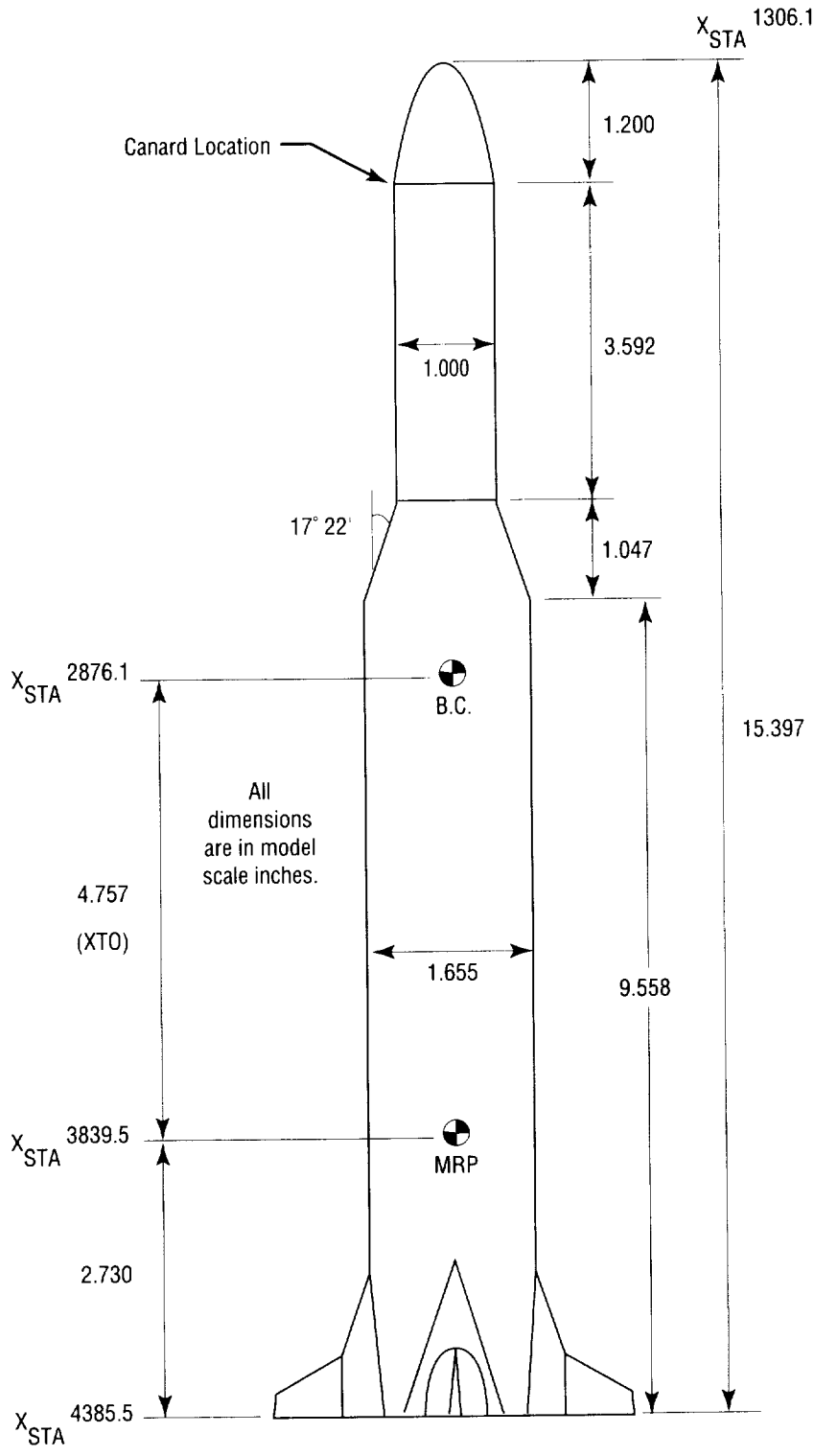

FIGURE 13. Static stability wind tunnel model (0.005 scale).

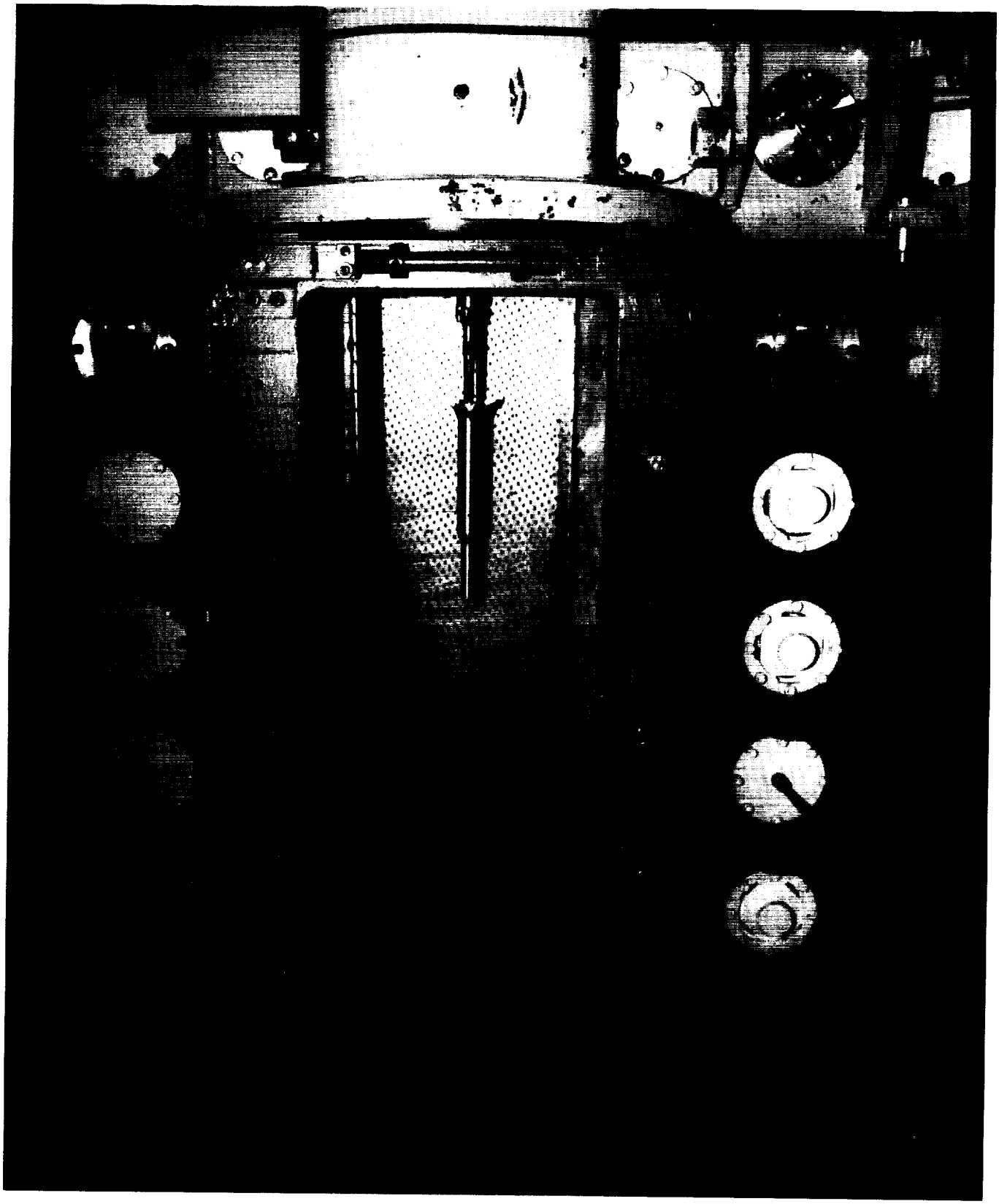

FIGURE 14. Dynamic wind tunnel test setup.

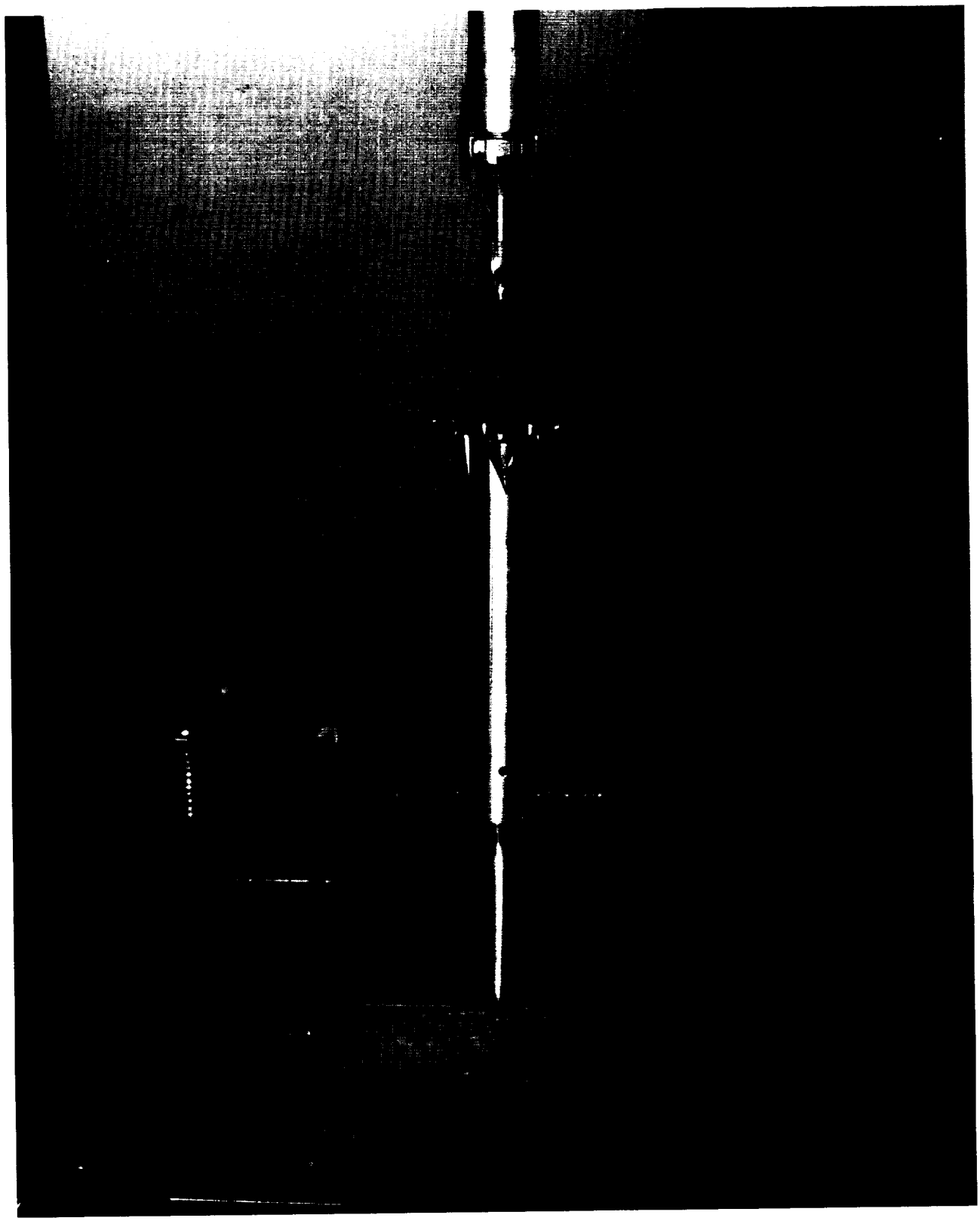

FIGURE 15. Dynamic wind tunnel test adapter assembly.

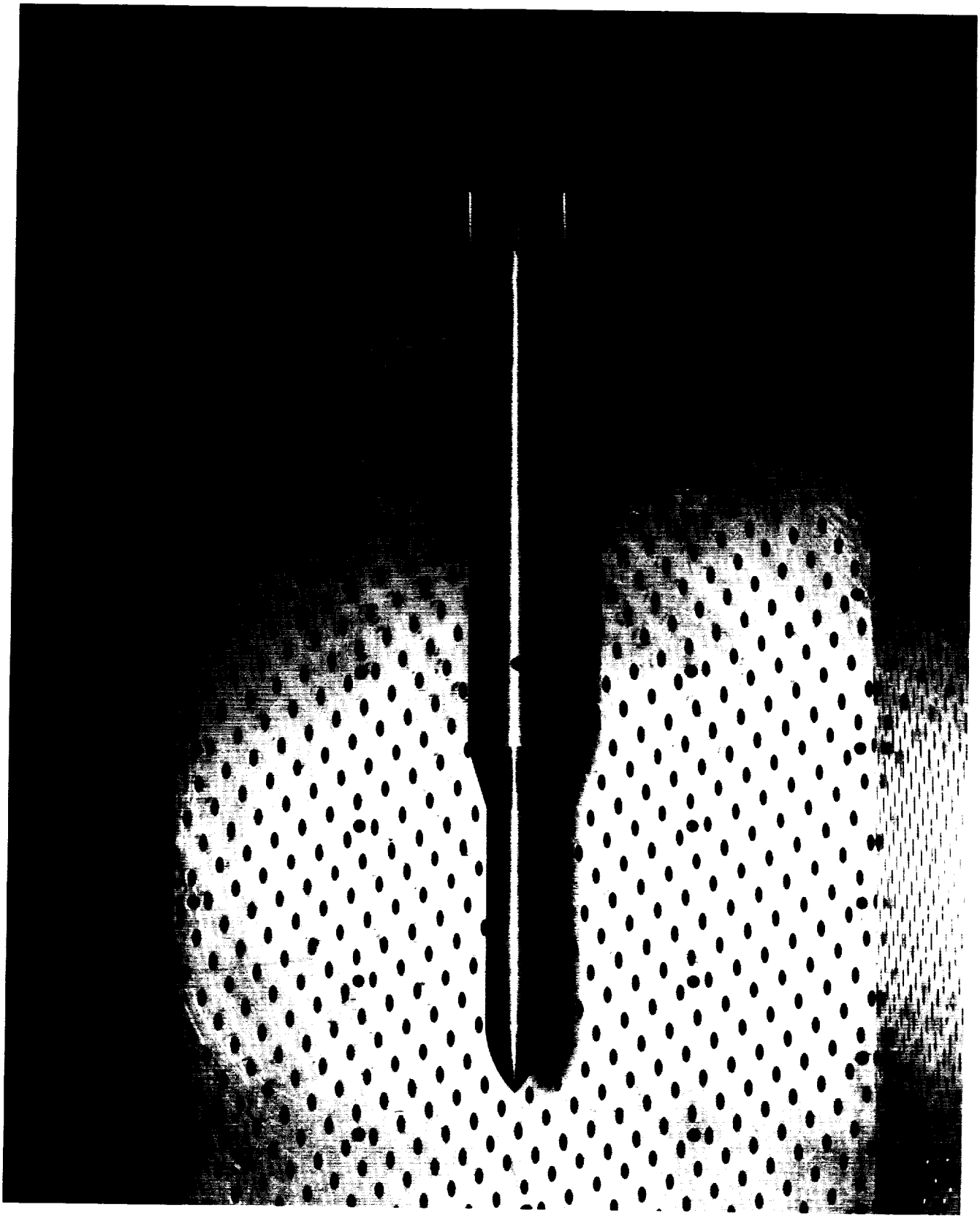

FIGURE 16. Variable porosity walls used in the transonic range.

V. STABILITY AND CONTROL ANALYSES

A. Static Stability Analysis

Wind tunnel test data were reduced and linearized to obtain the stability derivatives, i.e., the rates of change of the three forces (normal, axial, and side) and the three moments (pitching, yawing, and rolling) with respect to α and β,

$$\frac{\partial C_N}{\partial \alpha}, \quad \frac{\partial C_m}{\partial \alpha}, \quad \frac{\partial C_A}{\partial \alpha}, \quad \frac{\partial C_Y}{\partial \beta}, \quad \frac{\partial C_n}{\partial \beta}, \quad \frac{\partial C_\ell}{\partial \beta}$$

at fixed M, and the control derivatives, i.e., the rates of change of the forces and the moments with respect to the FCA deflections at fixed M,

$$\frac{\partial C_N}{\partial \alpha}, \quad \frac{\partial C_m}{\partial \alpha}, \quad \frac{\partial C_A}{\partial \alpha}, \quad \frac{\partial C_Y}{\partial \beta}, \quad \frac{\partial C_n}{\partial \beta}, \quad \frac{\partial C_\ell}{\partial \beta} \quad \text{and} \quad X_{cp},$$

the *cp* locations. The basic stability derivatives were tabulated as slopes of coefficients versus aerodynamic angle curves for fixed FCA deflections. The basic control derivatives were tabulated as slopes of coefficients versus FCA deflection curves for fixed aerodynamic angles.

The criteria for longitudinal static stability of a flight vehicle are,

$$C_{m_\alpha} < 0 \tag{12}$$

and for α_{trim} to be in the flight range of the vehicle. The vehicle C_{m_α} varies with the cg position. As the cg of a stable vehicle moves farther aft, C_{m_α} becomes less and less negative. When the C_{m_α} has become positive, the vehicle becomes longitudinally unstable. That cg location at which $C_{m_\alpha} = 0$ is the neutral point (NP), the *ac* for the entire flight vehicle, that place where the pitching moment is invariant with α. The longitudinal static margin (SM) (fig. 17) is the quantitative measure of longitudinal static stability used here. The SM is defined as the distance forward of the NP that the cg is located. Of course, when the cg is located aft of the NP, the SM is negative and the vehicle is longitudinally unstable. Early LV's were statically stable; today, most are unstable and the control systems provide artificial stability. As a LV's SM becomes more negative, the requirements for control torque increase.

From equation (6) or a derivation such as found in reference 13, the static margin can be defined in terms of the calculated longitudinal static stability parameters,

$$SM \equiv -\frac{C_{m_\alpha}}{C_{N_\alpha}} \text{ (in calibers)} \tag{13}$$

For the experimental expendable LV in the ascent trajectory, the static flight stability has been assessed. Only the longitudinal static flight stability is presented here. The SM's and the locations of the vehicle *cp* (X_{cp}) have been determined first for the cases of no FCA's at each Mach number, and then for the cases with each of the different FCA's tested at each Mach number but with zero FCA deflection, and finally each FCA with deflection at each Mach number in order to assess the improvement in static flight stability and *cp* shift provided by each of the FCA designs during ascent. The FCA's with the greatest aspect ratio had the greatest normal force gradient. Table 6 presents some of the calculated longitudinal static stability parameters. Figures 18–29 show the static stability results for the experimental LV with no FCA's, and with each of the 11 different designed sets of aft FCA's. From figure 18 it can be seen that the normal force gradient of the experimental LV with no FCA's hovers around 0.08; the pitching moment gradient at max Q is approximately 0.2; the very best SM is –2.0, and the *cp* location is approximately 4 calibers from the aft end of the vehicle. Dramatic flight stability improvements can be seen in all the aft FCA designs tested. It can be seen in figure 24 that the C_{N_α} improves to more than 0.124, the C_{m_α} plunges desirously toward the negative, the SM has a best value of –0.5, and the *cp* has been shifted considerably aft. The FCA's with the greatest aspect ratio had the greatest normal force gradient. Table 7 summarizes the results of the aft FCA's. Improvements ranged from 41 percent to 72 percent, with the blunt TE design No. 6 giving the greatest improvement.

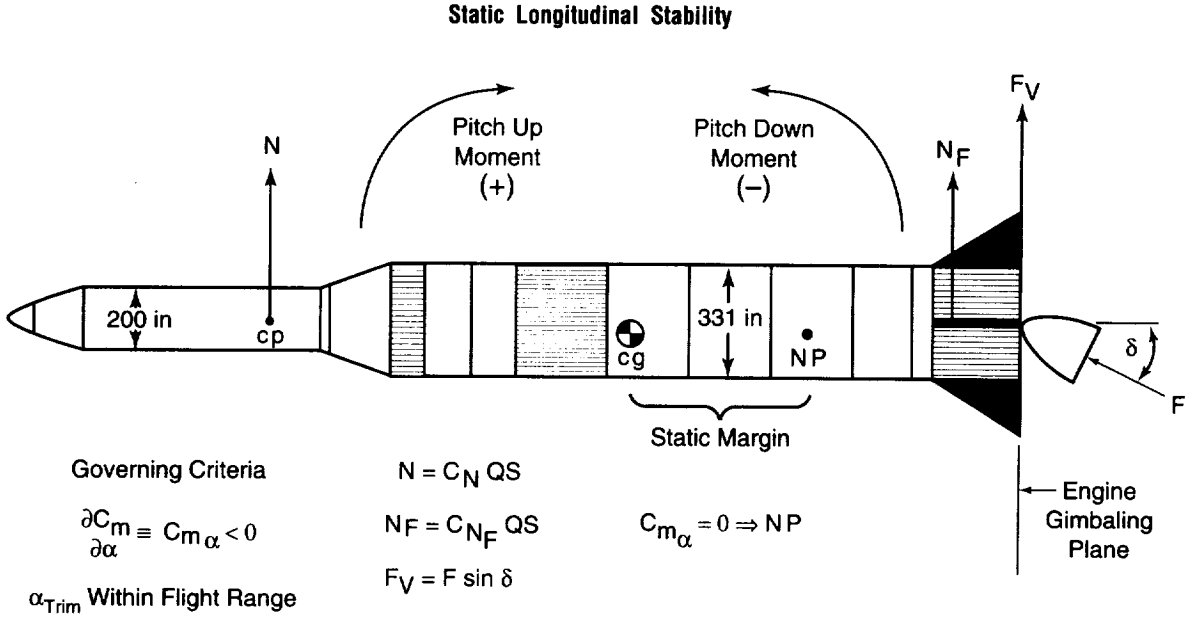

FIGURE 17. Static longitudinal stability of the experimental LV.

TABLE 6. Calculated longitudinal static stability parameters.

C_{N_α}	C_{m_α}	M	SM	X_{cp} From Aft End
No FCA's				
0.077372	0.15056	0.80	−1.9459	3.594
0.07868	0.15663	0.95	−1.9907	3.639
0.082689	0.17106	1.20	−2.0687	3.717
0.079187	0.18489	1.46	−2.3348	3.983
0.075104	0.19899	1.96	−2.6495	4.298
0.083023	0.21004	2.74	−2.5299	4.178
0.082002	0.21560	3.48	−2.6292	4.277
0.091236	0.20955	4.96	−2.2968	3.945
FCA #1 $\delta = 0°$				
0.099690	0.099983	0.80	−1.0029	2.6509
0.10402	0.095502	0.95	−0.91811	2.5661
0.109740	0.13015	1.20	−1.186	2.834
0.101380	0.15351	1.46	−1.5142	3.162
0.088601	0.17795	1.96	−2.0084	3.656
0.09280	0.18635	2.74	−2.0081	3.656
0.087482	0.19801	3.48	−2.2634	3.911
0.094358	0.19948	4.96	−2.1141	3.762
FCA #2 $\delta = 0°$				
0.10528	0.093632	0.80	−0.88936	2.5374
0.109966	0.10344	0.95	−0.94063	2.5886
0.11264	0.12034	1.20	−1.06839	2.7164
0.10326	0.16128	1.46	−1.5619	3.2099
0.10222	0.18884	1.96	−1.8474	3.4954
0.101698	0.20211	2.74	−1.98735	3.6354
0.09794	0.211667	3.48	−2.1612	3.8092
0.10490	0.19731	4.96	−1.88096	3.529
FCA #3 $\delta = 0°$				
0.09918	0.11368	0.80	−1.1462	2.7942
0.103336	0.117918	0.95	−1.1411	2.7891
0.10647	0.13574	1.20	−1.2749	2.9229
0.10118	0.15105	1.46	−1.49288	3.1409
0.09359	0.18060	1.96	−1.9297	3.5777
0.09357	0.19095	2.74	−2.0407	3.6887
0.08836	0.191127	3.48	−2.16305	3.8111
0.099694	0.20558	4.96	−2.0630	3.7110
FCA #4 $\delta = 0°$				
0.099630	0.11869	0.80	−1.19130	2.839
0.10218	0.12028	0.95	−1.1771	2.825
0.10566	0.15581	1.20	−1.4747	3.123
0.098674	0.16090	1.46	−1.63066	3.279
0.096698	0.17906	1.96	−1.85175	3.5
0.099144	0.19011	2.74	−1.91752	3.566
0.08991	0.18692	3.48	−2.0789	3.737
0.10592	0.20566	4.96	−1.94164	3.59

TABLE 6. (continued).

C_{N_α}	C_{m_α}	M	SM	X_{cp} From Aft End
FCA #5 $\delta = 0°$				
0.10869	0.09955	0.80	−0.91591	2.564
0.11436	0.08850	0.95	−0.7739	2.422
0.11396	0.124375	1.20	−1.09139	2.739
0.10438	0.14710	1.46	−1.40931	3.057
0.09609	0.174545	1.96	−1.81647	3.465
0.097064	0.18572	2.74	−1.91335	3.561
0.098096	0.19644	3.48	−2.0025	3.650
0.10609	0.208325	4.96	−1.9628	3.611
FCA #6 $\delta = 0°$				
0.11206	0.081324	0.80	−0.72572	2.374
0.12435	0.07026	0.95	−0.56506	2.213
0.12118	0.11205	1.20	−0.92465	2.573
0.10962	0.13284	1.46	−1.21178	2.86
0.10592	0.16970	1.96	−1.6022	3.250
0.099992	0.18741	2.74	−1.87423	3.522
0.098173	0.19814	3.48	−2.0182	3.666
0.15946	0.20144	4.96	−1.2632	2.911
FCA #7 $\delta = 0°$				
0.10027	0.10192	0.80	−1.01644	2.664
0.11251	0.09041	0.95	−0.803565	2.452
0.1108	0.1276	1.20	−1.1516	2.8
0.10269	0.15396	1.46	−1.4993	3.147
0.09727	0.17779	1.96	−1.8278	3.476
0.10129	0.20624	2.74	−2.03615	3.684
0.09797	0.20079	3.48	−2.0495	3.698
0.10639	0.18804	4.96	−1.7675	3.415
FCA #8 $\delta = 0°$				
0.11928	0.09747	0.80	−0.81716	2.465
0.011862	0.088773	0.95	−0.74838	2.396
0.11282	0.1258	1.20	−1.1150	2.763
0.10202	0.14912	1.46	−1.46166	3.11
0.096823	0.17788	1.96	−1.8372	3.485
0.10069	0.18865	2.74	−1.8736	3.522
0.10248	0.18655	3.48	−1.82037	3.468
0.095482	0.19311	4.96	−2.0225	3.670
FCA #9 $\delta = 0°$				
0.10258	0.10786	0.80	−1.05144	2.699
0.10519	0.10775	0.95	−1.0243	2.672
0.10683	0.13062	1.20	−1.22267	2.871
0.10173	0.15293	1.46	−1.50325	3.151
0.091627	0.17191	1.96	−1.8762	3.524
0.095177	0.195	2.74	−2.0488	3.697
FCA #10 $\delta = 0°$				
0.10697	0.11204	0.80	−1.0474	2.695
0.11179	0.106996	0.95	−0.95712	2.605
0.11542	0.13621	1.20	−1.18016	2.828
0.10578	0.15649	1.46	−1.4794	3.127
0.099324	0.17661	1.96	−1.7781	3.426

TABLE 6. (continued).

C_{N_α}	C_{m_α}	M	SM	X_{cp} From Aft End
FCA #11 $\delta = 0°$				
0.09642	0.11011	0.80	−1.14199	2.79
0.10037	0.10796	0.95	−1.07567	2.724
0.10532	0.13284	1.20	−1.2613	2.909
0.10032	0.15679	1.46	−1.56288	3.211
0.094556	0.1939	1.96	−2.0506	3.699
Canards $\delta = 0°$ FCA #3 $\delta = 0°$				
0.10882	0.21824	0.80	−2.0055	3.654
0.11812	0.25393	0.95	−2.1497	3.798
0.11847	0.23176	1.20	−1.9563	3.604
0.10774	0.22121	1.46	−2.0615	3.71
0.09913	0.22947	1.96	−2.3138	3.963
Canards $\delta = 5°$ and FCA #3 $\delta = 0°$				
0.10867	0.2084	0.80	−1.91778	3.566
0.11483	0.23408	0.95	−2.0385	3.686
0.11704	0.23310	1.20	−1.9916	3.64
0.10771	0.23343	1.46	−2.1672	3.815
0.09986	0.2368	1.96	−2.3714	4.019
FCA #1 $\delta = 6°$				
0.10099	0.11307	0.80	−1.1196	2.7676
0.10236	0.08738	0.95	−0.85366	2.5016
0.10794	0.13345	1.20	−1.2363	2.8843
0.10003	0.15802	1.46	−1.5797	3.2277
0.090973	0.17131	1.96	−1.8831	3.5311
0.097038	0.18363	2.74	−1.8924	3.5404
0.94048	0.19661	3.48	−2.0905	3.7385
0.10412	0.20299	4.96	−1.9496	3.5976
FCA #1 $\delta = 15°$				
0.096275	0.108412	0.80	−1.1261	2.7741
0.099769	0.10369	0.95	−1.0393	2.6873
0.10339	0.13809	1.20	−1.3356	2.9836
0.098243	0.16253	1.46	−1.6544	3.3024
0.089579	0.1737	1.96	−1.9391	3.5871
0.096615	0.18538	2.74	−1.9187	3.5667
0.091714	0.19231	3.48	−2.0968	3.7449
0.10186	0.19365	4.96	−1.9012	3.5492
FCA #2 $\delta = 6°$				
0.10216	0.096275	0.80	−0.9424	2.5904
0.10741	0.094269	0.95	−0.87766	2.5257
0.11117	0.1255	1.20	−1.1289	2.7769
0.10386	0.14258	1.46	−1.3728	3.0208
0.093458	0.174088	1.96	−1.8627	3.5107
0.099127	0.18509	2.74	−1.8672	3.5152
0.09352	0.19297	3.48	−2.0634	3.7114
0.097621	0.18666	4.96	−1.9120	3.5600

TABLE 6. (continued).

C_{N_α}	C_{m_α}	M	SM	X_{cp} From Aft End
FCA #2 $\delta = 15°$				
0.10012	0.10672	0.80	−1.0659	2.7139
0.10151	0.12265	0.95	−1.2082	2.8562
0.10601	0.13334	1.20	−1.2578	2.9058
0.09895	0.15012	1.46	−1.5172	3.1652
0.091537	0.17006	1.96	−1.8578	3.5058
0.09782	0.19334	2.74	−1.9765	3.6245
0.09425	0.19569	3.48	−2.0762	3.7242
0.098561	0.18803	4.96	−1.9078	3.556
FCA #3 $\delta = 6°$				
0.098515	0.10682	0.80	−1.08431	2.7323
0.10229	0.10466	0.95	−1.0232	2.6712
0.10534	0.14234	1.20	−1.3512	2.9992
0.09965	0.15214	1.46	−1.5268	3.1747
0.095042	0.18345	1.96	−1.9302	3.578
0.085091	0.18459	2.74	−2.1693	3.8173
0.09121	0.20460	3.48	−2.2432	3.8912
0.10423	0.19119	4.96	−1.8343	3.4823
FCA #3 $\delta = 15°$				
0.10114	0.11424	0.80	−1.1295	2.7775
0.10089	0.12096	0.95	−1.1989	2.8469
0.10398	0.14853	1.20	−1.4285	3.0765
0.098207	0.16284	1.46	−1.6581	3.3061
0.094495	0.18464	1.96	−1.9539	3.6019
0.095123	0.1783	2.74	−1.8744	3.5224
0.09369	0.20649	3.48	−2.204	3.852
0.09953	0.19622	4.96	−1.9714	3.6194
FCA #4 $\delta = 6°$				
0.099154	0.11125	0.80	−1.122	2.77
0.10021	0.11121	0.95	−1.1098	2.7578
0.10492	0.14462	1.20	−1.3784	3.0264
0.09875	0.16031	1.46	−1.6234	3.2714
0.093345	0.1868	1.96	−2.0012	3.649
0.097186	0.1796	2.74	−1.8482	3.496
0.09442	0.20314	3.48	−2.1514	3.799
0.10862	0.20167	4.96	−1.8567	3.505

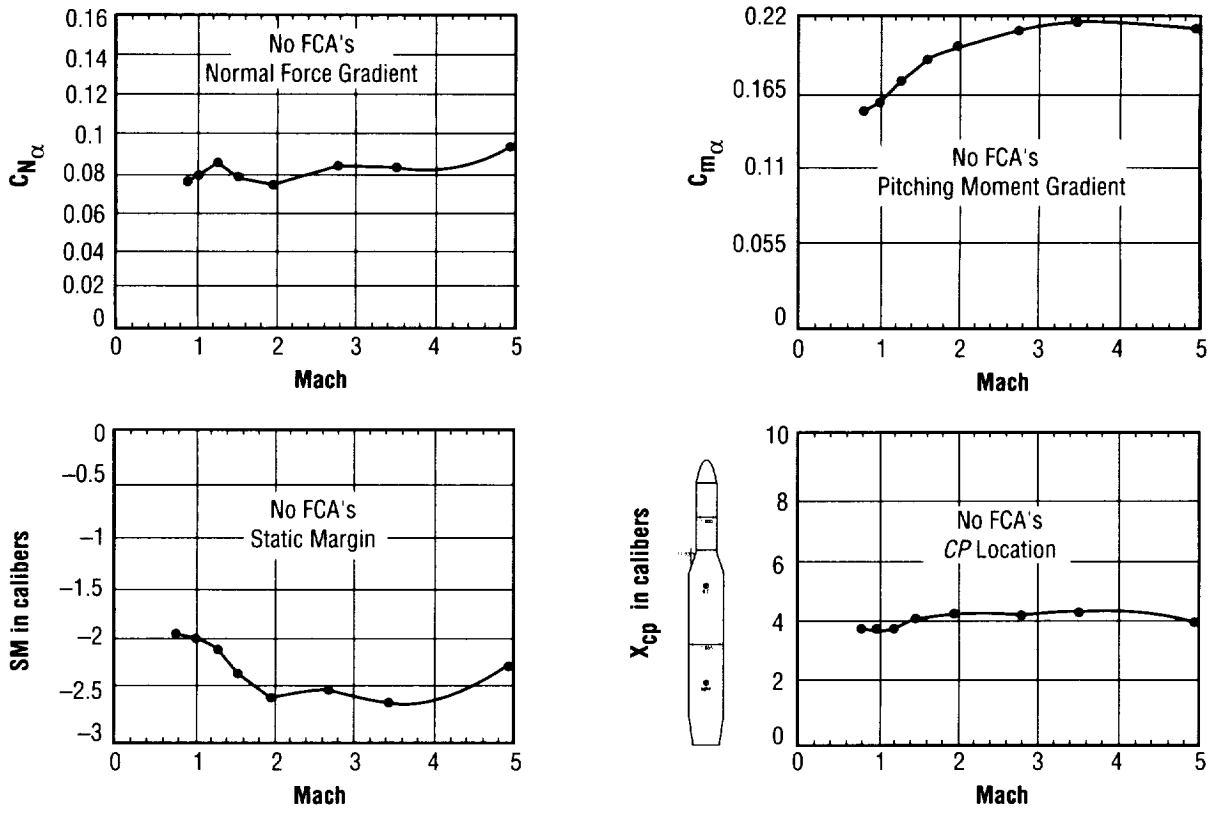

FIGURE 18. Stability results with no FCA's.

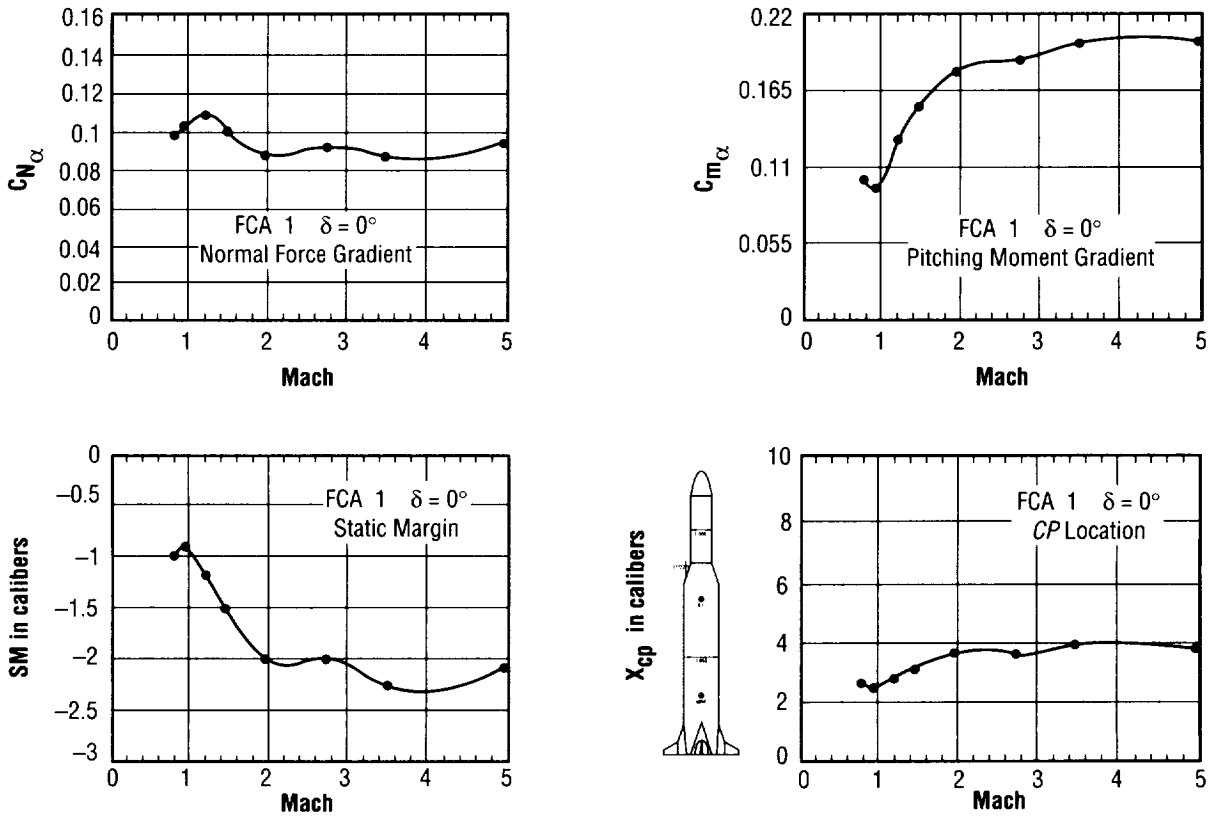

FIGURE 19. Stability results with FCA 1; deflection = 0°.

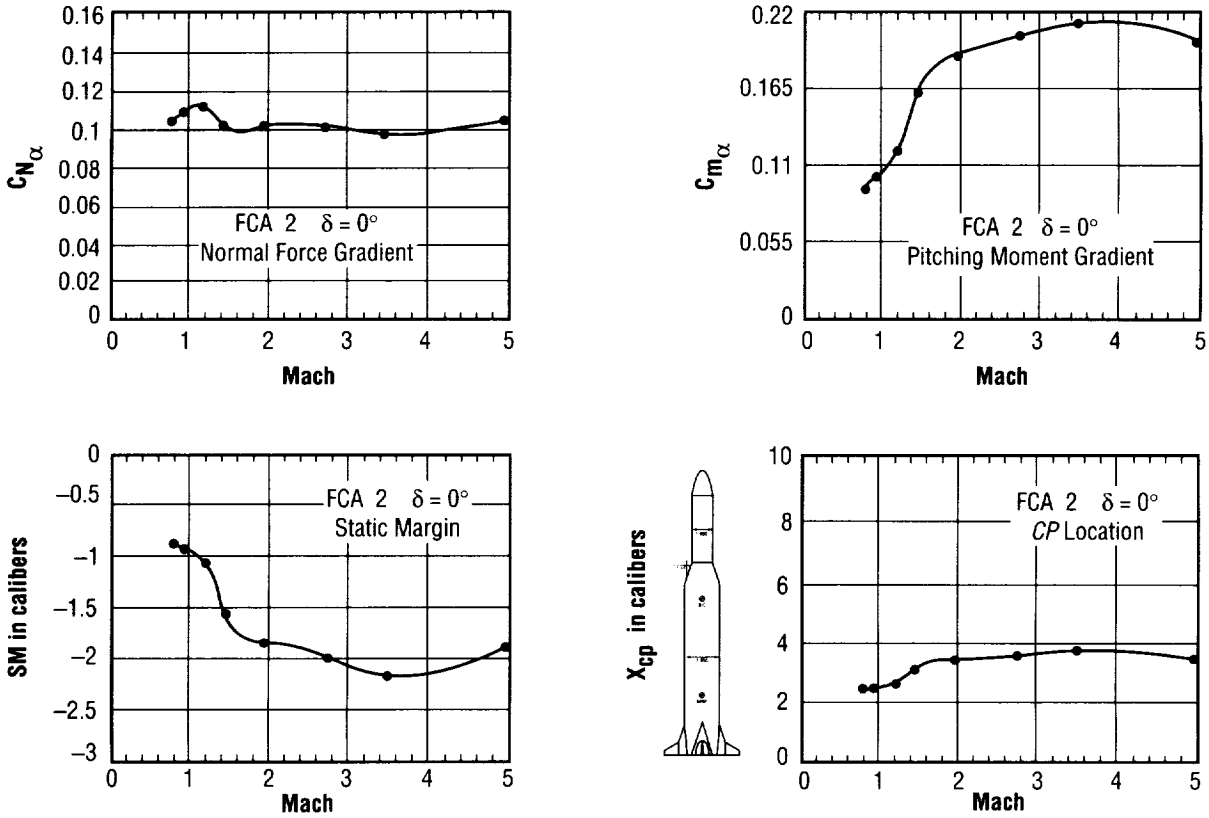

FIGURE 20. Stability results with FCA 2; deflection = 0°.

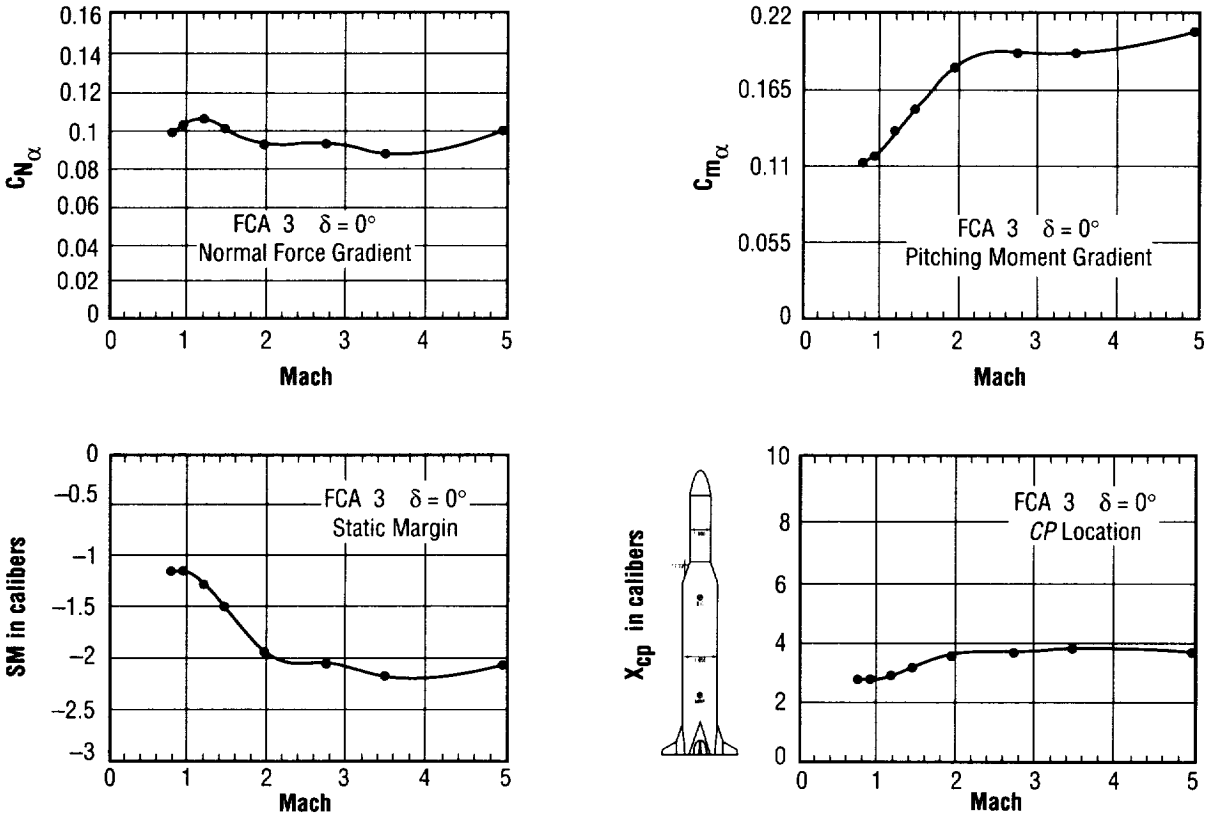

FIGURE 21. Stability results with FCA 3; deflection = 0°.

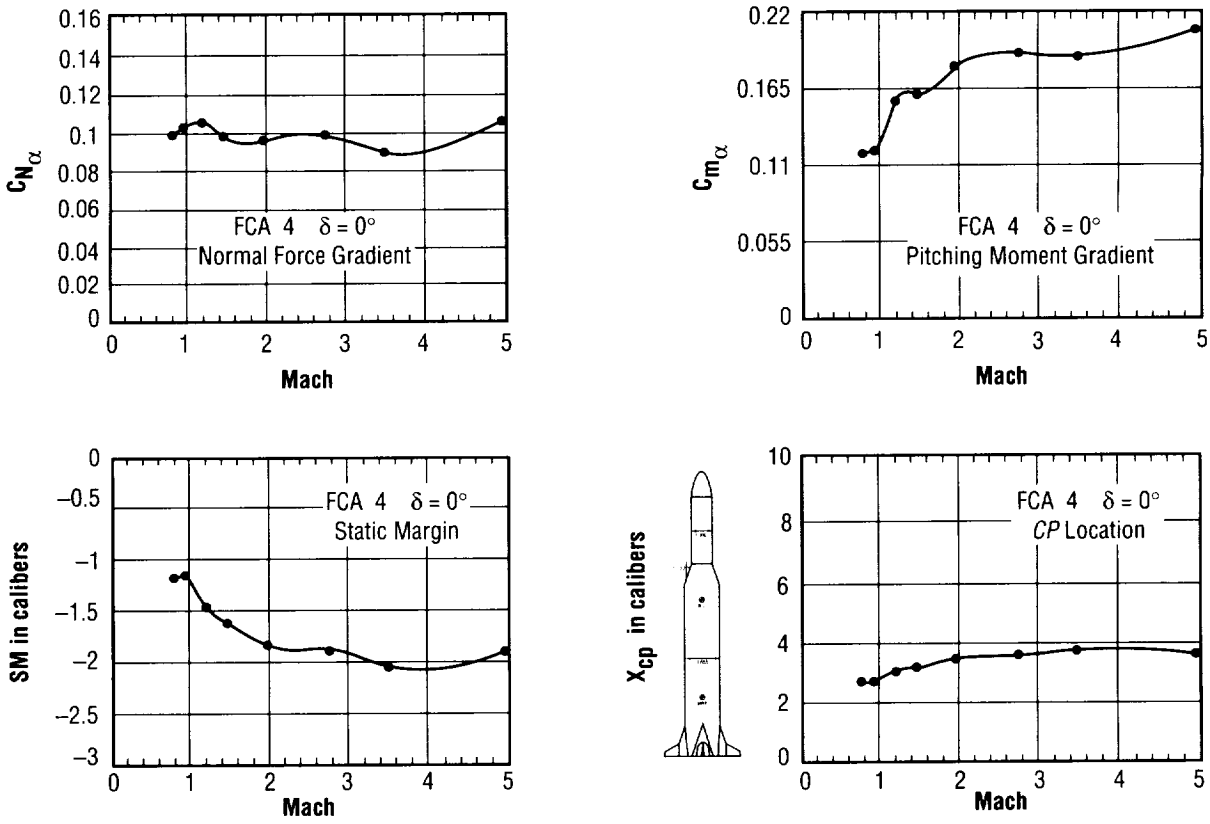

FIGURE 22. Stability results with FCA 4; deflection = 0°.

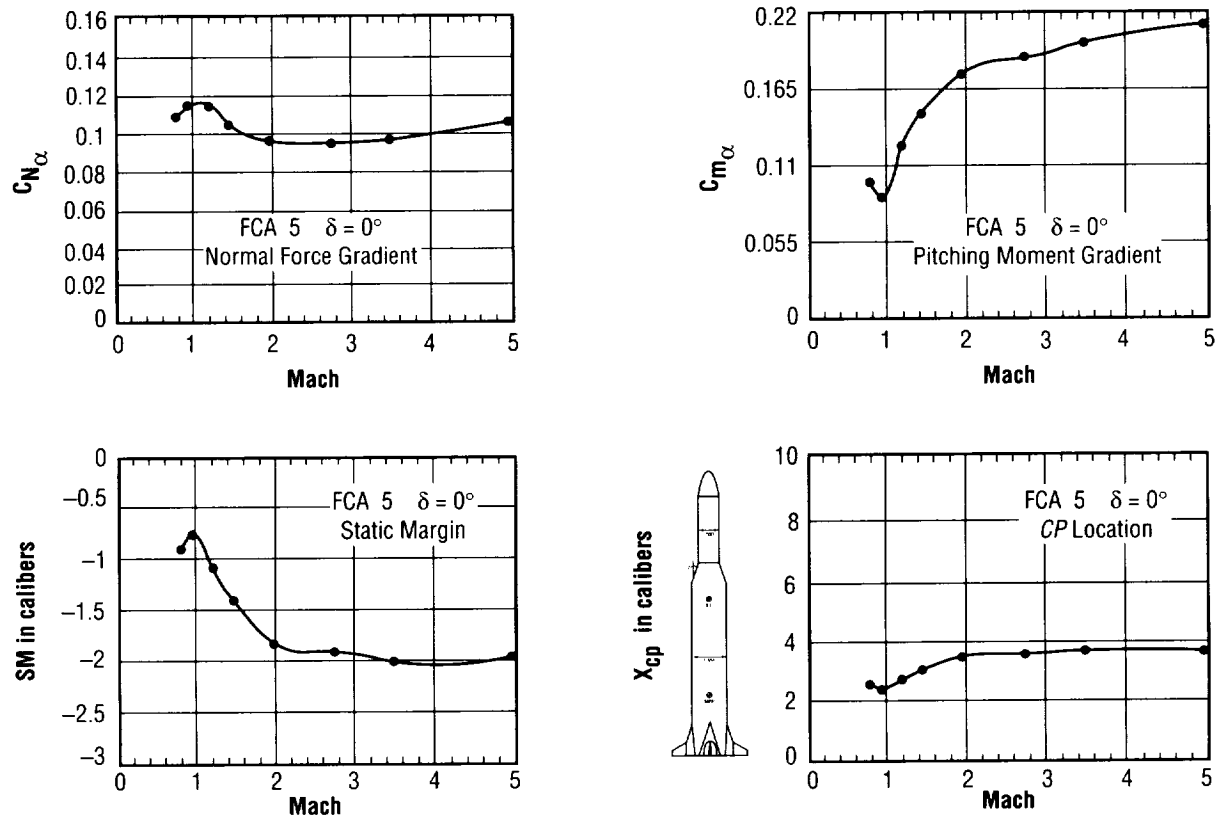

FIGURE 23. Stability results with FCA 5; deflection = 0°.

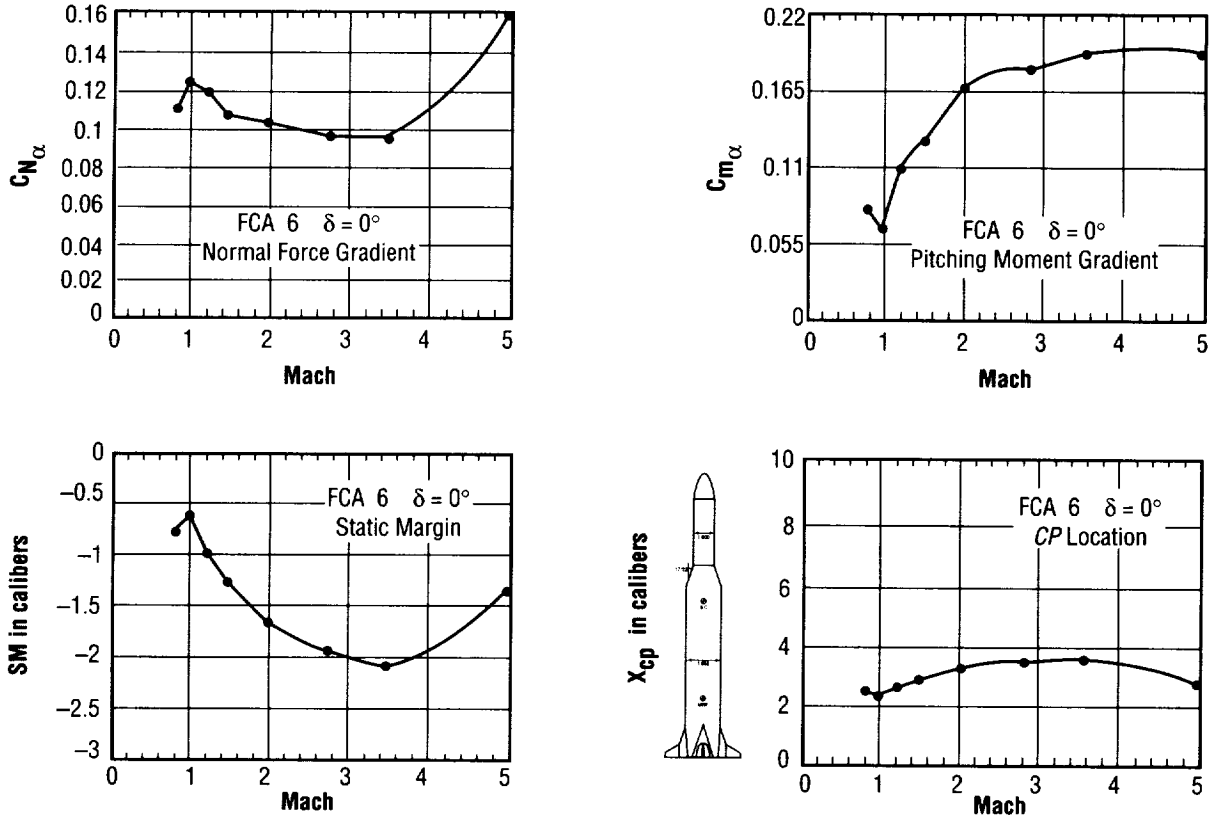

FIGURE 24. Stability results with FCA 6; deflection = 0°.

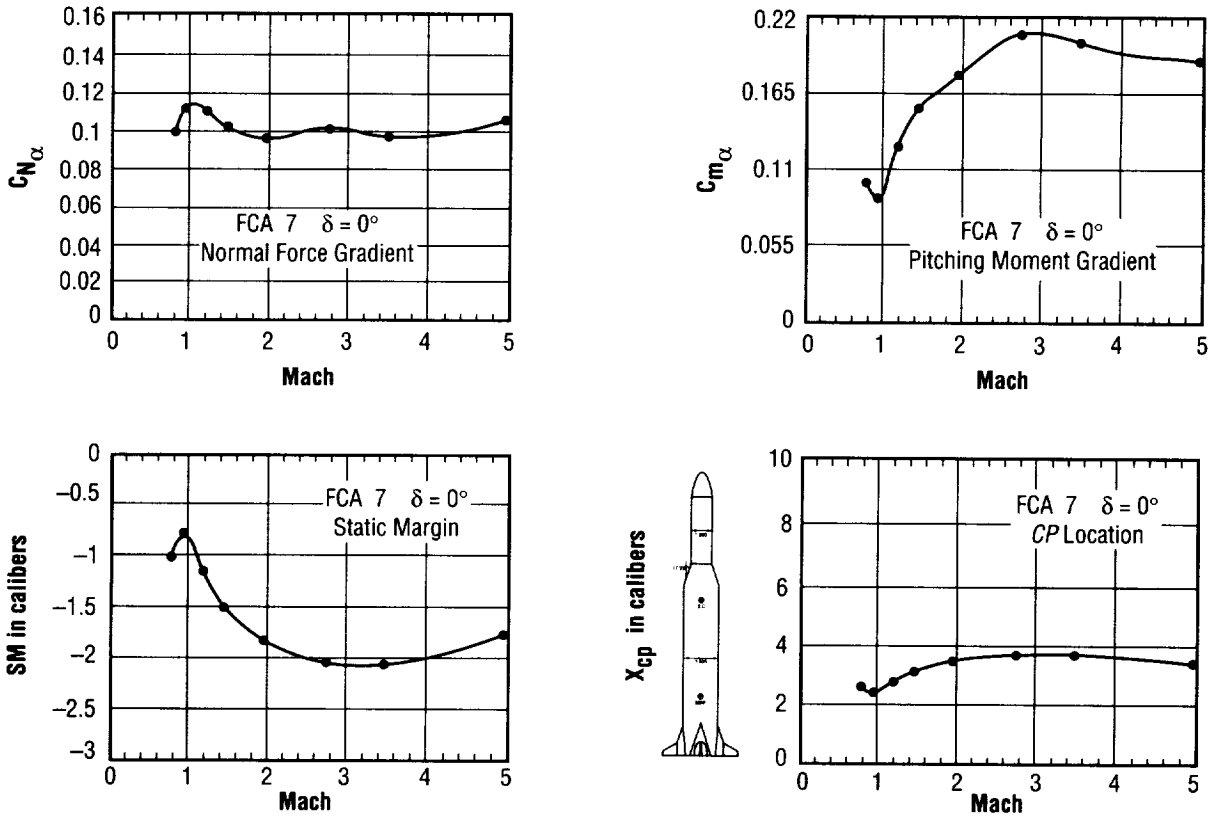

FIGURE 25. Stability results with FCA 7; deflection = 0°.

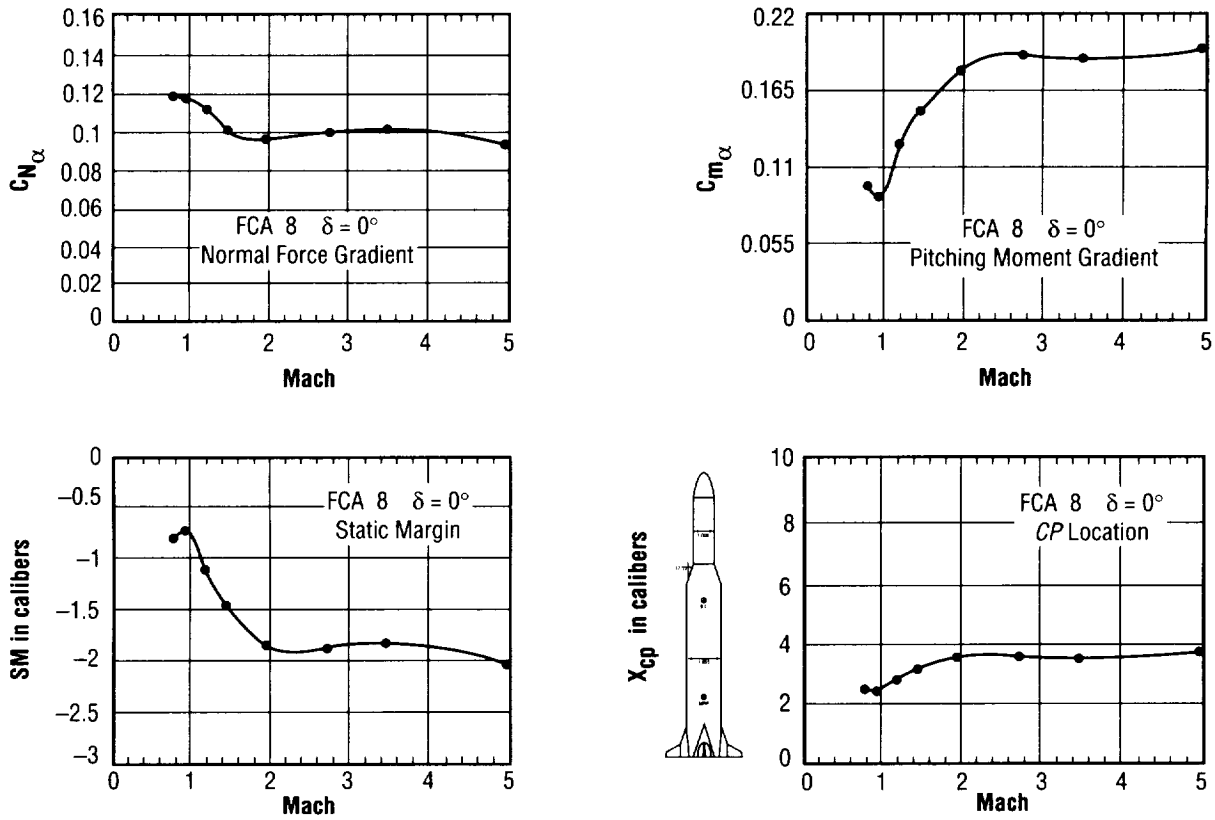

FIGURE 26. Stability results with FCA 8; deflection = 0°.

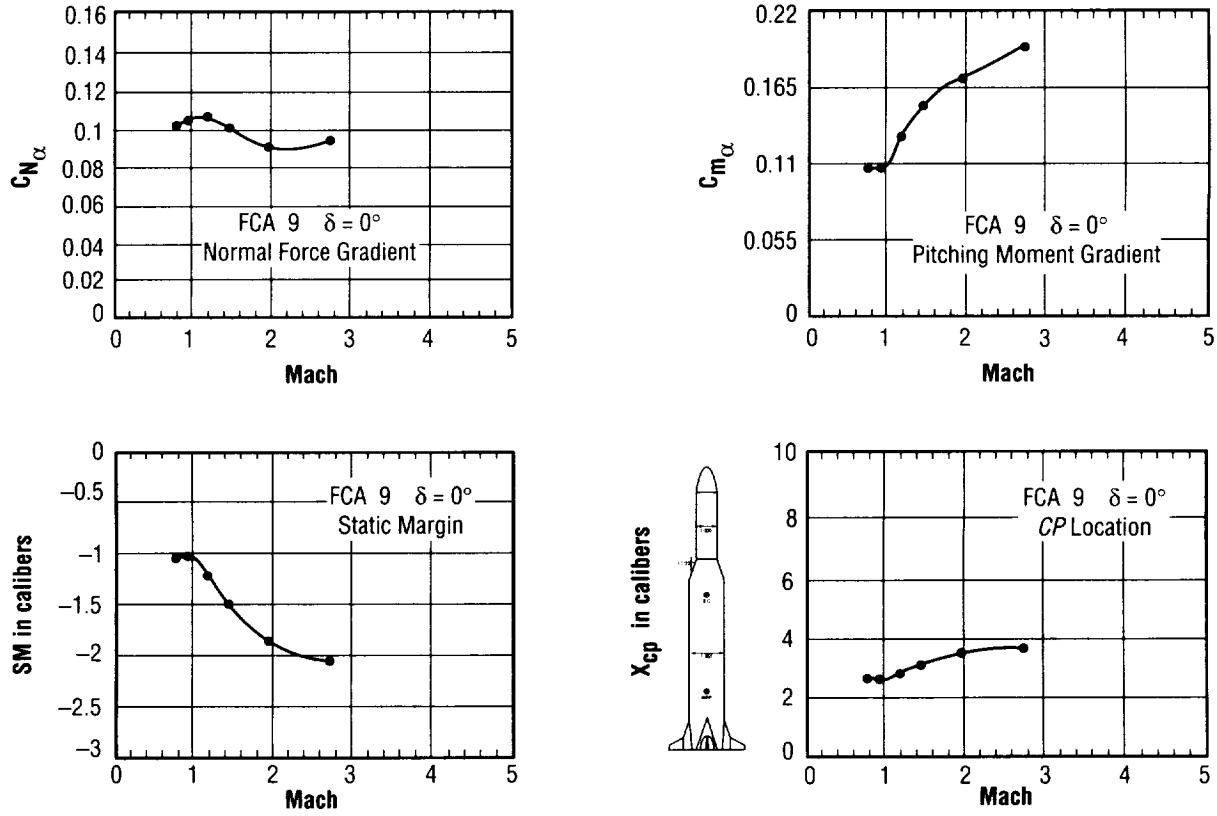

FIGURE 27. Stability results with FCA 9; deflection = 0°.

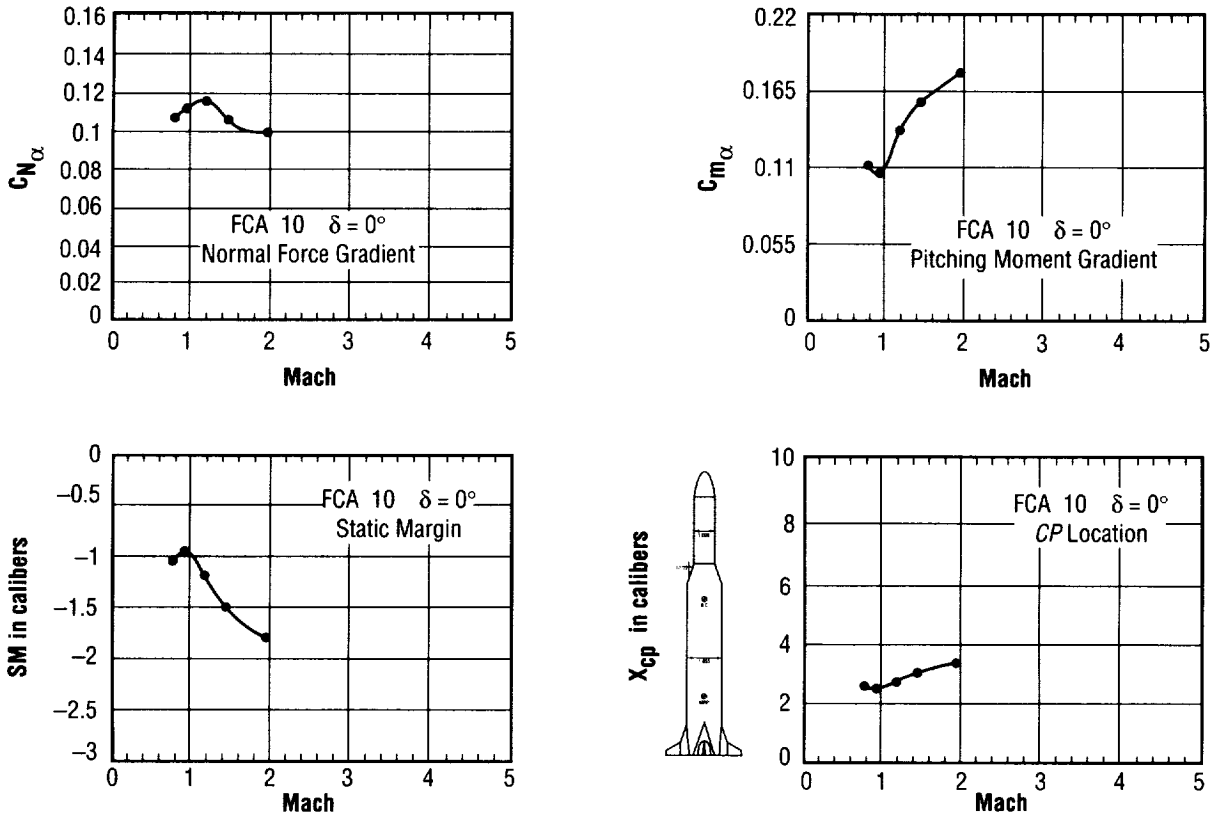

FIGURE 28. Stability results with FCA 10; deflection = 0°.

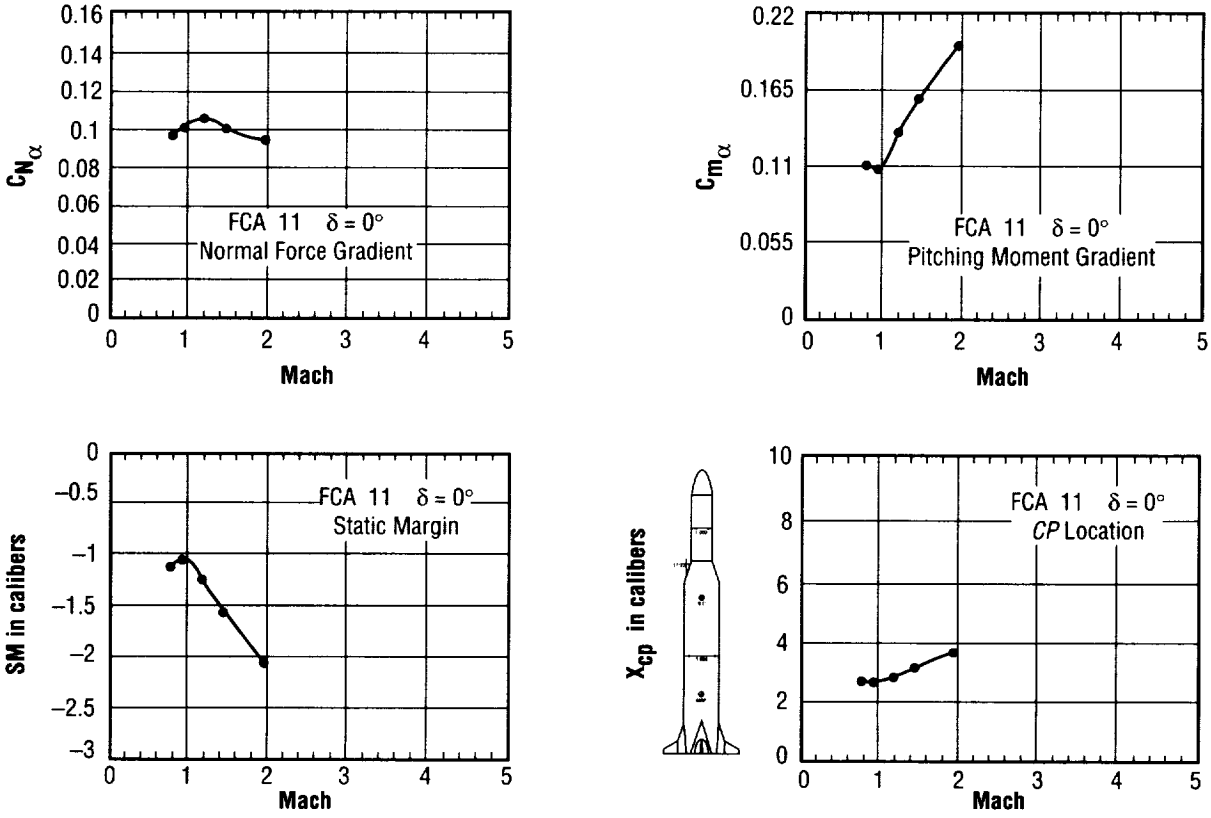

FIGURE 29. Stability results with FCA 11; deflection = 0°.

TABLE 7. FCA flight stability ratings based on SM.

FCA No. ($\delta = 0°$)	SM	Planform Design
No FCA's	−2.0	
6	−0.56	Triangular, 30° LE Λ, Blunt TE, Wedge
8	−0.75	Triangular, 30° LE Λ, Lenticular
5	−0.77	Triangular, 30° LE Λ, Diamond
7	−0.80	Triangular, 30° LE Λ, Diamond, Clipped Tip
2	−0.89	Triangular, 45° LE Λ, Blunt TE, Wedge
1	−0.92	Triangular, 45° LE Λ, Diamond
10	−0.96	Forward Swept, −45° LE Λ, Diamond
9	−1.02	Aft Swept, 45° LE Λ, 30° TE Λ, Diamond
11	−1.08	Trapezoidal, 45° LE Λ, −30° TE Λ, Diamond
3	−1.14	Triangular, 45° LE Λ, Diamond, Clipped Tip
4	−1.18	Triangular, 45° LE Λ, Lenticular

B. Control Analysis

The control requirement is to have the control ratio (CR) ≥ 1.5 where the CR is the ratio of the control torque (CT) to the aerodynamic torque (AT). With no FCA's the total control torque is that provided by the thrust vector control (TVC) of the gimbaled engines. With the use of aft FCA's the total CT becomes the sum of that provided by both the TVC and the FCA's. From equation (5),

$$\mathrm{CR} = \frac{T \sin \delta_E \; (E) \; \ell_E}{C_{N_\alpha} \; \alpha \; Q \; S \; \ell_{cp}} \geq 1.5 \tag{16}$$

Since

$$C_N \; Q \; S \; \ell_{cp} = C_m \; Q \; S \; d \tag{17}$$

it follows that,

$$\mathrm{CR} = \frac{T \sin \delta_E \; (E) \; \ell_E}{C_N \; Q \; S \; \ell_{cp}} = \frac{T \sin \delta_E \; (E) \; \ell_E}{C_m \; Q \; S \; d} \geq 1.5 \tag{18}$$

With deflection of the FCA's the pitching moment coefficient involves more terms. Using a relationship developed in the classic work of Etkin[13]

$$C_m = C_{m_o} + C_{m_\alpha} \; \alpha + C_{m_{\delta_F}} \; \delta_F \tag{19}$$

where C_{m_o} = pitching moment coefficient at $\alpha = 0°$; when the FCA deflection is utilized to augment the TVC control, the control stability derivative is,

$$C_{m_{\delta_F}} = \frac{\partial C_m}{\partial \delta_F} \equiv \text{FCA Control Power} \tag{20}$$

The more negative the value of $C_{m_{\delta_F}}$, the more effective the FCA control power of the experimental LV. For no deflection of the controls, equation (19) reduces $C_m = C_{m_\alpha}\ \alpha$. Thus, equation (18) becomes,

$$\text{CR} = \frac{T \sin \delta_E\ (E)\ \ell_E}{\left(C_{m_o} + C_{m_\alpha}\ \alpha + C_{m_{\delta_F}}\ \delta_F\right) Q\ S\ d} \geq 1.5 \tag{21}$$

For the experimental LV, the CR is now calculated using equation (16), first with no FCA's, then with FCA's but no deflection, and finally using equation (21) with FCA's and FCA deflection.

From table 1, $S = 597.56\ \text{ft}^2$, $d = 27.58$ ft, and $\delta_E = \alpha = 4°$. Before the FCA's were designed, the preliminary mass properties and corresponding trajectory data for the experimental aft-cg LV were used. Subsequently, the NASA MSFC Systems Engineering Division has updated and refined the mass properties for the experimental aft-cg LV. The updated far aft-cg mass properties and corresponding trajectory data, which challenge the FCA's to a greater degree, are used in this analysis. The trajectory data shows that at max Q conditions, the six engines are only producing 491,806.5 lb of thrust each; max Q = 722.56 psf at $M = 1.31$. From table 6 above, for no FCA's, the interpolated values corresponding to $M = 1.31$ are $C_{N_\alpha} = 0.081208$ and $C_{m_\alpha} = 0.176911$; $\Rightarrow \ell_{cp} = 60.08$ ft. Using these values and $\ell_E = 45.82$ ft in equation (16) with no FCA's,

$$\text{CR} = \frac{9{,}431{,}594\ \text{ft} - \text{lb}}{8{,}426{,}557\ \text{ft} - \text{lb}} = 1.12 \tag{22}$$

which shows that the FCA's are presented with a greater challenge to augment the control torque than was the case using preliminary data, where the CR was calculated to be 1.30.

Now using FCA 6, but no deflection, table 6 above shows that for FCA 6 with $\delta_F = 0°$ at $M = 1.31$ (interpolated), $C_{N_\alpha} = 0.11629$ and $C_{m_\alpha} = 0.12085$; $\Rightarrow \ell_{cp} = 28.66$ ft. Substituting these values into equation (16) yields,

$$\text{CR} = \frac{9{,}431{,}594\ \text{ft} - \text{lb}}{5{,}756{,}255\ \text{ft} - \text{lb}} = 1.64 \tag{23}$$

This shows that the controllability is more than adequate at max Q with only the presence of the FCA's using no deflection at all. It can be seen that the improvement in the CR by the mere presence of the FCA's with no deflection at all is 46 percent.

Now FCA 6 is used with deflection. Figures 30–31 show the control power $\left(C_{m_{\delta_F}}\right)$ for selected FCA's through the range of Mach numbers. It can be seen that the control power is greatest for most aft FCA's at max Q. Next, C_m values were plotted against α for the cases of FCA deflection. The value of C_m when $\alpha = 0°$ were tabulated, shifting data curves by a small amount when necessary, i.e., when it was known that a curve should pass through the origin. From the reduced and shift corrected data (using very conservative values of C_{m_o}), a sample C_{m_o} tabulation for the case of a deflected FCA is,

FCA 6	$\delta_F°$	M = 1.20 C_{m_o}	M = 1.46 C_{m_o}	M = 1.3 C_{m_o}
	0	0	0	0
	3	−0.1073	−0.047	−0.8411
	6	−0.2342	−0.1491	−0.2015
	9	−0.3284	−0.2331	−0.2918
	12	−0.3800	−0.3135	−0.3544
	15	−0.4654	−0.3551	−0.423

C_m was plotted against δ_F for fixed α and the slopes calculated. Table 8 shows selected calculated longitudinal control derivatives for $\alpha = 4°$ through the Mach range.

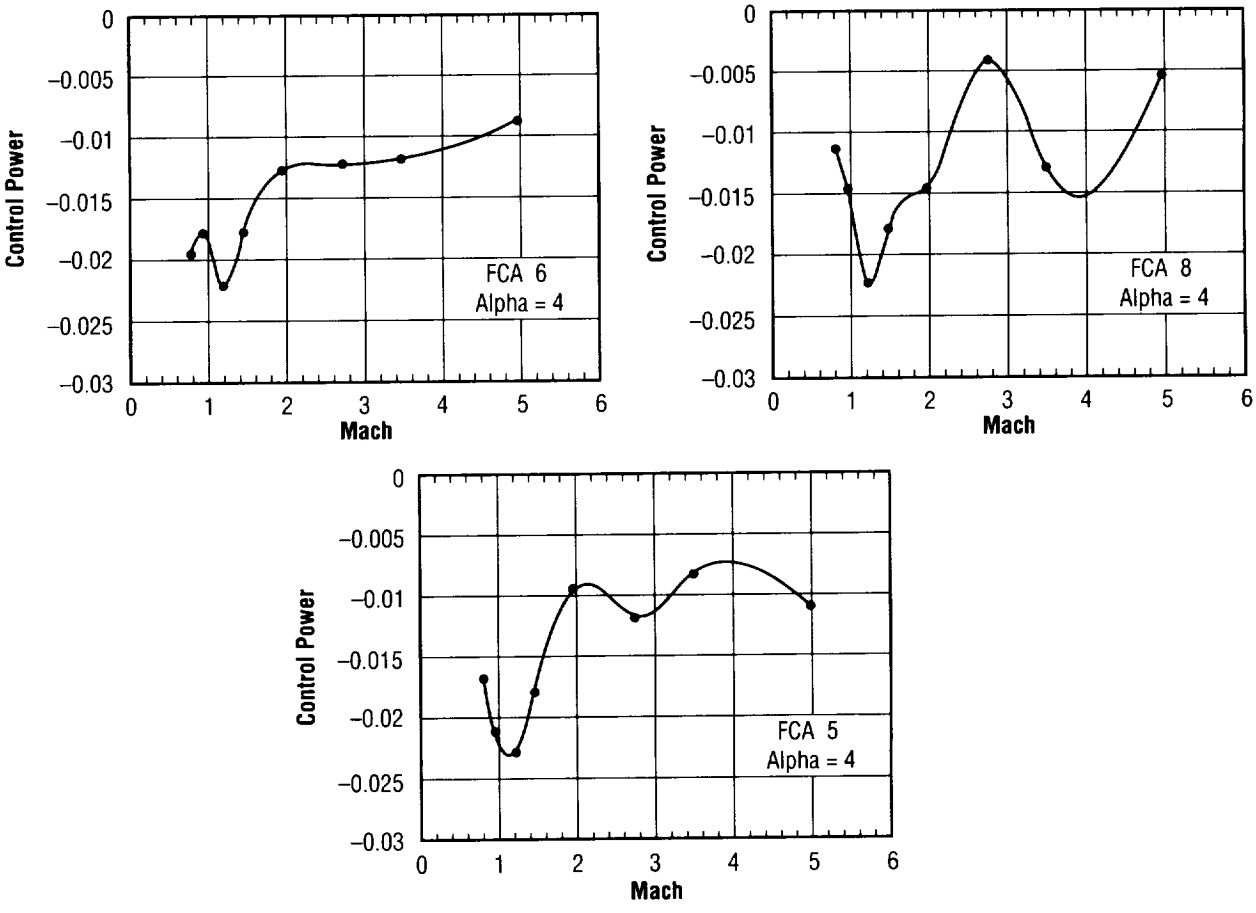

FIGURE 30. Control power versus Mach number for FCA 5, 6, and 8.

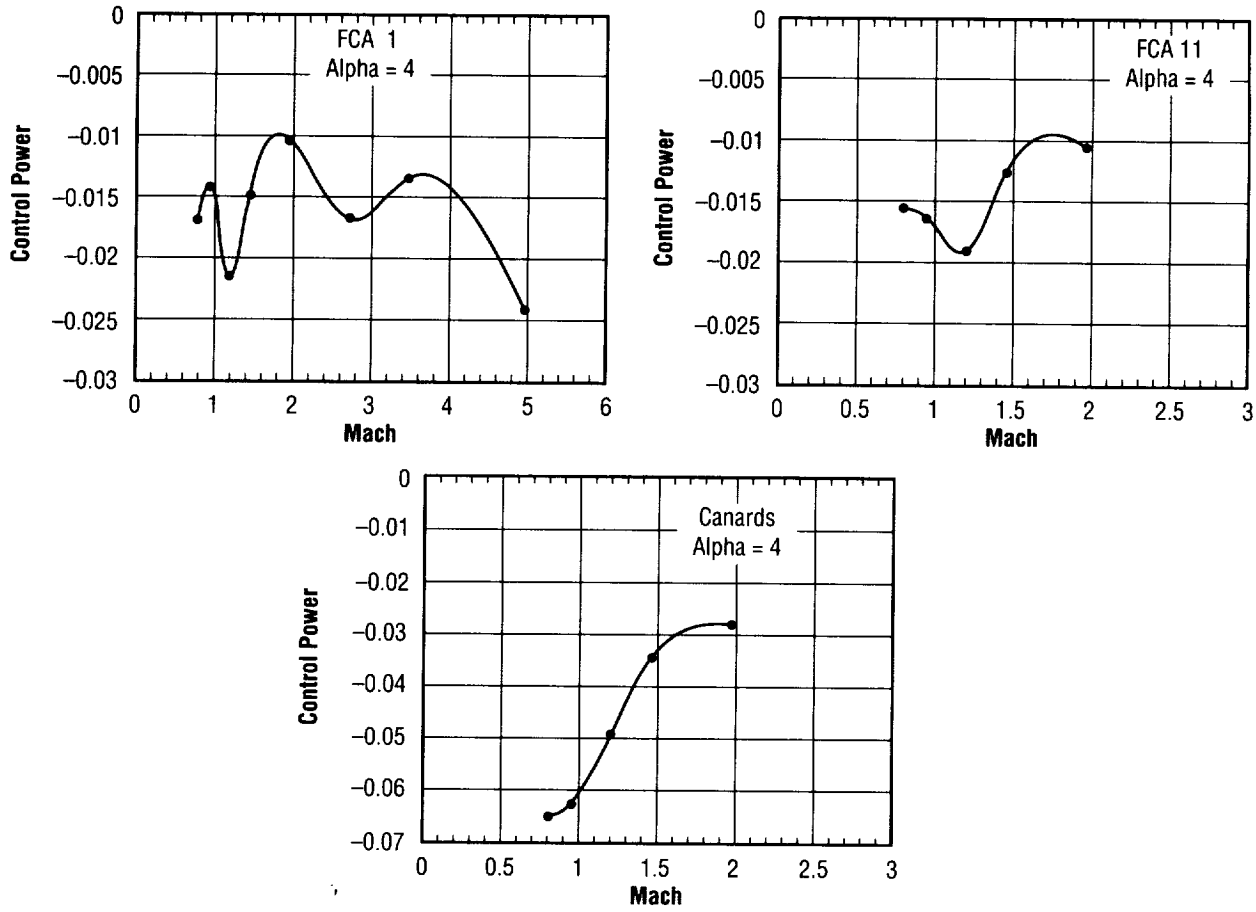

FIGURE 31. Control power versus Mach number for FCA 1, 11, and canard.

TABLE 8. Calculated longitudinal control derivatives for $\alpha = 4°$.

M	FCA 1 C_{m_δ}	FCA 5 C_{m_δ}	FCA 6 C_{m_δ}	FCA 8 C_{m_δ}	FCA 11 C_{m_δ}	Canards C_{m_δ}
0.80	-0.01712	-0.01699	-0.0197	-0.01136	-0.01579	-0.06477
0.95	-0.01442	-0.0213	-0.018	-0.01457	-0.01665	-0.0626
1.20	-0.02167	-0.02288	-0.02218	-0.02222	-0.0193	-0.04922
1.46	-0.01503	-0.01815	-0.01795	-0.01782	-0.01274	-0.03446
1.96	-0.01053	-0.009573	-0.0129	-0.01448	-0.01071	-0.02804
2.74	-0.01696	-0.01193	-0.01243	-0.003922		
3.48	-0.01365	-0.0084	-0.012	-0.01283		
4.96	-0.0243	-0.01098	-0.008933	-0.0055		

For FCA 6 at $M = 1.31$, $C_{m_\alpha} = 0.12085$ (at fixed δ_F) from above, and from table 6, $C_{m_{\delta_F}} = -0.020553$ (at fixed α). Substituting these values into equation (21), CR is determined as a function of FCA deflection

angle. Table 9 shows the calculated control ratio values for various FCA deflection angles, and figure 32 is the control analysis summary plot which shows the control ratio for no FCA's, the required amount, and that available through the use of the deflected FCA's.

TABLE 9. Calculated control ratio values for FCA deflection angles.

$\delta_F°$	Control Ratio
No FCA's	1.12
Min. Requirement	1.50
0	1.64
3	2.35
6	4.99
9	120.00

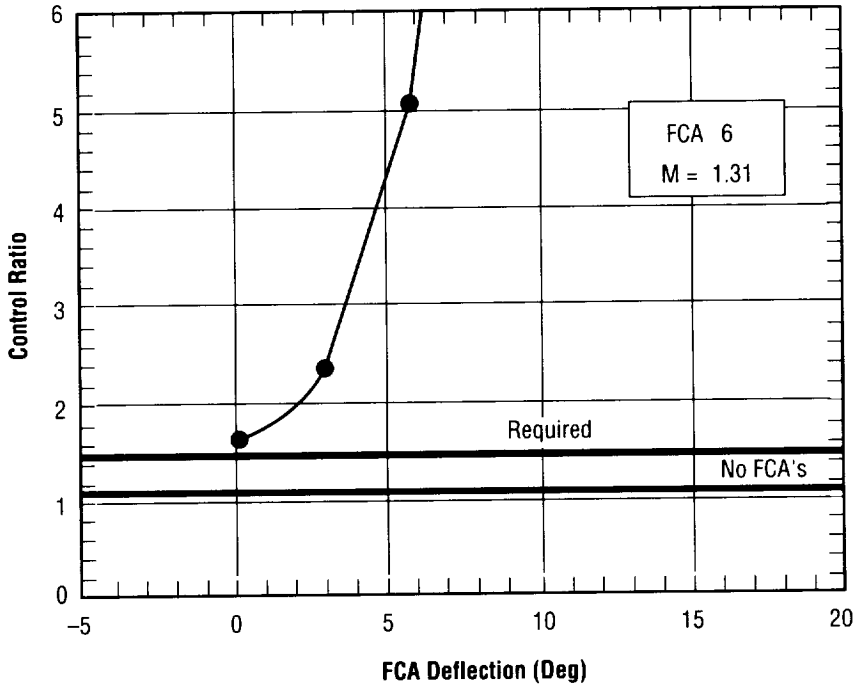

FIGURE 32. Control analysis summary plot.

When the aerodynamic moments on the vehicle are zero, the vehicle is said to be trimmed. From equation (36)

$$C_m = C_{m_o} + C_{m_\alpha}\ \alpha + C_{m_{\delta_F}}\ \delta_F = 0 \text{ for trim} \Rightarrow \delta_{F_{\text{Trim}}} = 9.1° \ . \qquad (24)$$

Thus, (for FCA 6), when the FCA's are deflected 9.1°, there is no resultant aerodynamic moment on the LV for $\alpha = 4°$. For deflections above 9.1°, the FCA's would be available to provide excess control along with the TVC.

Even greater results are achievable by using the FCA's and engine shrouds at 45°. It was found that the Saturn V aerodynamic surfaces and engine shrouds became more efficient when the LV was rolled 45° in the wind tunnel tests. With the FCA surfaces aligned with the body axes, i.e., two surfaces in the horizontal position and two in the vertical position, only two are working in the pitch plane. This orientation is referred to in the literature as the (+) configuration. When the FCA surfaces are rolled in orientation with respect to the body axes, all four would be working in the pitch plane. This orientation is referred to as the (X) configuration[14] (see fig. 33). For example,

$$0° \text{ (+)}: \quad N_F = 2\ C_{N_F}\ Q\ S_F$$

$$45° \text{ (X)}: \quad N = 4\ (\sin 45°)\ C_{N_F}\ Q\ S_F = 2.83\ C_{N_F}\ Q\ S_F \tag{25}$$

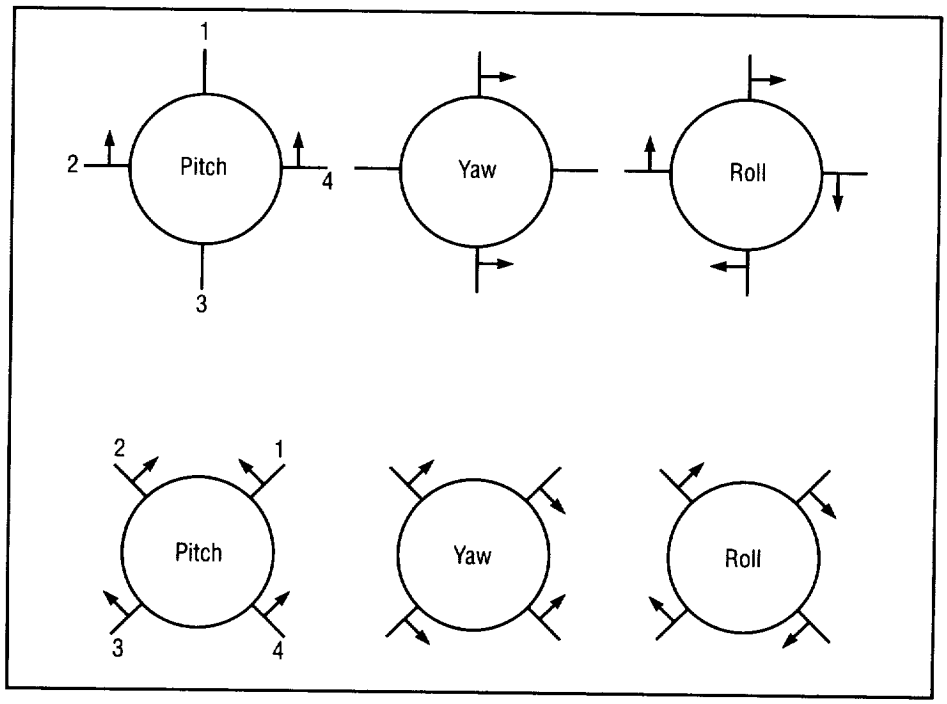

FIGURE 33. Definitions of positive pitch, yaw, and roll control (arrow shows direction of forces and leading edge of panel, looking upstream).

For canard control, from table 6 above, for $\alpha = 4°$ and $M = 1.31$ (interpolation), $C_{m_{\delta_C}} = -0.04354$ and from the sample tabulation of reduced and shift corrected data for C_{m_o} for the canards,

$\delta c°$	M = 1.20 C_{m_o}	M = 1.46 C_{m_o}	M = 1.3 C_{m_o}
0	0	0	0
5	−0.2760	−0.2197	−0.2543
10	−0.575	−0.4035	−0.5090
15	−0.8103	−0.6019	−0.7301
20	−0.9391	−0.6528	−0.829
25	−0.8394	−0.7911	−0.8208
30	−1.0719	−0.8328	−0.9799

Using the trim equation (24) for the canards, it can be seen that the canards are capable of trimming out the aerodynamic moment with only 5° of deflection.

In summary, the control analysis shows that the mere presence of the FCA's with no deflection increases the control ratio by 46 percent. When FCA deflection is utilized, the control ratio increases by 110 percent for 3° FCA deflection, to 346 percent for 6° FCA deflection, and at 9.1° FCA deflection, the aerodynamic moment is completely trimmed for the $\alpha = 4°$ case considered. The canards are able to trim the vehicle at 5° deflection.

C. Dynamic Stability Characteristics

A LV in its ascent trajectory is exposed to unsteady flow fields and asymmetric vortex shedding that may affect the vehicle's motion significantly. Unsteady flow fields affect the dynamic stability derivatives. Whereas the static stability derivatives are a function of aerodynamic angle, control surface deflection, and Mach number, the dynamic stability derivatives are a function of aerodynamic angle rates of change, control surface deflection rates, body rates, and Mach number, e.g.,

$$C_{m_{\dot{\alpha}}} \quad , \quad C_{n_{\dot{\beta}}} \quad , \quad C_{m_{\dot{\delta}}} \quad , \quad C_{m_q} \quad , \quad C_{\ell_{\dot{\phi}}}$$

where

$$C_{m_{\dot{\alpha}}} \equiv \frac{\partial C_m}{\partial \dot{\alpha}} \quad , \text{ etc.}$$

In certain flight vehicles, significant aerodynamic coupling between longitudinal and lateral-directional degrees of motion can occur. Figure 34 shows cross, cross-coupling, and damping dynamic stability derivatives.[15] Damping derivatives are defined such that each vector component of the moment, $\overline{M} = (\ell, m, n)$, is differentiated with respect to the same corresponding vector component of angular velocity, $\overline{\omega} = (p, q, r)$, i.e.,

$$C_{\ell_p} \, , \; C_{m_q} \, , \; C_{n_r} \qquad \text{where} \qquad C_{\ell_p} \equiv \frac{\partial C_\ell}{\partial p} \quad , \qquad \text{etc.}$$

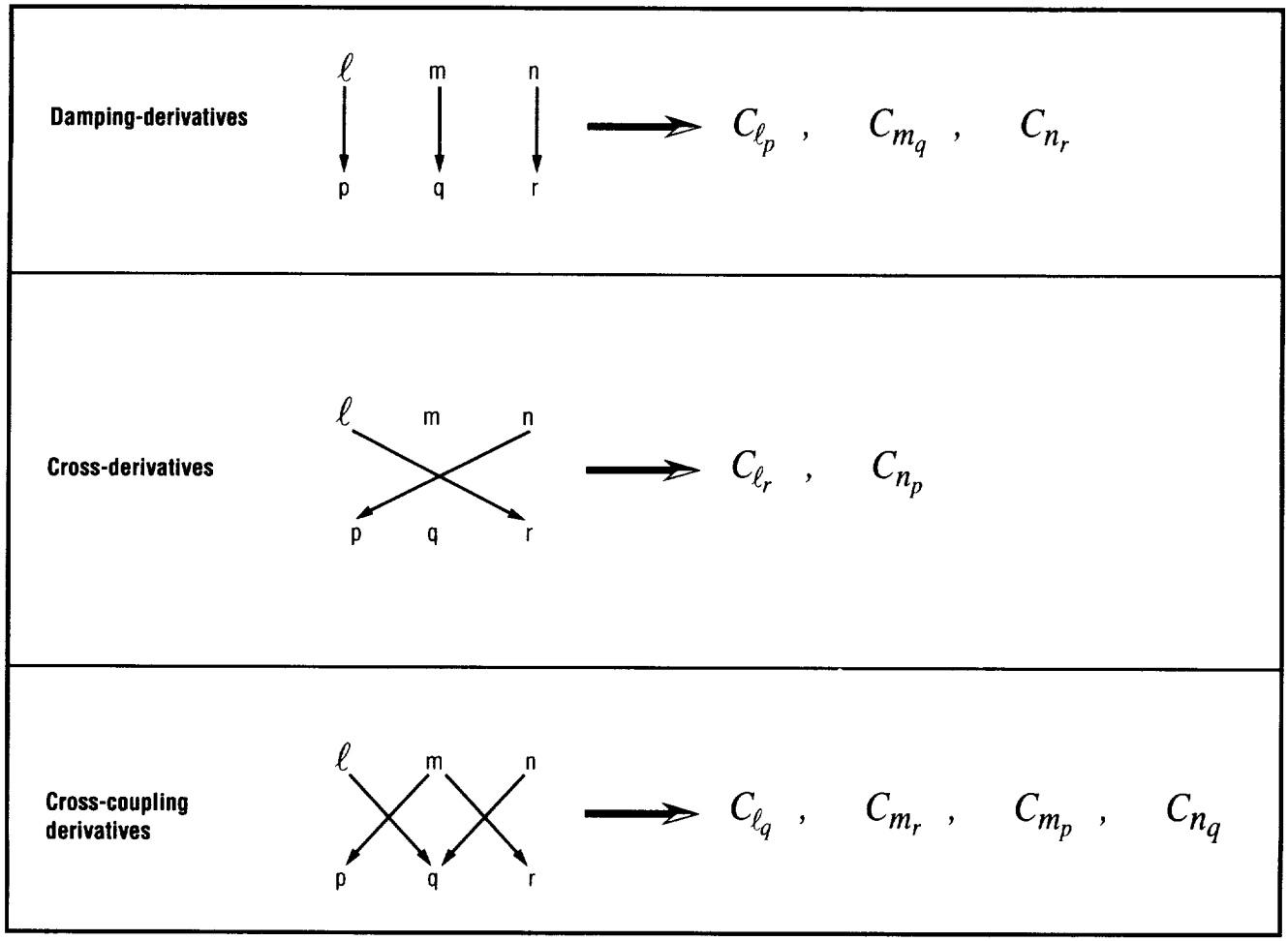

FIGURE 34. The classification of dynamic stability derivatives.

Table 10 shows some types of moment dynamic stability derivatives.[16]

TABLE 10. Moment dynamic stability derivatives.

Pure Rotation		
$C_{\ell_p} = \frac{\partial C_\ell}{\partial \frac{pb}{2V}}$	$C_{m_p} = \frac{\partial C_m}{\partial \frac{pb}{2V}}$	$C_{n_p} = \frac{\partial C_n}{\partial \frac{pb}{2V}}$
$C_{\ell_q} = \frac{\partial C_\ell}{\partial \frac{q\bar{c}}{2V}}$	$C_{m_q} = \frac{\partial C_m}{\partial \frac{q\bar{c}}{2V}}$	$C_{n_q} = \frac{\partial C_n}{\partial \frac{q\bar{c}}{2V}}$
$C_{\ell_r} = \frac{\partial C_\ell}{\partial \frac{rb}{2V}}$	$C_{m_r} = \frac{\partial C_m}{\partial \frac{rb}{2V}}$	$C_{n_r} = \frac{\partial C_n}{\partial \frac{rb}{2V}}$

TABLE 10. (continued).

Translational Acceleration		
$C_{\ell_{\dot{\alpha}}} = \frac{\partial C_\ell}{\partial \frac{\dot{\alpha}\bar{c}}{2V}}$	$C_{m_{\dot{\alpha}}} = \frac{\partial C_m}{\partial \frac{\dot{\alpha}\bar{c}}{2V}}$	$C_{n_{\dot{\alpha}}} = \frac{\partial C_n}{\partial \frac{\dot{\alpha}\bar{c}}{2V}}$
$C_{\ell_{\dot{\beta}}} = \frac{\partial C_\ell}{\partial \frac{\dot{\beta}b}{2V}}$	$C_{m_{\dot{\beta}}} = \frac{\partial C_m}{\partial \frac{\dot{\beta}b}{2V}}$	$C_{n_{\dot{\beta}}} = \frac{\partial C_n}{\partial \frac{\dot{\beta}b}{2V}}$

Damping Derivatives	Oscillation Around Fixed Axis: Cross Derivatives	Cross-Coupling Derivatives
$C_{\ell_p} + C_{\ell_{\dot{\beta}}} \sin\alpha$	$C_{\ell_r} + C_{\ell_{\dot{\beta}}} \cos\alpha$	$C_{\ell_q} + C_{\ell_{\dot{\beta}}}$
$C_{m_q} + C_{m_{\dot{\alpha}}}$	$C_{n_p} + C_{n_{\dot{\beta}}} \sin\alpha$	$C_{m_r} + C_{m_{\dot{\beta}}} \cos\alpha$
$C_{n_r} + C_{n_{\dot{\beta}}} \cos\alpha$		$C_{m_p} + C_{m_{\dot{\beta}}} \sin\alpha$
		$C_{n_q} + C_{n_{\dot{\alpha}}}$

The longitudinal dynamic stability derivatives, i.e., the pitch damping derivatives $\left(C_{m_q} + C_{m_{\dot{\alpha}}}\right)$ and the corresponding C_{m_α} for a Mach range of 0.8 to 1.96 and FCA deflections from 0° to 15°, were obtained and are discussed here. Oscillation around a fixed axis results in a sum of a purely rotary derivative and a translational acceleration derivative. In the longitudinal case, these are C_{m_q} and $C_{m_{\dot{\alpha}}}$, respectively, which are now explained. For a free-flying vehicle, the variations in angle of pitch, q, and in α can occur independently of each other, and each gives rise to a different longitudinal distribution of the normal velocity. The distribution due to the angle-of-pitch variation, i.e., due to the pitching velocity q, varies along the LV body and intersects zero at the axis of rotation, while the distribution due to the α variation, $\dot{\alpha}$, is constant along the fuselage. In the case of an oscillation about a fixed axis, both variations occur simultaneously, and even if the two variables q and $\dot{\alpha}$ are numerically equal, their effects are different and have to be superimposed. Figure 35 shows these different motions. The contribution due to $\dot{\alpha}$ is equivalent to one due to a vertical acceleration, since $\dot{\alpha} = \frac{\ddot{Z}}{V}$.

For more insight on the two different angular rates, $\dot{\alpha}$ and q, which produce aerodynamic moments proportional to the damping terms, one or both of the angular velocities must be nonzero. One simple planar motion that produces $q \neq 0$ and $\dot{\alpha} = 0$ is the circular looping motion shown in figure 35. In this case, the in-plane moment, C_m, contains contributions from both the pitching moment slope C_{m_α} and C_{m_q}. The contribution from C_{m_α} can be eliminated if the vehicle longitudinal axis is tangent to the radius of curvature of the loop. In this case, $\alpha = 0$, and C_{m_q} is directly proportional to the net aerodynamic moment.

Other more complicated helical motions can be used for visualization. Two such motions require the cg of the vehicle to traverse a helical flight path. The first motion requires the vehicle's longitudinal axis to be oriented in the same direction as the center of rotation of the helix but displaced by a constant distance. A 2–D projection of this motion on the vertical plane is what is depicted in figure 35 in the $\dot{\alpha} \neq 0$, $q = 0$ case, where α and $\dot{\alpha}$ vary continuously, and produce moment components proportional to C_{m_α} and $C_{m_{\dot{\alpha}}}$, respectively. This is referred to as "$q = 0$ helical motion" because the motion will not produce any moment proportional to C_{m_q}.

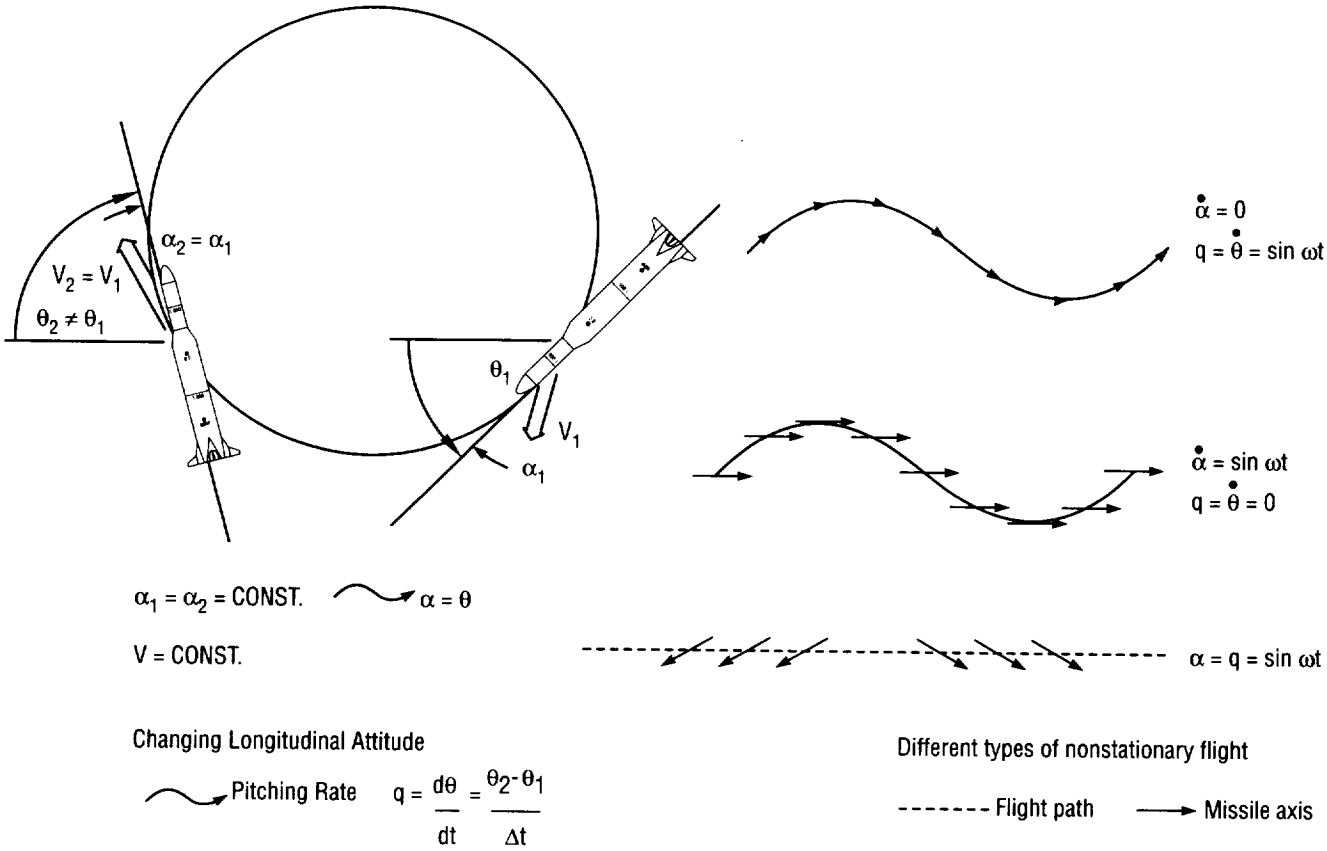

FIGURE 35. Rates of change of pitch rate versus rate of change of angle of attack.

For the second motion, the longitudinal axis of the vehicle remains tangent to the helical flight path at each point along the trajectory. A 2–D projection of this motion on the vertical plane is also depicted in

figure 35 in the $\dot{\alpha} = 0, q \neq 0$ case, where moment components proportional to C_{m_q} are produced. The α of the incident air-stream is zero, since both the longitudinal axis of the vehicle and the free-stream velocity vector are tangent to the flight path. This motion is referred to as "$\dot{\alpha} = 0$ helical motion" because the motion will not produce any moment proportional to $C_{m_{\dot{\alpha}}}$.[17]

The wind tunnel test conducted here involved the combined rate of change of α, that is $\dot{\alpha}$, and the rate of change of the longitudinal attitude, q, and these coefficients were measured as a sum. Similarly, in the lateral-directional case, a rolling velocity (p), or a yawing velocity (r) about a fixed axis at an α causes a simultaneous variation in the rate of change of the angle-of-sideslip ($\dot{\beta}$). If a system of body axes is used, the resulting composite expressions for the lateral-directional damping derivatives include a trigonometric function of α, such as

$$\left(C_{n_r} - C_{n_{\dot{\beta}}} \cos\alpha \right) \quad \text{and} \quad \left(C_{\ell_p} - C_{\ell_{\dot{\beta}}} \sin\alpha \right) .$$

For an axisymmetric vehicle,

$$C_{N_{\dot{\alpha}}} = C_{Y_{\dot{\beta}}} \quad \text{and} \quad C_{m_{\dot{\alpha}}} = C_{n_{\dot{\beta}}} \tag{26}$$

where

$$C_{N_{\dot{\alpha}}} \equiv \frac{\partial C_N}{\partial \dot{\alpha}} = \text{normal damping force coefficient}$$

$$C_{Y_{\dot{\beta}}} \equiv \frac{\partial C_Y}{\partial \dot{\beta}} = \text{side damping force coefficient}$$

$$C_{m_{\dot{\alpha}}} \equiv \frac{\partial C_m}{\partial \dot{\alpha}} = \text{pitch damping force coefficient, and}$$

$$C_{n_{\dot{\beta}}} \equiv \frac{\partial C_n}{\partial \dot{\beta}} = \text{yaw damping force coefficient.}$$

An LV can be considered dynamically stable if, after being disturbed from a nominal trajectory, the vehicle oscillates about the nominal condition with an amplitude of oscillation that decreases with time. A quantitative measure of dynamic stability or instability is the time it takes a disturbance motion to damp to half of its initial amplitude in a stable vehicle, or the time it takes for the initial amplitude to double in an unstable vehicle. Also of interest is the natural frequency and period of the oscillatory motion. The requirement for dynamic stability is typically expressed in terms of natural frequency and damping ratio of a natural mode. For a complete detailed development of the equations of motion for dynamic stability, see Etkin.[13]

The longitudinal motion of an LV disturbed from its nominal ascent trajectory is characterized by two oscillatory modes, the phugoid and the short period modes. The phugoid mode of a stable vehicle is lightly damped, has a long period, and is characterized by changes in pitch attitude at a nearly constant α. The short period mode is heavily damped in a stable vehicle, has a very short period, and is characterized by change in pitch rate at small forward velocity. For the experimental LV in the ascent trajectory, the short period mode is by far the more important mode. If this mode has a high frequency and is heavily damped, then the LV will respond rapidly to the FCA input without any undesirable overshoot. As the sum $\left(m_q + m_{\dot{\alpha}}\right)$ increases, the pitch damping increases. As the static stability increases, the vehicle natural frequency increases. As the cg is moved rearward, the longitudinal modes become aperiodic, and eventually unstable.

Figure 36 shows sample raw wind tunnel test data from the dynamic stability wind tunnel test program which was run with the forward cg configuration of the experimental LV to facilitate the free oscillation test method. Figures 37 and 38 show the qualitative dynamic stability results obtained from the data reduction and short period approximation mode equations. Figure 37 shows that for all FCA's tested, and at all Mach numbers tested, the pitch damping has significantly increased with the flight control augmentation.

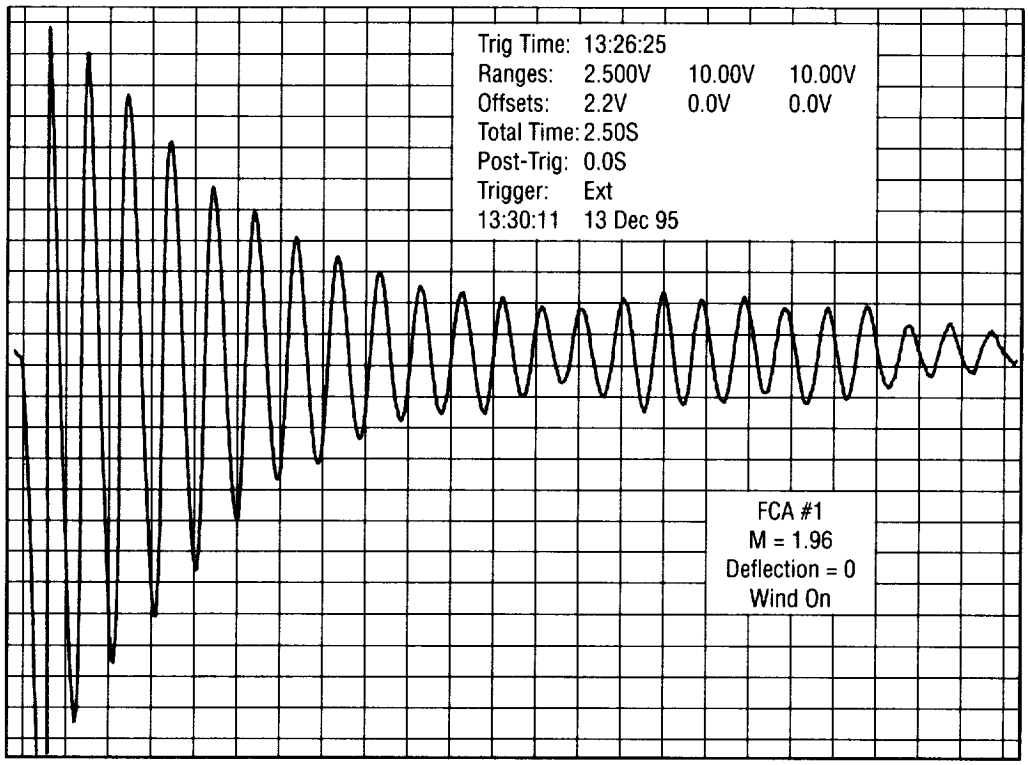

FIGURE 36. Sample dynamic stability wind tunnel test data.

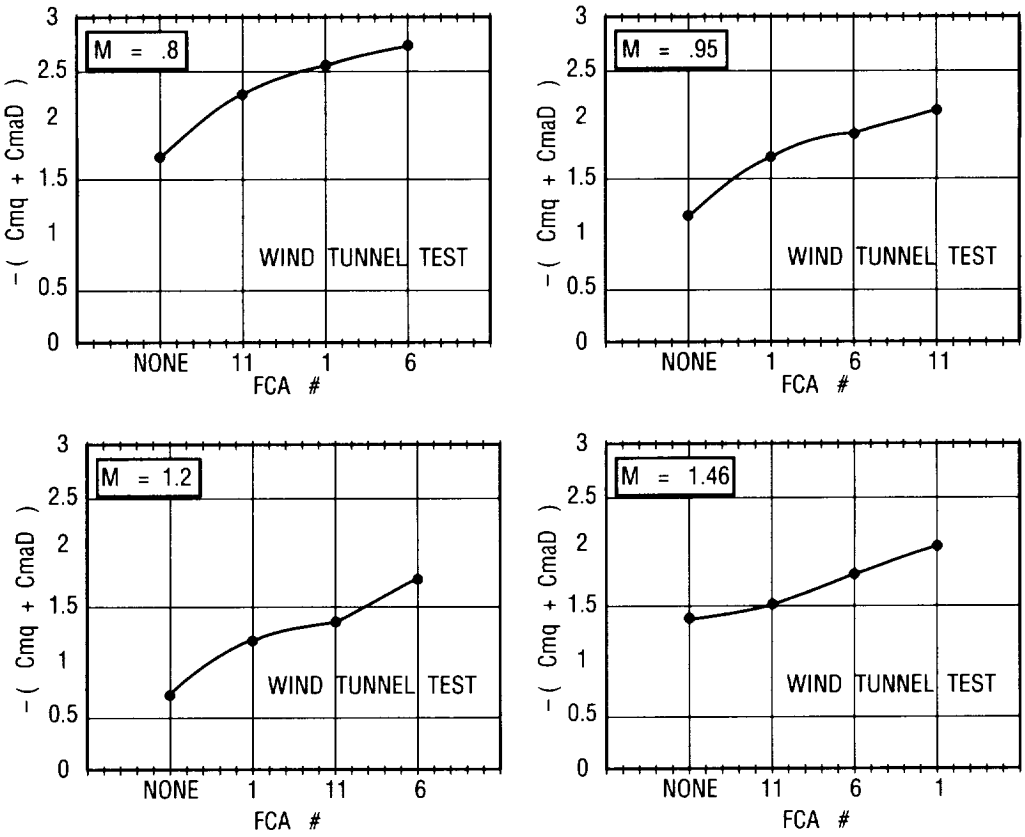

FIGURE 37. Pitch damping results.

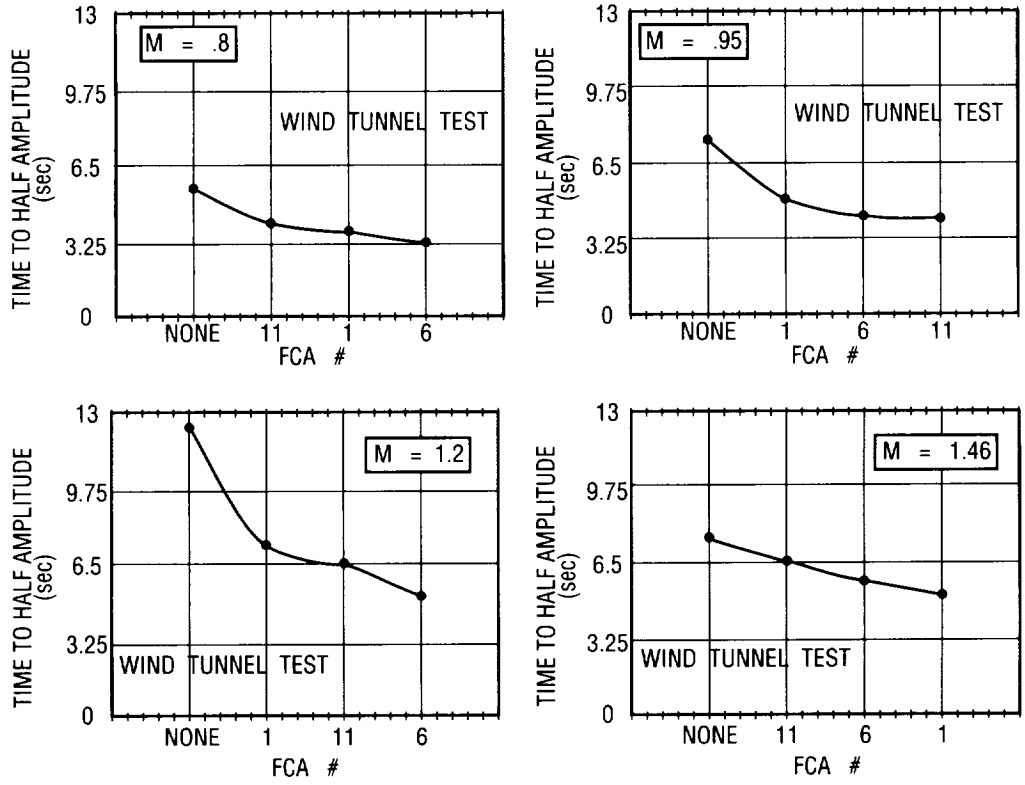

FIGURE 38. Short period mode characteristics.

The dynamic test Mach number interval was from M = 0.8 to M = 1.96. From the experimental LV mass properties and ascent trajectory data, pertinent quantities are listed below. Changes of consideration during this ascent time interval are indicated in percent at the bottom of the columns.

Mach No.	Time (sec)	Altitude (ft)	Q (psf)	Weight (lb)	cg Station (in)	I_y (slug-ft)
0.80	34	13,260	575.51	1,721,249	3860.15	132,714,436
0.95	39	17,700	691.46	1,677,553	3863.15	131,179,500
1.20	49	27,897	720.90	1,604,655	3867.65	128,768,416
1.31	53	32,165	722.57	1,577,027	3869.20	127,902,088
1.46	57	37,171	718.23	1,546,350	3870.76	126,980,902
1.96	68	51,714	630.19	1,466,188	3874.38	124,675,602
				14.8%	**0.37%**	**6.06%**

Pertinent dynamic stability parameters for the short period mode assessment included:

$$C_{Z_\alpha} = -\left(C_{L_\alpha} + C_{D_o}\right)$$

$$Z_\alpha = -\left(C_{N_\alpha} + C_{D_o}\right) \; Q \; S \; / \; \mu \; ; \qquad m_q = C_{m_q}\left(\frac{d}{u_o}\right) Q \; S \; d \; / \; I_y$$

$$m_\alpha = C_{m_\alpha} \; Q \; S \; d \; / \; I_y \; ; \qquad m_{\dot{\alpha}} = C_{m_{\dot{\alpha}}}\left(\frac{d}{u_o}\right) Q \; S \; d \; / \; I_y \qquad (27)$$

and the actual mass and moments of inertia were used at each point. From the basic equations of motion, developed in references such as 13 or 18, it can be derived that:

$$t_{half} \text{ or } t_{double} = \frac{2 \; \ell n \; 2}{\left(m_q + m_{\dot{\alpha}} + \frac{Z_\alpha}{u_o}\right)} \qquad (28)$$

Figure 38 shows that for all FCA's tested, and at all Mach numbers tested, the time-to-half-amplitude has significantly decreased. FCA No. 1 is a full diamond airfoil with a LE sweep (Λ) = 45° and a TE Λ = 0°; No. 6 is a half diamond airfoil with a blunt TE; No. 11 is a tapered trapezoidal planform with a LE Λ = 45° and TE Λ = –30°. FCA No. 6, the blunt TE design, provided the best overall pitch damping and short period mode characteristics, hence the best overall dynamic stability.

VI. ELASTIC VEHICLE

In reality an LV is not a rigid body, but an elastic body. The lowest elastic vehicle frequency must be well separated from that of the control system. Since the bending mode frequencies can couple with those of the control system when the bending frequencies are low, it is desirable to have the first bending mode frequency much higher than the control frequency. When bending mode frequencies and control frequencies are of the same order of magnitude, potential problems exist. The experimental LV of this research has a very far aft cg. It was desired to know how the elastic properties of this vehicle had changed vis-a-vis the original forward cg configuration, and if there would be any coupling of the elastic body frequencies with the frequencies of the control system. The significant modes of vibration are identified and the response spectra compared for the far aft cg experimental LV and the original configuration.

When an LV flies through the atmosphere during its ascent trajectory, aerodynamic forces act over its fuselage. All LV's, in varying degrees, are subject to the same static and dynamic instabilities that can be encountered by aircraft, plus some additional ones such as those attributed to the huge volumes of sloshing propellants. After liftoff and during ascent, the elastic LV is subjected to a myriad of randomly varying forces, including a time-dependent crosswind velocity. Some of these fluctuating loads are rather localized in extent and produce vibrations of only a small portion of the total structure. Other random loadings may be spread over the entire fuselage and produce vibrations of the complete LV (see fig. 39). There are also cases where rather localized forces can produce vibratory response of the complete vehicle. Vibrations resulting from random forces can produce dynamic aeroelastic instabilities which can and have resulted in catastrophic failure. In addition, internal acoustic fields generated by the random vibrations of structural panels can have adverse effects on the crew or result in damage to sensitive payloads. Some sources of significant random forces on an LV include atmospheric turbulence (wind gusts and wind shear), ground winds (including vortex shedding from the LV), engine noise, engine gimbaling, and sloshing propellants.

Panel flutter is a dynamic oscillatory aeroelastic instability that occurs at certain speeds at which the energy extracted from the airstream during a period of oscillation is exactly dissipated by the hysteretic damping of the surface. At speeds above flutter speed, divergence of the oscillation occurs. Methods of aeroelastic analysis differ according to the time dependence of the inertial and aerodynamic loads. Panel flutter can occur in an LV during supersonic flight and can be analyzed using a cylindrical shell model, such as Donnell's formulation.[19] The key to flutter prevention is to break up any coupling between the degrees-of-freedom (DOF).

If the magnitude and frequencies of the sloshing motions are not properly controlled relative to the frequencies of the vehicle, the complete system may become unstable. The longitudinal vibration can couple with the sloshing propellant and the propulsion system. Pogo (NASA SP–8055; 1970) was an early example of adverse coupling between the structure, propulsion system, and propellant. In pogo, the longitudinal structural vibrations, excited by combustion in the propulsion system, set up a pressure wave in the propellant. The propellant lines amplify this pressure wave and transfer it to the propulsion system. This results in a thrust oscillation which further drives the longitudinal vibration of the structure. As design goals, the ratio of slosh frequency to control frequency should be > 1, and the ratio of slosh frequency to fundamental bending frequency should be < 1. Desirable control frequency is 0.1 of the first bending

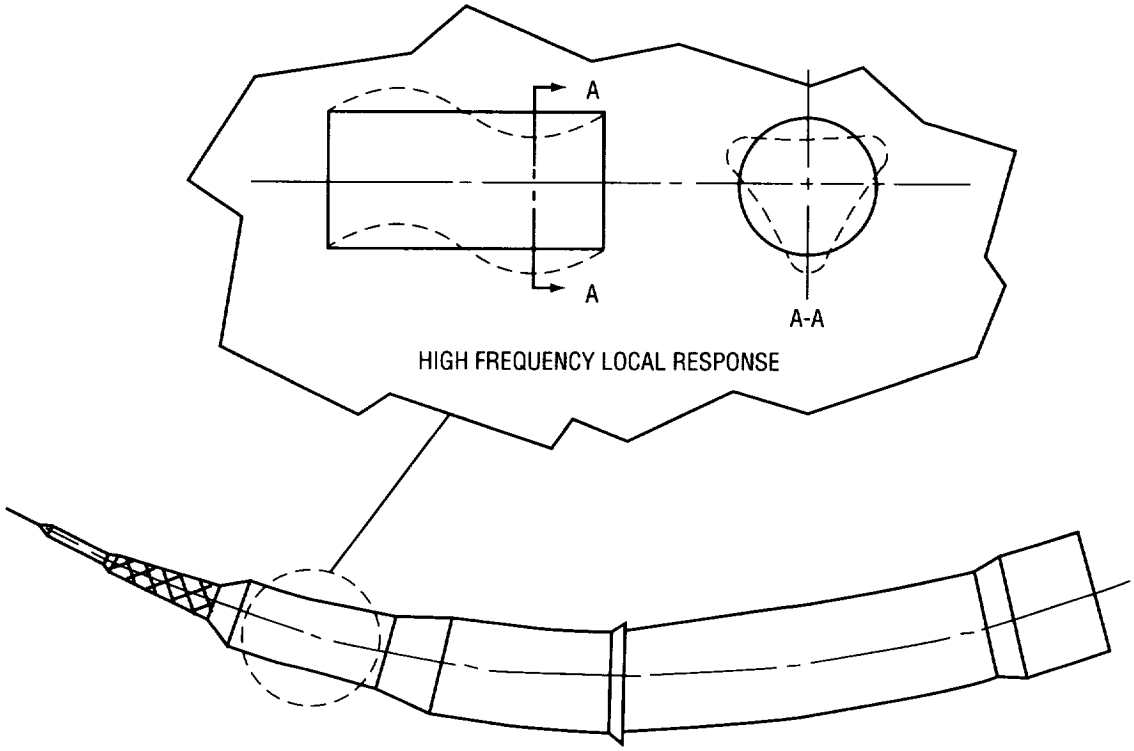

FIGURE 39. Types of LV elastic response.

mode, however, this is not always possible because of the low frequencies of this mode. Sloshing can be modeled as a series of harmonic oscillators, one for each slosh mode, and repeated for each tank. Figure 40 shows a typical modeling scheme. In the author's previous slosh studies (Shuttle–C LV), it was found that the LOX slosh could be significant when the slosh mass/total propellant mass > 0.1. This critical mass ratio was reached at approximately 80 sec after liftoff. This occurred in second stage flight, after the solid rocket booster separation; the damping factor was determined to be > 3 percent which was adequate for this LV.

Aeroelasticity, the interaction of aerodynamic forces on an elastic LV, is an important consideration, since a deformed fuselage can result in a change in magnitude and distribution of surface forces. The effect of aeroelasticity is to change the local α and control deflection through a redistribution of airloads. The α can be changed due to the elastic angular deflection of the fuselage.

$$\alpha_{\text{actual}} = \alpha_{\text{rigid-body}} + \alpha_{\text{elastic}} \tag{29}$$

Aeroelasticity can thus significantly affect the stability and control, hence the performance of an LV. For example, the pitching moment about the cg can increase more than 16 percent at maximum dynamic pressure (max Q) and the flexible body aerodynamic forces can increase the required engine gimbal angle by 30 percent, as was the case on the Saturn V LV.[1] Flexible body aerodynamics can cause a forward shift of the center of pressure, which was approximately 10 ft on the Saturn V.[1] Thus, flight control effectiveness is affected by structural deformation.

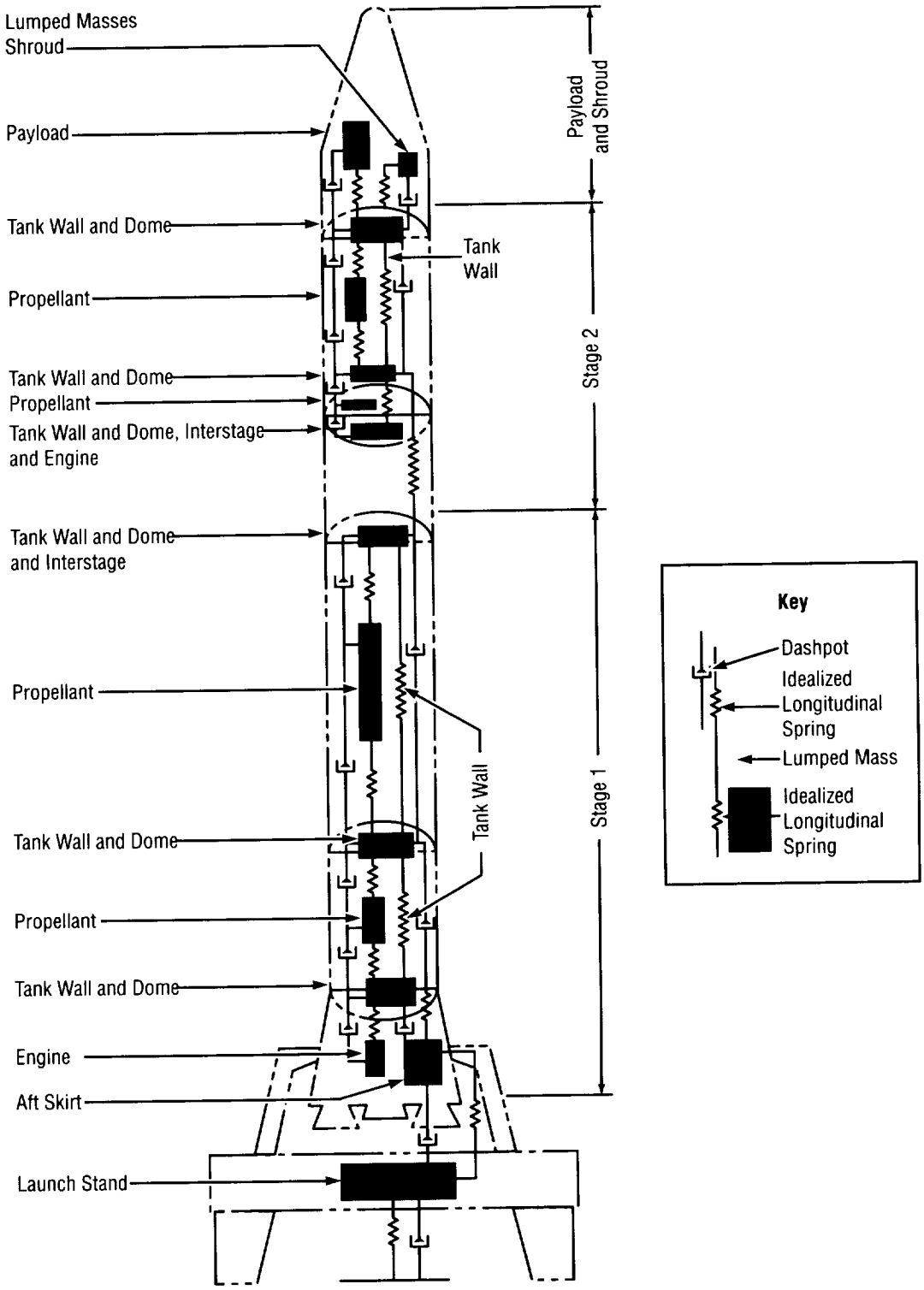

FIGURE 40. LV longitudinal dynamic model.

The forces and moments applied by the gimbaling of the rocket engines are governed both in magnitude and direction by the information derived from the sensors located along the fuselage. Flexible body analysis determines filter requirements and sensor locations. Active elements should be located on the LV where their authority over the modes to control is largest. Vehicle angular rates and displacements, the rigid body 6 DOF together with those of the elastic deflections, and the slosh are sensed by combinations of attitude gyros and accelerometers strategically located along the fuselage, ideally at the antinodes for gyros and at nodes for accelerometers, on the lowest vibration mode. If sensors are not properly placed, the aeroelastic effects can cause erroneous signals from the position and rate gyros on a deflected vehicle. Notch filters can be used to suppress sensor signals in selected small frequency ranges. Elastic DOF are best included in the control system design. Under adverse conditions, the autopilot can reinforce the amplitude of oscillation, leading ultimately to structural failure of the vehicle. The most natural way to actively damp an elastic mode is by local rate feedback. Uncertainty in modal parameters can require extended Kalman filters or adaptive control. A prerequisite for control system design is, therefore, an adequate representation of the elastic body motion under prescribed environmental and internal disturbance forces. This representation can be conveniently expressed in terms of the vibration frequencies and mode shapes of the vehicle. The vibrations consist of longitudinal, lateral, and torsional.

As the slenderness ratio of the vehicle increases, so do the aeroelastic effects, especially at max Q in the ascent trajectory, and the lowest bending frequency decreases. This can adversely affect the flight stability. Since the slenderness ratio of the experimental LV being considered here is three times that of the space shuttle, the aeroelastic effects are more significant. Elastic body frequencies are higher than those of the rigid body, and after liftoff the rigid-body mode frequencies are zero. When an LV is launched vertically from a launch pad, there is a large change in the structural boundary conditions which accompanies the liftoff.

Aeroserveoelasticity is the branch of aeroelasticity which deals with the flight control surfaces. Aeroelastic wind tunnel tests conducted at NASA Langley with and without the rigid Saturn I aerodynamic surfaces showed the same basic first bending mode shape. There was a small decrease in the first bending mode frequency and an increase in total damping with the aerodynamic surfaces, especially at subsonic speeds. The thick wedge surfaces cause these changes to a greater degree than did the thin surfaces.[20] The ratio of fin area to the total surface wetted area for the Saturn I LV was 8 percent. Fuselage bending and torsion have generally been shown to be more significant in altering the control forces on a LV than the local fin surface deformations.[1] In addition, for the LV of this research, it has been shown in equation (9) that the total FCA surface area is only 1.6 percent of the total LV wetted surface area, hence the FCA deformations have not been modeled in the elastic body analysis. The focus was on how the fuselage basic vibration modes changed in the aft cg configuration.

The NASA Structural Analysis (NASTRAN) Finite Element Method (FEM) normal modes analysis and frequency response have been used here to generate the modal data for the experimental LV, using a free-free, branched beam model, incorporating the NASTRAN subroutines CBAR, CBEND, MASS normalization, and no damping.[21] NASTRAN gives relative displacements so that individual actual displacements can be calculated as a function of initial conditions. For branched beam attachments, when two beam elements are connected to the same node, coupling with respect to both translation and rotation occurs. On the Saturn V, a 30-DOF beam-rod model was used to determine full-scale testing requirements. Normal modes, 1,388 DOF, and E = 10 E06 for Aluminum (Al) 2219 have been used here for the experimental LV at two trajectory critical points: liftoff and max Q conditions. Two configurations of the experimental LV

have been studied and compared—one with the original forward cg and one with the aft cg. The natural frequencies (ω_n's) of the LV, along with the vehicle mode shapes are functions of the structural properties and boundary conditions (BC). If the structural properties change, the ω_n's change, but the mode shapes may not. If the BC change, then the ω_n and the mode shapes both change. This can be seen below along with the most significant modes. Three sets of each mode have been produced in translation, and three sets of each mode have been produced in rotation. Zero natural frequency indicates one of the rigid body modes. Due to computer roundoff, the zero frequency ω_n's were on the order of 1.0 E–04 Hz. The normalization yields very small eigenvalues for a large heavy LV. Repeated root ω_n's occur for plane-of-symmetry vehicles and the eigenvalues are not unique since many orthogonal sets can be found. Modal superposition can be used to determine forced response using the modal results. In this investigation, attention has been focused on parameters important for stability and control analyses, for which the LV frequencies of interest are generally below 20 Hz and quite often below 10 Hz. The test LV has been represented by a series of lumped masses connected by elastic beams. Branched-beams have been included to represent the multiple load paths, and concentrated masses have been attached by translational and rotational springs. Eigenvalues and eigenvectors have been calculated, and mode shapes produced for the longitudinal (x-direction), lateral (y- and z-direction), and three rotational directions. Only the lateral deflections (z-direction) are shown here.

Table 11 lists the natural frequencies that are below 20 Hz for both the forward and aft cg configurations during the ascent trajectory critical points of liftoff and max Q. It can be seen that for the aft cg vehicle, the number of natural frequencies below 20 Hz has increased by 12 percent during liftoff, and has increased by 64 percent during max Q in the ascent trajectory. The lowest bending mode frequency has increased by 1.4 percent during liftoff, but has decreased by 2.8 percent during max Q for the aft cg configuration. Figure 41 lists the significant natural frequencies and shows the corresponding significant mode shapes for the forward cg configuration of the experimental LV at liftoff. Figure 42 lists the significant natural frequencies and shows the corresponding significant mode shapes for the forward cg configuration of the experimental LV at max Q. Figure 43 lists the significant natural frequencies and shows the corresponding significant mode shapes for the aft cg configuration of the experimental LV at liftoff. Figure 44 lists the significant natural frequencies and shows the corresponding significant mode shapes for the aft cg configuration of the experimental LV at max Q. Figure 45 shows the liftoff and max Q response spectra for the forward cg vehicle, and figure 46 shows the liftoff and max Q response spectra for the aft cg vehicle. The dynamic response is 150 percent greater in the aft cg experimental LV for both liftoff and max Q conditions.

TABLE 11. Experimental LV natural frequencies (Hz).

Forward cg		Aft cg	
Liftoff	***Max Q***	**Liftoff**	***Max Q***
2.5252	2.9227	2.5609	2.8420
2.6797	3.1381	2.6437	2.9202
4.9504	5.3889	5.0778	5.1306
5.1078	5.731	5.1852	6.4921
7.1450	8.7203	6.4479	7.7311
7.8363	9.3890	6.8917	8.3856
8.0998	9.4334	10.4543	11.5663
11.3736	14.4957	11.5939	11.6223
11.8005	15.2295	11.8976	12.6215
12.5657	15.9771	12.6223	13.2064
13.0057	18.7243	13.1882	13.7049
13.4119		13.6006	13.9265
15.0153		14.3102	15.1122
15.4947		15.1381	15.5340
15.6297		15.2189	16.0404
16.7443		16.1105	16.8734
19.8676		16.7120	17.4705
		19.4097	19.8484
		19.8079	

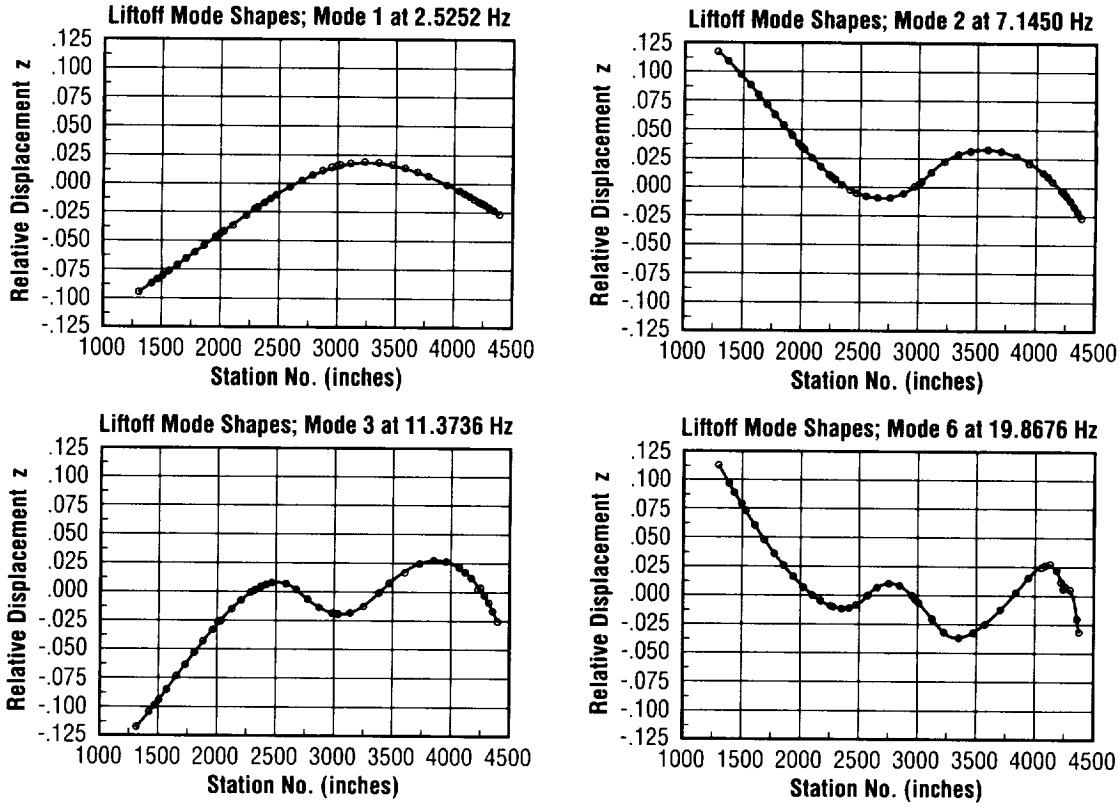

FIGURE 41. Forward cg mode shapes at liftoff.

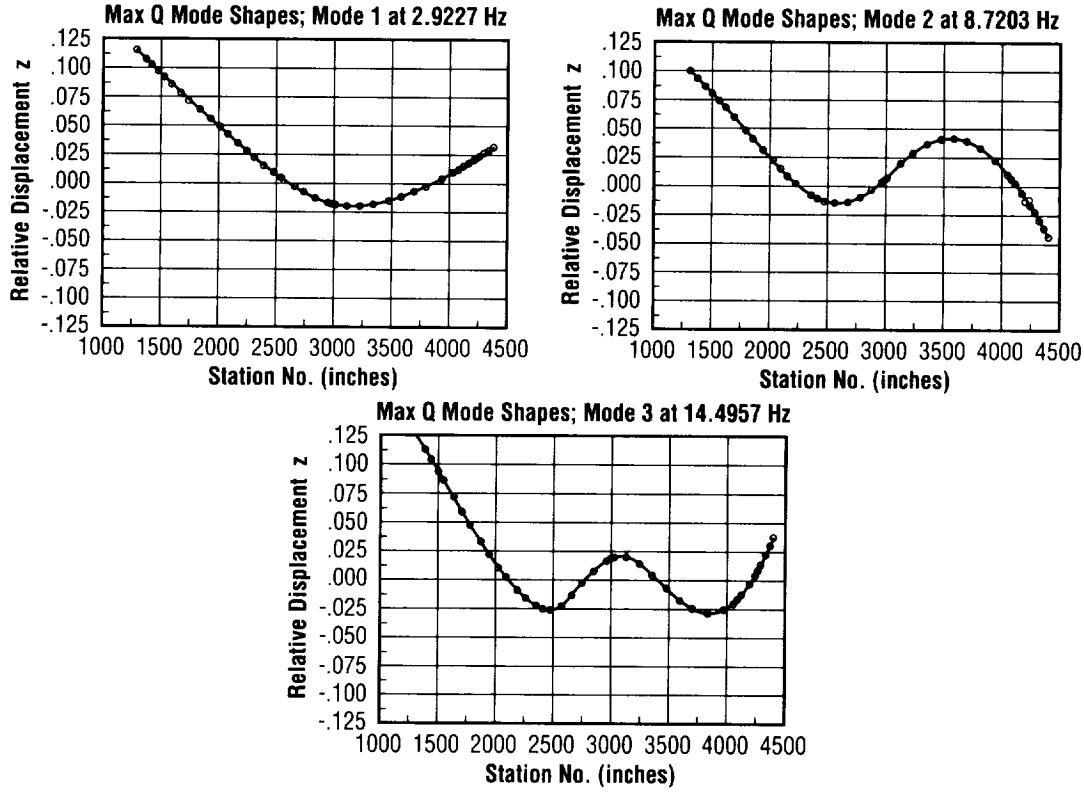

FIGURE 42. Forward cg mode shapes at max Q.

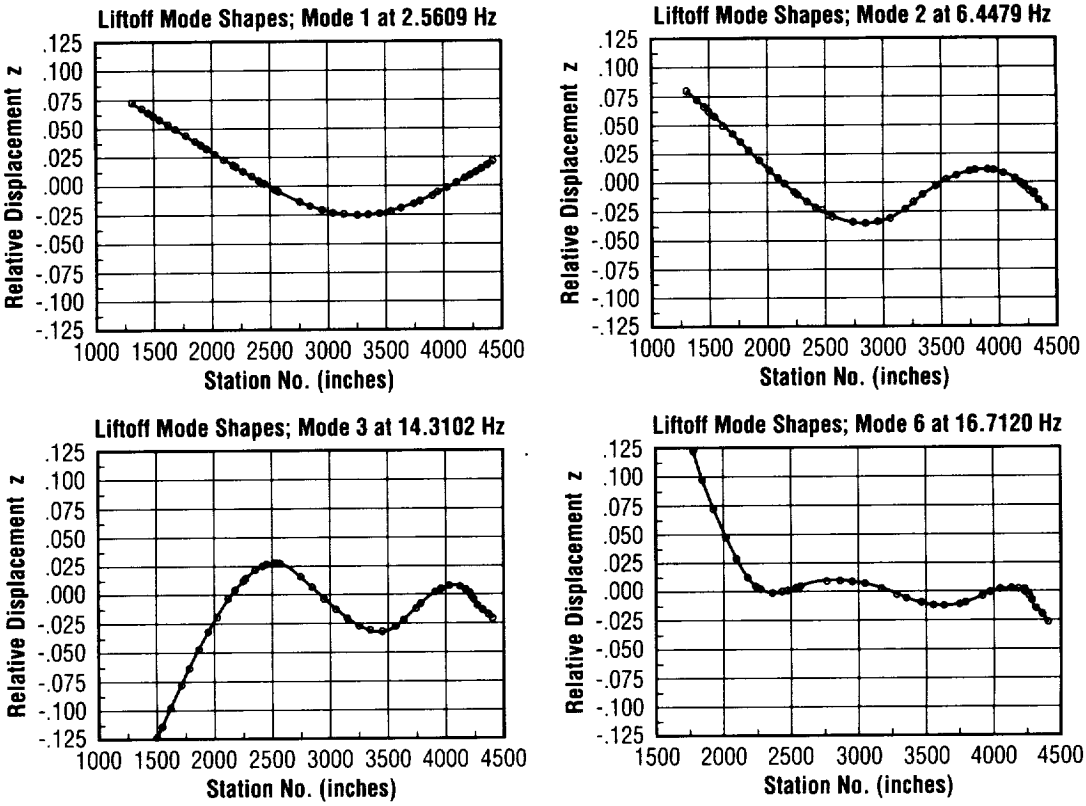

FIGURE 43. Aft cg mode shapes at liftoff.

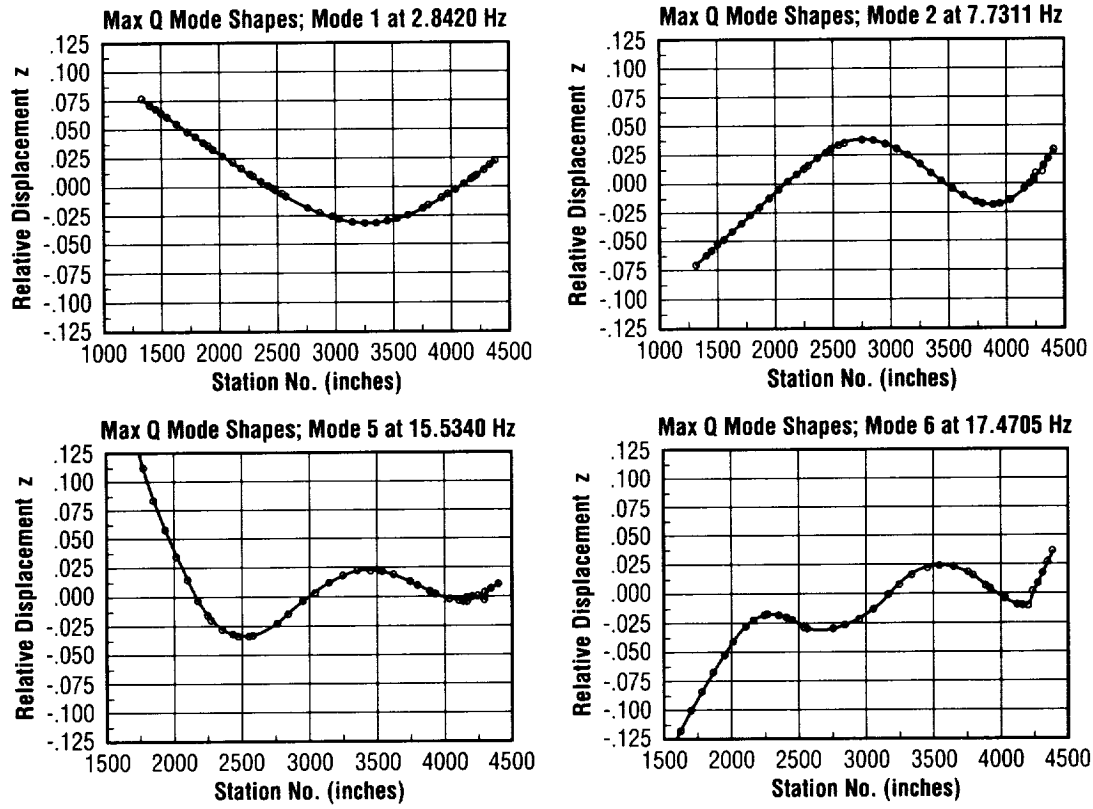

FIGURE 44. Aft cg mode shapes at max Q.

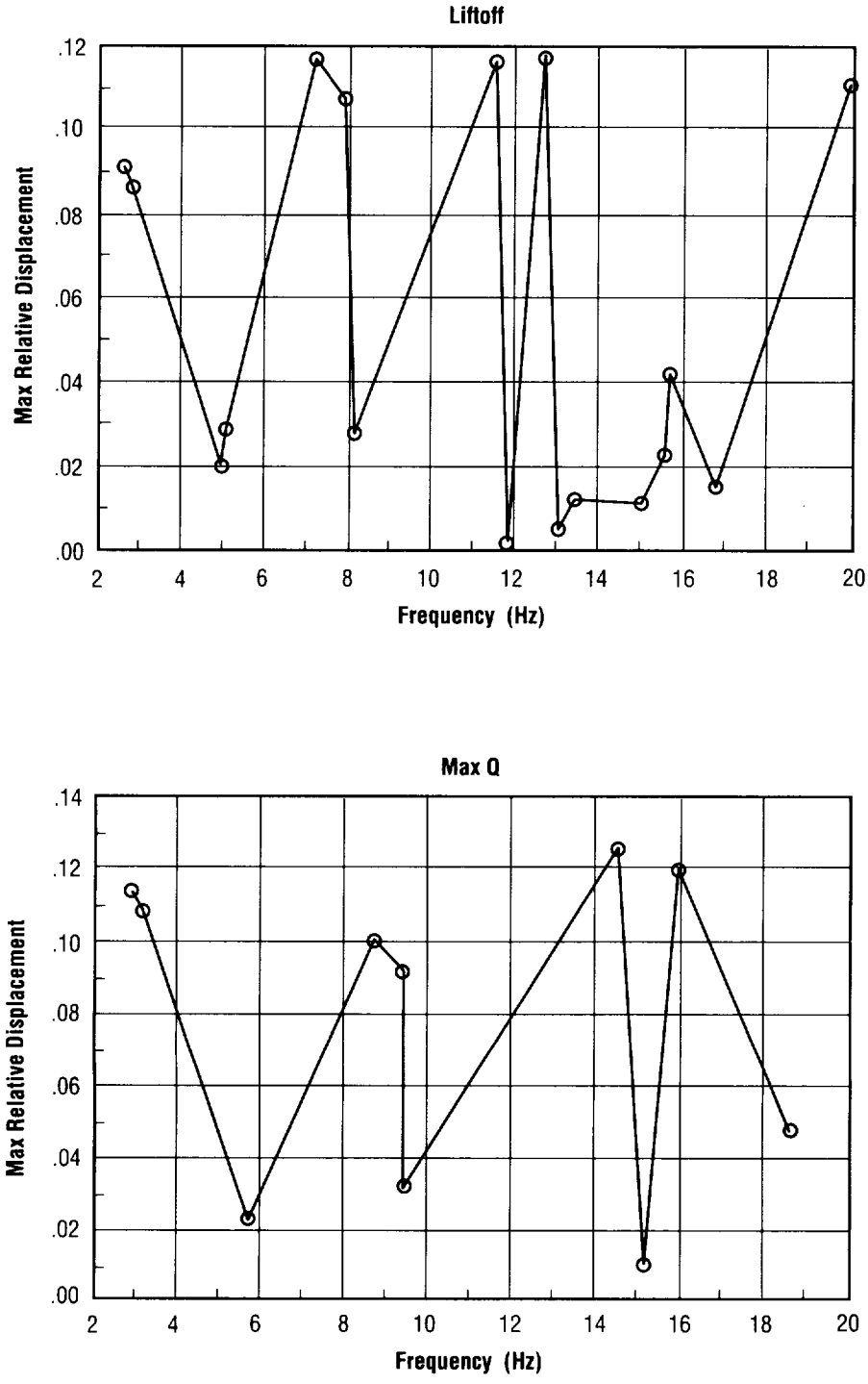

FIGURE 45. Response spectra for forward cg experimental LV.

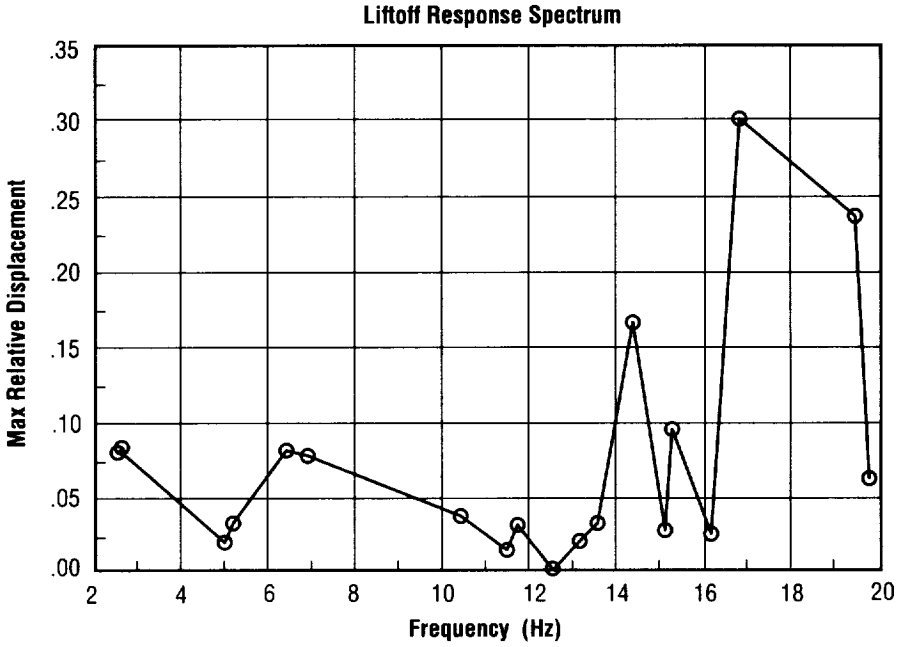

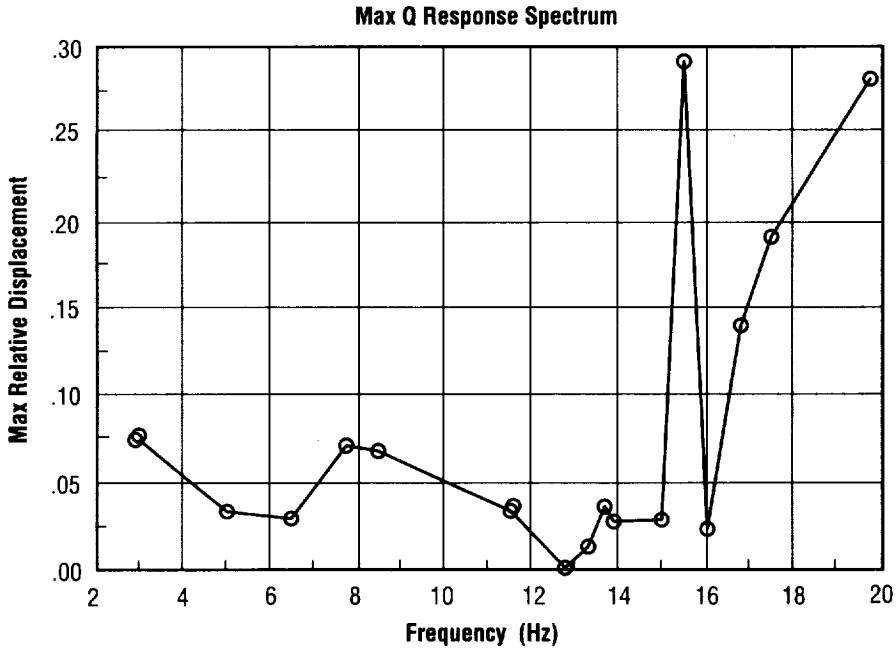

FIGURE 46. Response spectra for aft cg experimental LV.

VII. CONCLUSIONS

Flight control augmentors have been proposed, designed, and wind tunnel tested to provide the required control augmentation for a launch vehicle that could not be adequately controlled using engine gimbaling alone. Dramatic improvements in static stability were achieved with all aft FCA designs, at all Mach numbers tested. Improvements ranged from 41 to 72 percent with the blunt TE design giving the best results. The control analysis showed that the mere presence on the experimental LV of the aft FCA's with no deflection, increased the control ratio by 46 percent. When FCA deflection was utilized, the control ratio increased by 110 percent for 3° of deflection; to 346 percent for 6° of FCA deflection; and at 9.1° of FCA deflection, the aerodynamic moment was completely trimmed for the $\alpha = 4°$ case considered. The forward canard FCA's were able to trim the vehicle at 5° deflection.

The dynamic stability characteristics of the experimental LV, with and without three different selected FCA designs, have been qualitatively assessed from wind tunnel test data. It has been shown that for all FCA's tested, and at all Mach numbers tested, the pitch damping has significantly increased and the time-to-half-amplitude has significantly decreased with the flight control augmentation. The blunt TE FCA design provided the best overall pitch damping and short period mode characteristics, hence the best overall dynamic stability. NASTRAN normal modes analysis and frequency response have been used to generate the modal data for the elastic experimental LV, using 1,388 DOF at two trajectory critical points: liftoff and max Q conditions. Two configurations of the experimental LV have been studied and compared, one with the original forward cg, and one with the aft cg. The significant frequencies and modes of vibration have been identified, and the response spectra compared. The lateral bending modes were found to be of much greater significance than those of torsion. It has been shown that for the aft cg vehicle, the number of natural frequencies below 20 Hz has increased by 12 percent during liftoff and by 64 percent during max Q. Although the dynamic response was 150 percent greater in the aft cg configuration for both liftoff and max Q conditions, the lowest bending mode frequency had decreased by only 2.8 percent during max Q.

REFERENCES

1. Barret, C.: "Review of Our National Heritage of Launch Vehicles Using Aerodynamic Surfaces and Current Use of These by Other Nations (CDDF Project 93–05, Part II)." NASA TP–3615, April 1996.

2. Barret, C.: "Aerodynamic Flight Control Augmentation Devices for Saturn Class Launch Vehicles With Aft Centers-of-Gravity." *NASA Tech Briefs*, vol. 19, No. 5, p. 99, May 1995.

3. Barret, C.: "Launch Vehicle Flight Control Augmentation Using Smart Materials and Advanced Composites (CDDF Project 93–05, Part I)." NASA TP–3535, February 1995.

4. Barret, C.: "Launch Vehicle Shape Memory Alloy Actuators for Flight Control Augmentation Devices." *NASA Tech Briefs*, vol. 19, No. 8, p. 79, August 1995.

5. Barret, C.: "Flight Control Augmentation for Aft Center-of-Gravity Launch Vehicles." Contained in "*Technology for the Stars*," *NASA Marshall Space Flight Center Annual Report*, NASA TM–108501, 1995.

6. Barret, C.: "Flight Control Augmentation for Aft CG Launch Vehicles." 34th AIAA Aerospace Sciences Meeting, AIAA Paper #96–0905, January 16–18, 1996.

7. Barret, C.: "Design of Flight Control Augmentors and Resulting Flight Stability and Control Analyses." 35th Aerospace Sciences Meeting, AIAA Paper #97–0425, January 6–9, 1997.

8. Barret, C.: "Launch Vehicle Dynamic Stability Characteristics With Designed Flight Control Augmentors." 36th AIAA Aerospace Sciences Meeting, AIAA Paper #98–0300, January 12–15, 1998.

9. USAF, U.S. Air Force Stability and Control DATCOM, Flight Control Division, Air Force Flight Dynamics Laboratory, Wright-Patterson Air Force Base, OH, 1975.

10. Wood, R.M.; and Miller, D.S.: "Impact of Airfoil Profile on Supersonic Aerodynamics." *AIAA Journal of Aircraft*, vol. 23, No. 9, pp. 675–702, September 1986.

11. Ceresuela, R.: "Aerodynamic Problems of Sounding Rockets." AIAA Sounding Rocket Specialist Conference Proceedings, pp. 73–83, February 1967.

12. Springer, A.: "The MSFC's 14 × 14-Inch Trisonic Wind Tunnel." AIAA Paper 94–0539, January 1994.

13. Etkin, B.: *Dynamics of Flight—Stability and Control*, 3rd ed., John Wiley and Sons, 1996.

14. Cronvich, L.L.: AIAA Progress in Astronautics and Aeronautics, *Tactical Missile Aerodynamics*, p. 36, 1992.

15. Fuchs, H.: "Prediction of Dynamic Derivatives." AGARD, 1988.

16. Orlik-Ruckemann, K.J.: "Techniques for Dynamic Stability Testing in Wind Tunnels." AGARD-CP–235, Dynamic Stability Parameters Conference, May 1978.

17. Weinacht, P.: "Individual Components of Pitch-Damping." AIAA Paper 95–3458 CP, Atmospheric Flight Mechanics Conference Proceedings, pp. 291–301, August 1995.

18. Nelson, R.C.: *Flight Stability and Automatic Control.* 1st ed., McGraw-Hill, chapt. 2–5, 1989.

19. Bisplinghoff, R.L.; and Ashley, H.: *Principles of Aeroelasticity.* Dover Publications, 1975.

20. Hanson, P.W.; and Dogget, R.V.: "Aerodynamic Damping of Saturn I." NASA Langley Research Center, 1963.

21. Blakely, K.: *MSC/NASTRAN Basic Dynamic Analysis User's Guide.* The MacNeal-Schwendler Corp., 1993.

REPORT DOCUMENTATION PAGE

Form Approved
OMB No. 0704-0188

1. AGENCY USE ONLY *(Leave Blank)*	2. REPORT DATE	3. REPORT TYPE AND DATES COVERED
	August 1997	Technical Paper

4. TITLE AND SUBTITLE
Design of Launch Vehicle Flight Control Augmentors and Resulting Flight Stability and Control (Center Director's Discretionary Fund Project 93–05, Part III)

5. FUNDING NUMBERS

6. AUTHORS
C. Barret, Ph.D.

7. PERFORMING ORGANIZATION NAMES(S) AND ADDRESS(ES)
George C. Marshall Space Flight Center
Marshall Space Flight Center, Alabama 35812

8. PERFORMING ORGANIZATION REPORT NUMBER
M-839

9. SPONSORING/MONITORING AGENCY NAME(S) AND ADDRESS(ES)
National Aeronautics and Space Administration
Washington, DC 20546–0001

10. SPONSORING/MONITORING AGENCY REPORT NUMBER
NASA TP–3704

11. SUPPLEMENTARY NOTES
Prepared by Propulsion Laboratory, Science and Engineering Directorate

12a. DISTRIBUTION/AVAILABILITY STATEMENT
Subject Category 15
Unclassified–Unlimited

12b. DISTRIBUTION CODE

13. ABSTRACT *(Maximum 200 words)*

This report is Part III, the final part, of the Center Director's Discretionary Fund (CDDF) Project 93–05, in which the author as Principal Investigator has proposed and designed forward and aft, all-movable, blunt trailing-edge (TE), flight control augmentors (FCA's) to provide the required control augmentation for a family of aft center-of-gravity (cg) launch vehicles that could not be adequately controlled using engine gimbaling alone. This comprehensive flight mechanics research effort has been partially documented in previous publications. NASA TP–3535 (Barret, C.; February 1995) has presented the state-of-the-art assessment of smart materials and advanced composites directly applicable to the innovative design of the FCA's. NASA TP–3615 (Barret, C.; April 1996) has presented the developmental stages of the program, the comprehensive reviews of our national heritage of launch vehicles that have used aerodynamic surfaces, and the current use of these by other nations.

This publication presents the control requirements, the details of the designed FCA's, the static stability and dynamic stability wind tunnel test programs, the static stability and control analyses, the dynamic stability characteristics of the experimental LV with the designed FCA's, and a consideration of the elastic vehicle. Dramatic improvements in flight stability have been realized with all the FCA designs; these ranged from 41 percent to 72 percent achieved by the blunt TE design. The control analysis showed that control increased 110 percent with only 3 degrees of FCA deflection. The dynamic stability results showed improvements with all FCA designs tested at all Mach numbers tested. The blunt TE FCA's had the best overall dynamic stability results. Since the lowest elastic vehicle frequency must be well separated from that of the control system, the significant frequencies and modes of vibration have been identified, and the response spectra compared for the experimental LV in both the conventional and the aft cg configuration. Although the dynamic response was 150 percent greater in the aft cg configuration, the lowest bending mode frequency decreased by only 2.8 percent.

14. SUBJECT TERMS	15. NUMBER OF PAGES
flight control augmentors, all-movable controls, blunt trailing edge, flight mechanics, stability and control, Saturn-class launch vehicles, Saturn V, stability derivatives, control derivatives, static margin, wind tunnel test, short-period damping, control power, control effectiveness, elastic launch vehicle, mode shapes, dynamic response spectra, aft-cg launch vehicles	76
	16. PRICE CODE A05

17. SECURITY CLASSIFICATION OF REPORT	18. SECURITY CLASSIFICATION OF THIS PAGE	19. SECURITY CLASSIFICATION OF ABSTRACT	20. LIMITATION OF ABSTRACT
Unclassified	Unclassified	Unclassified	Unlimited